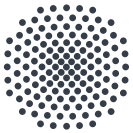

Universität Stuttgart

Nonlinear Optics in Hybrid Plasmon-Fiber Cavities

Von der Fakultät Mathematik und Physik
der Universität Stuttgart zur Erlangung der Würde
eines Doktors der Naturwissenschaften (Dr. rer. nat.)
genehmigte Abhandlung

vorgelegt von

Qi Ai

aus Heilongjiang, China

Hauptberichter:	Prof. Dr. Harald Giessen
Mitberichter:	Prof. Dr. Peter Michler
Prüfungsvorsitzender:	Prof. Dr. Hans Peter Büchler

Tag der mündlichen Prüfung: 21.05.2021

4. Physikalisches Institut der Universität Stuttgart

2021

Qi Ai: *Nonlinear Optics in Hybrid Plasmon-Fiber Cavities*, 2021

For my family
Für meine Familie
献给我的家人

Our job in physics is to see things simply, to understand a great many complicated phenomena in a unified way, in terms of a few simple principles.

— Steven Weinberg

ABSTRACT

The aim of this thesis is to study the nonlinear response of plasmon-fiber cavity systems achieved by depositing metallic nanoparticles onto the surfaces of tapered microfibers. In such systems, the localized plasmon resonances (LSPR) of the metallic nanoparticles can be excited via side-illumination and then coupled to the fiber cavities. In a classical picture, light with certain frequencies circulates and interacts with the metallic nanoparticles hundreds of times within the microcavities by continuous total internal reflection. This phenomenon is known as whispering gallery modes (WGMs). Thus, the light-matter interaction is dramatically boosted by efficient coupling between the plasmon modes of the metallic nanoparticles and the optical modes of the microfibers. It provides us with an opportunity to boost and investigate the nonlinear processes on the nanoscale in this hybrid system, especially the second-harmonic generation (SHG) and multiphoton photoluminescence (MPPL).

We firstly investigate the linear scattering response and SHG of the plasmon-fiber systems by coating gold nanoparticles onto the surface of microfibers. A specially developed dark-field reflection microspectroscopy setup combined with a switchable white light source and ultrafast laser source is utilized in the experiment. By sweeping the laser over the ultranarrow linear scattering spectral range, the frequency-dependence of the second-harmonic response is traced. It leads to an ultranarrow second harmonic resonance. Meanwhile, a coupled anharmonic oscillator model is used to describe the linear as well as second-harmonic resonances. It can be used to predict not only the shape of the SH resonance but also the SH efficiency. Based on this model, we come to the conclusion that the second harmonic intensity is directly proportional to the 4th power of the quality factor (Q) of the linear resonance. This result is clearly

proved by performing linear scattering and nonlinear emission measurements for 5 hybrid systems with slightly different quality factors.

Secondly, we find that there is always a broad MPPL background besides SHG in the nonlinear emission spectra of the coupled Au nanoparticles. We firstly determine and analyze the MPPL process of the fiber-coupled gold (Au) nanorods by performing excitation power dependent measurements. Furthermore, we observe the MPPL of coupled gold bipyramids (NBPs) particles differ from the emission spectra of coupled Au nanorods. Thus the polarization characteristics of the PL emission are investigated and also explained on the basis of the band and crystalline structure of gold. Based on the understanding of MPPL in gold NBPs, a quenching effect of four photon photoluminescence (4PPL) is discovered when coating the palladium (Pd) shell onto the gold NBPs due to the fast transfer of electrons from the gold to the palladium.

Finally, a high-Q doubly resonant plamson-fiber cavity is realized by fine-tuning the diameter of the microfibers in the hybrid systems further. In this system, the plasmon response of the gold bipyramid is matched to a high-Q cavity mode and simultaneously the second harmonic wavelength is also in resonance with a higher order cavity mode. Thanks to the simultaneous realization of the doubly resonant case and the high quality, the SHG is successful enhanced by $5-6$ orders of magnitude compared to the gold NBPs on the fused silica substrate. With an indirect calibration method, we estimated a second harmonic conversion efficiency up to 1.59×10^{-5}, which is believed to make the nonlinear plasmons stepping much closer towards practical applications. At the end, some applications and more design ideas of enhancing the nonlinear conversion efficiency based on the research in this thesis are proposed.

DEUTSCHE ZUSAMMENFASSUNG

Das Ziel dieser Arbeit ist es, die nichtlineare Antwort eines Faser-Resonator-Systems zu untersuchen, indem metallische Nanopartikel auf die Oberfläche von verjüngten optischen Mikrofasern aufgebracht werden. In einem solchen System können die lokalisierten plasmonischen Resonanzen (*engl. localized plasmon resonances: LSPR*) der metallischen Nanopartikel über eine seitliche Beleuchtung angeregt und dann an die optischen Mikrofasern angekoppelt werden. Im klassischen Bild kann man sich vorstellen, dass Licht bestimmter Frequenzen aufgrund der Totalreflexion mehrere hunderte Male in der Faser zirkuliert und bei jedem Durchlauf mit den metallischen Nanopartikeln interagiert. Dieses Phänomen ist unter dem Namen „*Whispering Gallery Mode*“ (WGM) bekannt. Daraus folgt, dass die Licht-Materie-Wechselwirkung durch die effiziente Kopplung zwischen den Plasmon-Moden der metallischen Nanopartikeln und den optischen Moden der Mikrofasern drastisch verstärkt wird. Dies ermöglicht uns die nichtlinearen Prozesse auf der Nanometerskala in diesem Hybrid-System, speziell die Frequenzverdopplung (*engl. second harmonic generation: SHG*) und die Multiphoton-Lumineszenz (*engl. multiphoton photoluminescence: MPPL*), zu verstärken und zu untersuchen.

Zunächst untersuchen wir die lineare Streuung und die Frequenzverdopplung des Plasmon-Faser-Systems, indem wir Nanopartikel aus Gold (Au) auf die Oberfläche der Mikrofasern aufbringen. Für dieses Experiment verwenden wir einen speziell entwickelten Aufbau bestehend aus einem Dunkelfeldmikroskop und einer variablen Lichtquelle, bei der zwischen Weißlicht und Licht aus einem Ultrakurzpulslaser gewählt werden kann. Durch Abtasten des ultraschmalrandigen Spektralbereichs der linearen Streuung mit dem Laser, wird die Frequenzabhängigkeit des frequenzverdoppelten Signals

untersucht. In diesem Fall ist dieses Signal eine untra-schmalbandige Resonanz zweiter Ordnung. Sowohl die linearen, als auch die Resonanzen zweiter Ordnung können mit Hilfe eines anharmonischen Oszillatormodells beschrieben werden. Dieses kann nicht nur die Form, sondern auch die Effizienz der Resonanz zweiter Ordnung vorhersagen. Auf Grundlage dieses Modells kommen wir zu dem Ergebnis, dass die Intensität des frequenzverdoppelten Signals proportional zur vierten Ordnung des Gütefaktors (Q) der linearen Resonanz ist. Dieses Ergebnis wird verifiziert, indem wir sowohl die lineare Streuung, als auch die nichtlineare Emission von fünf verschiedenen Systemen, die jeweils leicht unterschiedliche Gütefaktoren besitzen, vermessen.

Darüber hinaus stellen wir fest, dass die Spektren der gekoppelten Gold-Nanostäbchen neben dem frequenzverdoppelten Signal, stets einen breiten MPPL-Hintergrund aufweisen. Wir identifizieren und untersuchen den zugrundeliegenden MPPL-Prozess bei fasergekoppelten Gold-Nanostäbchen, indem wir Messungen mit variierender Anregungsleistung durchführen. Des Weiteren finden wir Unterschiede in den MPPL-Spektren von gekoppelten Gold Nano-Doppelpyramiden und gekoppelten Gold Nanostäbchen. Die Polarisationseigenschaften der Photolumineszenz-Emission werden untersucht und mithilfe der Bandstruktur von kristallinem Gold erklärt. Basierend auf dem grundlegenden Verständnis der MPPL in Gold Nano-Doppelpyramiden entdeckten wir einen Quenching-Effekt der Vier-Photonen-Lumineszenz, wenn die Nano-Doppelpyramiden mit einer Palladiumschicht ummantelt werden. Dieser hat seinen Ursprung in einem schnellen Elektronentransport von Gold zu Palladium.

Zum Abschluss realisieren wir einen doppelt-resonanten Plasmon-Faser-Resonator mit hohem Gütefaktor, indem wir den Durchmesser der optischen Mikrofaser weiter optimieren. In diesem System ist sowohl die Plasmonresonanz der Gold-Doppelpyramiden auf eine Resonatormode der Faser mit hohem Gütefaktor abgestimmt, als auch die Resonanz zweiter Ordnung auf eine Fasermode höherer Ordnung. Dank des gleichzeitigen Vorhandenseins der beiden Resonanzen und des hohen Gütefaktors, kann das SHG-Signal im Vergleich zu Gold

Nano-Doppelpyramiden auf einem Glassubstrat, erfolgreich um das 5 – 6-fache gesteigert werden. Mithilfe einer indirekten Kallibrationsmethode können wir eine SHG- Umwandlungseffizienz von bis zu 1.59×10^{-5} abschätzen, was einen wichtigen Schritt auf dem Weg zu praktischen Anwendungen von nichtlinearen Plasmonen darstellt. Zum Schluss werden einige mögliche praktische Anwendungsmöglichkeiten diskutiert und weitere Designideen, die auf Grundlage dieser Arbeit die nichtlineare Umwandlungseffizient weiter steigern könnten, werden vorgestellt.

CONTENTS

1

INTRODUCTION

Laser as one of the greatest inventions at 20*st* century opened a completely new field of research called *nonlinear optics*. The first laser was constructed by Theodore Maiman at 1960.[1] Shortly afterwards, two-photon absorption was observed at Bell Labs.[2] Almost simultaneous the SHG was discovered by Peter Franken et al. in the Randall Laboratory when the rubi laser beam illuminated to the quartz crystal. Enough strong electric field leads to the efficient interaction between photons and optical medium beyond simple linear interference, which means the response of the medium is no longer linearly related to the electric field of the laser beam. It was suddenly realized that some optical media, such as quartz crystal, could change the frequency of light. Afterwards, a lot of nonlinear optical media were investigated.[2–5] Until now, the nonlinear crystals have been one of the most important communications materials, which are widely used in the laser communication, optical radars, medical devices, material processes and so on. Meanwhile, it is observed that the phase-matched interacting beams play a key role in determining the efficiency of the nonlinear optical effects in those bulk nonlinear optical materials.

At the early stage of nonlinear optics, metal was not considered as a suitable choice to do nonlinear optics research due to their low optical nonlinearities. Especially, the second-order nonlinear effect is forbidden for most metals because of their inversion centrosymmetric structures.[6] However, sliver (Ag)-air interface was first reported

to produce a second-harmonic response (SH) in 1974.[7] The nonlinear polarization in metals is found to be induced by the surface plasmon-polariton at the metal surface where the symmetry is broken. Afterwards, nanofabrication techniques developed fast. Meanwhile, the ability of probing optical field has a great advantage. It makes the metallic nanostructures, which support the *localized surface plasmon resonance* (LSPR) that is the collective oscillations of free-electrons in metallic subwavelength structures showing a big potential to process nonlinear response since the metal-light interaction is boosted at the nano structures surfaces.[2, 8–10] The efficiency of the nonlinear optical effects is more determined by the confinement and strength of the electromagnetic fields in the nonlinear optical structures, not by the phase matching between the interacting lights and nonlinear materials. It opens a new door and even shifts the main research directions in nonlinear optics.

Regarding the linear response properties, the electro-magnetic resonances performed in metal nanostructures are experimental and theoretically proven to be sensitive to not only the dielectric characteristics of the material but also the details of the plasmonic nanostructure.[11–14] The physical mechanisms behind it have already been well established. In order to understand and study the nonlinear processes, especially the coherent processes, such as *second harmonic generation* (SHG) in those metallic nanostuctures, a series of research is done with a variety of metallic nano geometries, such as single nanoparticles,[15, 16] naon-apertures,[17] split-ring resonators,[18, 19] L-shape arrays,[20, 21] T-shaped nanodimers[22] and so on. Meanwhile, a great deal of effort is put into promoting the nonlinear conversion efficiency, such as matching the multiple resonances with the fundamental and generated second harmonic frequency,[23–27] combining nanostructures with high-nonlinear materials,[28–30] designing special non-centrosymmetric structures,[31, 32] utilizing the interaction between localized and delocalized plasmons[33, 34] and so on. However, as the nanofabrication technology develops and the research goes to deeper, the researched systems are more and more complex.

In order to design optimized configurations to boost the nonlinear conversion efficiencies and realize their applications in ultrafast nonlinear optical devices, it is necessary to reveal what determines the properties of generation of high-order harmonic in metallic nanostructures. Conceptually, some mechanisms including surface nonlinearities, bulk or volume nonlinearities and field enhancement are mainly responsible for the nonlinear optical response of metallic nanoparticles in a dielectric environment. However, as the researched systems are more and more multifarious and complex, the origin turns out to be more intricate. The linear properties, near-field distributions, spatial symmetries, different materials combination and other structure characteristics[35–37] are all factors to influence their nonlinear response. Especially, it was observed unexpectedly that the breaking centrosymmetry does not induce an increase in SH intensity in coupled plasmonic nanoparticles, compared to the symmetric systems.[24, 38] More and more open questions about the origin of the nonlinearity come and remain. The fundamental mechanism of determining the enhancement fact is still not clear. It is even a big challenge to completely describe the nonlinear process both from the experiment side or the theory side.[39–42]

As mentioned above, unraveling the mechanism responsible for the plasmonic nonlinear response is still an arduous task. The physicist Steven Weinberg said our job in physics is to see things simply, to understand a great many complicated phenomena in a unified way, in terms of a few simple principles. So we can think about our question from another side with a certain direction by getting rid of its complexity. Particularly, Although the factors which influence the nonlinear response vary in the different plasmonic systems, it is evident that a resonance at the fundamental frequency and its quality are crucial for all the harmonic generation.[43–45] The anharmonic oscillator model has been already utilized well to predict a nonlinear signal that is superlinearly proportional to the inverse of the resonance linewidth,[44, 46, 47] which is directly related to the quality factor. Thus, we get our main story-line in this thesis, namely how the quality factor influences the plasmonic nonlinear response and

followed with the question of what we can do with it to boost the nonlinear process further.

1.1 THESIS OUTLINE

This thesis is mainly researching a *hybrid fiber-plasmon cavity* which is designed to realize high second-harmonic efficiency on the sub-wavelength scale. In the process of tailoring, the influence on the nonlinear efficiency in plasmonic systems are firstly considered and analyzed. By optimizing the parameters in the hybrid cavities with specific designs, the nonlinear efficiency increases step by step. Micro-spectroscopy combining the microscopic and spectroscopic means is implemented to present the results of the optical properties in the coupled systems. Finally, ultra-high second harmonic generation enhancement is achieved in the plasmon-fiber hybrid system with *high quality factors (Q)* and under the *doubly-resonant condition*.

The main outline is as follows:

Chapter 2 gives a theoretical background starting from the light-matter interaction in metals. As one component of our hybrid system, metallic nanoparticles and their optical properties are introduced. In the following, the principles of nonlinear plasmonics is described, in particular, the second harmonic generation is discussed in an anharmonic model. Meanwhile, whispering gallery modes (WGMs) in microcavities are presented as the other element of our hybrid system. All these theoretical background provides us with a fundamental point of view about how the nonlinear process can be boosted by the enhanced localized electric field in the plasmonic nanostructures.

Chapter 3 introduce the preparation process of the fiber-gold nanoparticle hybrid systems including the fiber pulling, chemical synthesis of gold nanoparitcles and drop-coating process. Furthermore, we give a detailed description of a reflection dark-field microscopy setup combined with a spectrometer and switchable white light/laser source, which is utilized to implement and perform our microspectroscopic experiments.

Chapter 4 demonstrates the coupled structure between the microfiber and gold nanoparticles. In the linear optical regime, we see how the scattering is influenced by the illumination condition and the parameters of the coupled system, like the diameter of the microfiber, the size of the nano particles, etc. Next, the nonlinear microspectroscopic measurement is implemented. The results depict an ultra narrow second harmonic resonance. Meanwhile, the strong multiphoton induced photoluminescence is also detected and studied.

Chapter 5 present how the giant second harmonic generation enhancement is obtained starting from introducing the basic concept of the doubly resonant high-Q plasmon system. We first study the Q-dependent second harmonic generation by tailoring the quality factors in the hybrid system and then define the boosting effect in a high-Q system. The second step is followed to enhance the second harmonic response further by fine-tuning the diameter of the microfiber to make another hybrid mode generate at the second harmonic wavelength in respect to the central wavelength of the linear scattering. At the end, a method to calibrate the power of the spectrometer is introduced and implemented to quantify the power of the measured second harmonic response.

Chapter 6 gives a short conclusion of the main results displayed in this thesis and a brief outlook of how these results can be used in future developments of the nonlinear plasmonic systems.

2

THEORY BACKGROUND

Fundamental concepts and the theory backgrounds are always solid foundation for the experimental research. In this chapter, we focus on the concept of plasmonics, whispering gallery modes, and nonlinear optics. The interaction of metal nanoparitlces to the driving electric magnetic wave in the optical regime are introduced after the basic description of light-matter interaction. We will see how the surface electrons in such particles oscillate coherently with the excitation light. Based on the introduction of the nonlinear optics in the bulk materials, nonlinear optical properties of metal nanoparticles are studied with an extension of the Lorentz oscillator model. At last, the basic properties of the whispering gallery modes are presented and the parameters which influence those properties are discussed.

2.1 LIGHT-MATTER INTERACTION

The interaction of metal nanoparticles to the driving electric wave can be understood as the one of the particular cases. Starting with the fundamental Maxwell equations, the light-matter interaction can be understood in general. Then the Lorenz oscillator model provides us with a bridge between microscopic and macroscopic view, which means it is available in both cases. At last, a series of Drude-based models are developed to study the light-metal nanoparticles interaction, especially the nonlinear plasmonics. This section and

the Section 2.2 mostly follow the argumentations in the work of Stepan Maier,[10] Lukas Novotny and Bert Hecht,[48] and Craig F. Bohren.[49]

2.1.1 *Maxwells equations*

The Maxwell's equations of classical electrodynamics are the key basement to study the light-matter interaction. The differential form read as follows:

Gauss's law

$$\nabla \cdot \boldsymbol{D} = \rho_{\text{ext}}, \tag{2.1}$$

Gauss's law for magnetism

$$\nabla \cdot \boldsymbol{B} = 0. \tag{2.2}$$

Maxwell-Faraday equation

$$\nabla \times \boldsymbol{E} = -\frac{\partial \boldsymbol{B}}{\partial t}, \tag{2.3}$$

Ampère's circuital law

$$\nabla \times \boldsymbol{H} = \frac{\partial \boldsymbol{D}}{\partial t} + \boldsymbol{j}_{\text{ext}}, \tag{2.4}$$

Here, $\boldsymbol{E}$, $\boldsymbol{D}$, $\boldsymbol{H}$, $\boldsymbol{B}$ are the electric field, the dielectric displacement, the magnetic field, and the magnetic induction flux density, respectively. The source of these fields are the external current density $\boldsymbol{j}_{\text{ext}}$ and the external charge density ρ_{ext}.

In the macroscopic view, the relations between $\boldsymbol{D}$ and $\boldsymbol{E}$, as well as $\boldsymbol{H}$ and $\boldsymbol{B}$ are specified in constitutive relations, which start with the definition of the auxiliary fields themselves as follows,

$$\boldsymbol{D} = \epsilon_0 \boldsymbol{E} + \boldsymbol{P}, \tag{2.5}$$

$$\boldsymbol{H} = \frac{1}{\mu_0} \boldsymbol{B} - \boldsymbol{M} \tag{2.6}$$

where ϵ_0 is the electric permittivity of free space and μ_0 is the magnetic permeability of free space. They are linked to each other with the vacuum speed of light c by $c = \frac{1}{\sqrt{\epsilon_0 \mu_0}}$. Meanwhile, $\boldsymbol{P}$ is the polarization field and $\boldsymbol{M}$ is the magnetization field, which are defined in terms of microscopic bound charges and currents, respectively. Moreover, the macroscopic bound charge density ρ_{int} and bound current density $\boldsymbol{j}_{\text{int}}$ in terms of polarization $\boldsymbol{P}$ and magnetization $\boldsymbol{M}$ are then defined as

$$\rho_{\text{int}} = -\nabla \cdot \boldsymbol{P}, \tag{2.7}$$

$$\boldsymbol{j}_{\text{int}} = \nabla \times \boldsymbol{M} + \frac{\partial \boldsymbol{P}}{\partial t}, \tag{2.8}$$

When we insert constitutive equations 2.5 and 2.6 into Gauss's law Equation 2.1 and Ampère's circuital law Equation 2.4, the equivalent equations including only the electric field $\boldsymbol{E}$ and the magnetic flux density $\boldsymbol{B}$ are obtained:

$$\nabla \cdot \boldsymbol{E} = \frac{1}{\epsilon_0}(\rho_{\text{ext}} - \nabla \cdot \boldsymbol{P}) = \frac{1}{\epsilon_0}(\rho_{\text{ext}} + \rho_{\text{int}}) = \frac{1}{\epsilon_0}\rho_{\text{total}} \tag{2.9}$$

$$\begin{aligned} \nabla \times \boldsymbol{H} &= \mu_0(\boldsymbol{j}_{\text{ext}} + \frac{\partial \boldsymbol{P}}{\partial t} + \nabla \times \boldsymbol{M}) = \mu_0(\boldsymbol{j}_{\text{ext}} + \boldsymbol{j}_{\text{int}}) \\ &= \mu_0 \boldsymbol{j}_{\text{total}} \end{aligned} \tag{2.10}$$

Where we defined the total charge density $\rho_{\text{total}} = \rho_{\text{int}} + \rho_{\text{ext}}$ and the total current density $\boldsymbol{j}_{\text{total}} = \boldsymbol{j}_{\text{int}} + \boldsymbol{j}_{\text{ext}}$.

The magnetization $\boldsymbol{M}$ can be neglected when dielectric or metallic materials are considered. Assuming all external sources are far enough from the considered object, the external charge density ρ_{ext} and the external current density $\boldsymbol{j}_{\text{ext}}$ can be set equal to zero. In the following a wave equation for the electric field $\boldsymbol{E}$ in matter is derived by applying a rotation on 2.1 2.3 2.4 and together with two constitutive equations 2.5 and 2.6:

$$\Delta \boldsymbol{E}(\boldsymbol{r}, t) - \frac{n^2}{c^2}\frac{\partial^2 \boldsymbol{E}(\boldsymbol{r}, t)}{\partial t^2} = \mu_0 \frac{\partial^2 \boldsymbol{P}(\boldsymbol{r}, t)}{\partial t^2} \tag{2.11}$$

The left side correspondes to the wave equation in vacuum conditions for the electric field $\boldsymbol{E}$, while the right side describes the polarization $\boldsymbol{P}$ of the medium responding from the external light field $\boldsymbol{E}$.

In order to make the following steps more convenient, now we switch the wave equation in the spatial and the temporal domain 2.11 to a frequency domain description by Fourier-Transform as follows:

$$\Delta \boldsymbol{E}(\boldsymbol{r},\omega) + \frac{n^2\omega^2}{c^2}\boldsymbol{E}(\boldsymbol{r},\omega) = -\mu_0\omega^2\boldsymbol{P}(\boldsymbol{r},\omega) \tag{2.12}$$

In following, we only consider the linear optical response of the isotropic and nonmagnetic media in a low electric fields $\boldsymbol{E}$. The linear relationship between the induced optical polarization $\boldsymbol{P}$ and the electric field $\boldsymbol{E}$ is expressed as follows,

$$\boldsymbol{P} = \varepsilon_0\chi\boldsymbol{E} \tag{2.13}$$

Then we insert equation 2.13 into wave equation 2.12. The Helmholtz equation is obtained:

$$\Delta \boldsymbol{E}(\boldsymbol{r},\omega) + \underbrace{(1+\chi(\omega))}_{\varepsilon(\omega)}\frac{n^2\omega^2}{c^2}\boldsymbol{E}(\boldsymbol{r},\omega) = 0 \tag{2.14}$$

where we defined the dielectric function $\varepsilon(\omega) = 1 + \chi(\omega)$, where $\chi(\omega)$ is the dielectric susceptibility, with the frequency-dependence arising from material resonances. We can also get a conclusion that the temporally dispersive response of a medium induces a frequency dependence in permittivity.

So far, the linear electric field in the matter is described clearly by the Helmholtz equation. It has the same form as the wave equation in the free space, in particular in the case that the dielectric constant is directly related to the propagation velocity. The propagation velocity of the electric-magnetic wave is described as $v = \frac{c}{\tilde{n}(\omega)}$, with the complex refractive index $\tilde{n}(\omega)^2 = \varepsilon(\omega) = 1 + \chi(\omega)$. Hence, to determine the frequency-dependent complex refractive index or equivalently the complex dielectric constant is the key to study the linear optical properties of a medium.

Alternatively, the induced electrical current $\boldsymbol{j}(\omega)$ can be used to describe the optical response with electrical conductivity $\sigma(\omega)$ as $\boldsymbol{j}(\omega) = \sigma(\omega)\boldsymbol{E}(\omega)$. Then the relationship between the typical complex $\sigma(\omega)$ and $\varepsilon(\omega)$ can be straightly written as:

$$\varepsilon(\omega) = 1 + \frac{i}{\varepsilon_r \omega}\sigma(\omega) \tag{2.15}$$

When we consider the dielectric function, the conductivity and the refractive index as the complex function, more information directly related to damping effect in the medium can be derived in following:

$$n^2 - \kappa^2 = \varepsilon_r \tag{2.16}$$

$$2n\kappa = \varepsilon_i \tag{2.17}$$

Using $\tilde{n} = n + i\kappa$ and dispersion relation $\omega = \frac{c}{\tilde{n}}\tilde{\kappa}$, one obtains the complex wave vector as follows,

$$\tilde{\kappa} = \tilde{n}\frac{\omega}{c} = n\frac{\omega}{c} + i\kappa\frac{\omega}{c} = \kappa_r + \kappa_i \tag{2.18}$$

2.1.2 *The Lorenz oscillator model*

When we talk about the electron-magnetic (EM) wave propagation in the media, we generally divide the media into three main categories: insulating media, conducting media (metals) and semiconducting media. Their dielectric properties differ in terms of their band structures. The interaction of electron-magnetic wave with medias excites the electrons inside of materials, in where the intraband and interband transition are possible.

In the dielectric medium or the energy of the propagating wave is low enough, only valence electrons are affected and can be regarded as bound in a harmonic potential. In this case, the Lorentz oscillator (harmonic oscillator) can give a perfect description. It is the fundamental to investigate the origin frequency dependence of

the electric susceptibility in real materials. The bindings between electrons and nucleus are supposed to be similar to the that of a mass-spring system. Electrons react to an electromagnetic field by vibrating like damped harmonic oscillators. The way of the dipole responds to an external electric filed $\boldsymbol{E}(t) = \boldsymbol{E}(0)e^{-i\omega t}$ is given by the following equation of motion a bound electron:

$$m_e \frac{d^2\boldsymbol{x}}{dt^2} + m_e\gamma\frac{d\boldsymbol{x}}{dt} + m_e\omega_0^2\boldsymbol{x} = -e\boldsymbol{E}_0^{i\omega t} \tag{2.19}$$

Where

m_e	mass of an electron
$\boldsymbol{x}_t$	displacement of the electron
γ	damping factor
ω_0	resonance frequency of undamped oscillator
e	elementary charge
$\boldsymbol{E}_0$	the driving electric field

The damping parameter γ is a phenomenological parameter, which means it only can be determined from a particular experiment or quantum-mechanical considerations. In quantum mechanics it is iversely proportional to the lifetime τ and thus proportional to the decay rate of the excited electrons. Furthermore, the eigenfrequency ω_0 of the damped driven harmonic oscillator corresponds to the energy difference of both quantum states $\Delta\boldsymbol{E} = \hbar\omega_0$.

The solution to the previous equation submits the expression for the amplitude of oscillation x depending on the frequency:

$$\boldsymbol{x}(\omega) = \frac{e}{m_e}\frac{1}{\omega^2 - \omega_0^2 + i\gamma\omega}\boldsymbol{E}(\omega) \tag{2.20}$$

The displacement x leads to a dipole moment $\boldsymbol{p} = -e\boldsymbol{x}$ and then we can generally write for the dipole moment $\boldsymbol{p} = \varepsilon_0 \cdot \alpha \cdot \boldsymbol{E}$, where α is the atomic polarizability:

$$\begin{aligned} \alpha(\omega) &= -\frac{e \cdot \mathrm{x}}{\varepsilon_0 \cdot \boldsymbol{E}} \\ &= \frac{e^2}{m_e \cdot \varepsilon_0} \cdot \frac{1}{\omega_0^2 - \omega^2 - i\gamma\omega} \end{aligned} \tag{2.21}$$

When we consider that the dipole moments in a dielectric are independent and directed to the same direction, the polarization per unit volume can be attained by taking the sum of the single atom dipole moment over all atoms in a volume:

$$\boldsymbol{P} = N \cdot \boldsymbol{p} = N \cdot \varepsilon_0 \cdot \alpha \cdot \boldsymbol{E} \tag{2.22}$$

According to equation 2.13 $\boldsymbol{P} = \varepsilon_0 \cdot \chi \cdot \boldsymbol{E}$, we can have:

$$\chi(\omega) = N \cdot \alpha(\omega) \tag{2.23}$$

$$\varepsilon(\omega) = 1 + \chi(\omega) = 1 + N \cdot \alpha(\omega) \tag{2.24}$$

Then the susceptibility $\chi(\omega)$ is deduced from the previous equations:

$$\chi(\omega) = \frac{N \cdot e^2}{\varepsilon_0 \cdot m_e} \frac{1}{\omega_0^2 - \omega^2 - i\gamma\omega} \tag{2.25}$$

Here, we introduced the definition of the plasma frequency of the free electron gas ω_p (the deeper meaning will be explained at the end of this section):

$$\omega_p = \sqrt{\frac{n_e e^2}{\varepsilon_0 m_e}} \tag{2.26}$$

Consequentially, the dielectric function is given through this relation

$$\varepsilon(\omega) = 1 + \chi(\omega) = 1 + \frac{\omega_p^2}{\omega_0^2 - \omega^2 + -i\gamma\omega} \tag{2.27}$$

Splitting into real and imaginary part, it turns out to be:

$$\varepsilon_r(\omega) = 1 + \omega_p^2 \cdot \frac{\omega_0^2 - \omega^2}{(\omega_0^2 - \omega^2)^2 + (\gamma\omega)^2} \tag{2.28}$$

$$\varepsilon_i(\omega) = \omega_p^2 \cdot \frac{\omega\gamma}{(\omega_0^2 - \omega^2)^2 + (\gamma\omega)^2} \tag{2.29}$$

2.1.3 *Drude-based models*

Regarding to the conducting media, namely metals, the bands are partly occupied by the conduction electrons. Hence, the electrons can transfer from different quantum states in the band and move in the metals. As a result, we can basically consider them as ideal free electrons , which are not bounded to particular nucleus. In this case, the interband excitation is neglected and Drude model can be used to describe the propagation of EM wave in the media. However, the bound-electron region also always exists in metals, especially in the noble metals. The d-bands of the electronic structure in the noble metals are filled and close to the Fermi surface. As a result, a residual polarization is caused due to the positive back ground of the ion cores. In this case, modified models are developed to predict the optical response to the outside driving electron-magnetic field more precisely, such as quasi-free-electron model, Drude-Sommerfeld model and so on.

Drude model is also named free-electron model, in which electrons are completely free. Hence, we can also consider it as the Lorenz model without restoration force. Then the equation of motion of a free electron can be obtained from Lorentz model 2.19:

$$m_e \frac{d^2\boldsymbol{x}}{dt^2} + m_e\gamma\frac{d\boldsymbol{x}}{dt} = -e\boldsymbol{E}_0^{i\omega t} \tag{2.30}$$

Then the expression of the dielectric function derived from the emotion equation of the Drude model simplifies to:

$$\varepsilon(\omega) = 1 - \frac{\omega_p^2}{\omega^2 + i\gamma\omega} \tag{2.31}$$

The result can be separated into its real and imaginary parts as:

$$\varepsilon_r(\omega) = 1 - \frac{\omega_p^2}{\omega^2 + \gamma^2} \tag{2.32}$$

$$\varepsilon_i(\omega) = \frac{\omega_p^2 \gamma}{\omega^3 + \omega\gamma^2} \tag{2.33}$$

When we concern the optical frequency, namely $\omega_{visible} \gg \gamma$, the dielectric function can be simplified further:

$$\varepsilon(\omega) \simeq (1 - \frac{\omega_p^2}{\omega^2}) + i(\frac{\omega_p^2}{\omega^3/\gamma}) \tag{2.34}$$

If we only consider the ideal case of the undamped free-electron gas without decay and interband transitions, then the dielectric function can be further approximated to $\varepsilon(\omega) \sim 1 - \frac{\omega_p^2}{\omega^2}$. The effective damping in metals is generally generated from the scattering events, like electron-electron scattering, electron-phonon scattering, or scattering at lattice defects.

Here, it is worthy to point out the actual meaning of ω_p. When the electrons in a plasma are displaced from a homogeneous background of ions, they will be pulled back to the original positions in order to restore the neutrality of the plasma by the new built-up electric fields. As a result, the electrons will overshoot, and then oscillate around their balanced positions with a certain frequency. We call this characteristic frequency as plasma frequency. Equation 2.34 provides us with an important information that only in the frequency range below the plasma frequency, the metallic characters are maintained.

The dielectric function in a widely frequency range below the interband transitions can be described well in the undamped Drude model. However, there is no damping mechanism included. It is necessary to modify it in the visible and near infrared frequency range as if approaches d-band resonances. The first modification is made by correcting the electron rest mass to an effective mass m^* to account for the electron correlation effect in a heuristic manner.

In addition, an empirical, largely frequency independent term ε_∞ (usually $1 \leq \varepsilon_\infty \leq 10$ is inserted into the dielectric function. This correction is mainly considering the contribution of the positive ion cores to the dielectric function:

$$\begin{aligned} \varepsilon(\omega) &= \varepsilon_\infty - \frac{\omega_p^2}{\omega^2 + i\omega\gamma} \\ &= (\varepsilon_\infty - \frac{\omega_p^2}{\omega^2 + \gamma^2}) + i(\frac{\omega_p^2\gamma}{\omega^3 + \omega\gamma^2}) \end{aligned} \tag{2.35}$$

The plasma frequency is corrected to $\omega_p = \sqrt{\frac{ne^2}{\varepsilon_0 m^*}}$

This modified Drude model (also named Drude-Sommerfeld model) has been proved suitable to predict the dielectric function in a broader frequency range. For example, the results from it are in good agreement to the measured data for silver bellow 2.5 eV. However, regarding to the interband regions, there are more correction needed obviously. The extended Drude (Drude-Lorentz) model[50] consisting in addition of one Lorentz term has been developed. It succeeds to overcome the limitation of the Drude model for gold below d-bands energy range. Meanwhile, the interband transitions are also taken into account. Regarding the general form of the Lorentz terms of insulator, the dielectric function of gold is written as:

$$\varepsilon(\omega) = \varepsilon_\infty - \frac{\omega_p^2}{\omega^2 + i\omega\gamma} - \frac{\Delta\epsilon \cdot \Omega_L^2}{\omega^2 - \Omega_L^2 + \tau_L\omega} \tag{2.36}$$

where Ω_L stands for the oscillator strength, τ_L is the spectral width of the Lorentz oscillators and $\Delta\epsilon$ can be interpreted as a weighting factor. The results obtained by employing the Drude-Lorentz model are depicted in Figure 2.1 with compared to the results from the single Drude model. It is clearly seen that the real and imaginary parts of the dielectric function get excellent agreements within 500 nm $\sim$ 1 µm for the experimental data of gold.

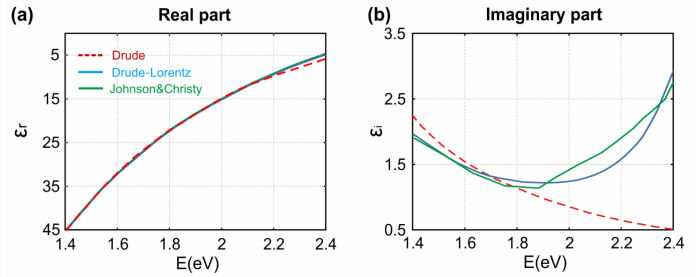

FIGURE 2.1. Real (a) and imaginary part (b) of the dielectric function of gold as measured by Johnson and Christy, calculated employing the single Drude model and the Drude-Lorentz model.

2.2 METALLIC NANOPARTICLES

So far, the optical properties of bulk materials are introduced by mainly calculating the dielectric function in the varying models, especially the Drude-based models of metals. Now it comes to our concerned question: how do metallic nanoparticles with dimensions below 100 nm respond to the driving EM waves in the optical frequency range?

2.2.1 *Near-field distribution*

When the electrons in the metallic nanoparticles are excited by the illuminating light, harmonic oscillations will arise from coupling to the oscillating EM field since the conduction electrons in metals are almost free, like the electrons and ions in a plasma. Meanwhile, an effective restoring force will be supplied to the driven electrons by the curved surface. As a result, a resonance is formed which leads to a field amplification inside and in the near-field area outside the particle. This resonance is called *localized surface plasmon resonance* (LSPR), which is different from the propagating surface plasmon polaritons at a metal/dielectric interface. The illustration of this oscillation in plasmonic particles is represented in Figure 2.2 in which showing

the displacement of the conduction electron cloud relative to the nuclei. Regarding the effect and its result of the curved surface, it can be simply suspected that its resonance frequency and position should depend on the size, the geometry, the material and also the surroundings.

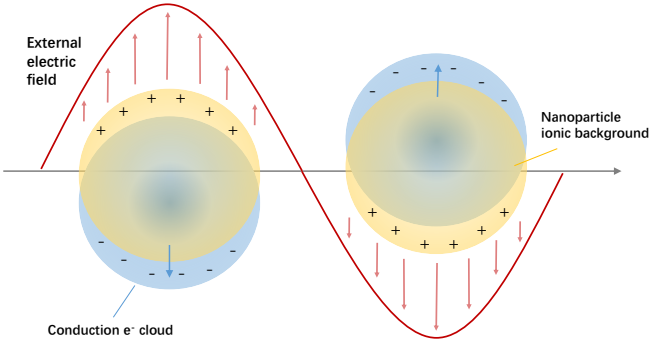

Figure 2.2. Sketch of a dipolar plasmon oscillation in a metallic nanosphere.

In the following section, we will discuss where these resonances arise from and how they depend on the parameters of these metallic nanoparticles. Furthermore, we will briefly show a sample with a series of gold nanorods, which is also utilized in this thesis.

We start with the simplest geometry for an analysis: a homogeneous sphere with radius a placed in a uniform, static electric field $E = E_0 z$. The surroudings is dielectric medium with dielectric constant $\varepsilon(\omega)$. (see Figure 2.3)

Because the nanosphere we are talking about has a size much smaller than the wavelength of the illuminating light, the phase of the EM wave over the whole nanosphere is nearly constant at any

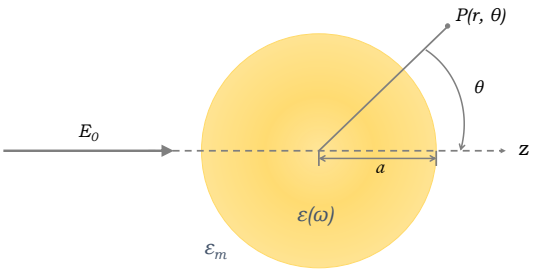

FIGURE 2.3. Sketch of a gold nanosphere with dielectric constant $\varepsilon(\omega)$ placed in an electrostatic field.

moment in time. Thus the retardation effects can be almost neglected. In other words, we can take the *quasi-static approximation* to analyze the optical response of nanoparticles with sizes below 100 nm.

In the above approximation, the applied field therefore can be regarded as the static $E = E_0 z$. Meanwhile, the magnetic flux density $\boldsymbol{B}$ does not change depending on the time and the Faraday's law 2.3 can be simplified to $\nabla \times \boldsymbol{E} = 0$. Hence, we can define the electric field $\boldsymbol{E} = -\nabla \Phi$. Now we need a solution of the *Laplace equation* $\Delta\Phi = 0$ for the electric potential Φ. Due to the azimuthal symmetry in this case, the solution for the potentials inside Φ_{in} and outside Φ_{out} the sphere can be given as:

$$\Phi_{in}(r,\theta) = \sum_{l=0}^{\infty} A_l r^l P_l(cos\theta) \tag{2.37}$$

$$\Phi_{out}(r,\theta) = \sum_{l=0}^{\infty} [B_l r^l + C_l r^{-(l+1)}] P_l(cos\theta) \tag{2.38}$$

where $P_l(cos\theta)$ are the Legendre Polynomials. The coefficients A_l, B_l and C_l can be determined from three boundary conditions in the next step. The first one is the boundary condition at infinity $r \to \infty$:

$$\Phi_{out} \to -E_0 z = -E_0 r cos\theta \tag{2.39}$$

Then they demand the continuity of the tangential components of the E-field and meanwhile the continuity of the normal components of the displacement field:

$$-\frac{1}{a}\frac{\partial \Phi_{in}}{\partial \theta}\bigg|_{r=a} = -\frac{1}{a}\frac{\partial \Phi_{out}}{\partial \theta}\bigg|_{r=a} \tag{2.40}$$

$$-\varepsilon_0 \varepsilon \frac{\partial \Phi_{in}}{\partial \theta}\bigg|_{r=a} = -\varepsilon_0 \varepsilon_m \frac{\partial \Phi_{out}}{\partial \theta}\bigg|_{r=a} \tag{2.41}$$

By implementing the boundary conditions, the electric potential inside and outside the metal sphere can be written as:

$$\Phi_{in}(r,\theta) = -\frac{3\varepsilon_m}{\varepsilon + 2\varepsilon_m} E_0 r cos\theta \tag{2.42}$$

$$\Phi_{out}(r,\theta) = -E_0 r cos\theta + \frac{\varepsilon - \varepsilon_m}{\varepsilon + 2\varepsilon_m} E_0 a^3 \frac{cos\theta}{r^2} \tag{2.43}$$

Interestingly, the potential outside is a superposition of two contributions including the externally applied electric field and that one of a dipole at the center of the particle. The latter term is originally induced from the surface charge density on the interface of the particle. Thus, we can rewrite the potential outside by bringing in the dipole moment $\boldsymbol{P}$ as:

$$\Phi_{out}(r,\theta) = -E_0 r cos\theta + \frac{\boldsymbol{P}\cdot\boldsymbol{r}}{4\pi\varepsilon_0\varepsilon_m r^3} \tag{2.44}$$

with

$$\boldsymbol{P} = 4\pi\varepsilon_0\varepsilon_m a^3 \frac{\varepsilon - \varepsilon_m}{\varepsilon + 2\varepsilon_m} E_0 \tag{2.45}$$

Furthermore, the polarizability α can be introduced via $\boldsymbol{P} = \varepsilon_0\varepsilon_m\alpha\boldsymbol{E_0}$:

$$\alpha(\omega) = 4\pi a^3 \frac{\varepsilon - \varepsilon_m}{\varepsilon + 2\varepsilon_m} \tag{2.46}$$

Equation 2.46 is the key result of this part. On the one hand, it is clearly seen that the polarizability α is proportional to a^3 and hence to the volume of the particle. On the other hand, the phase and absolute value of the polarizability α varies as the dielectric function ε_ω of the Drude form. It is obvious that the polarizability exhibit a resonance under the condition of the minimum $\mid \varepsilon + 2\varepsilon_m \mid$ for the case $Re[\varepsilon_\omega] = 2\varepsilon_m$ (Fröhlich condition). In particular, when we consider the dielectric function in the Drude model, the resonance frequency ω_0 of a sphere located in air can be calculated to $\omega_0 = \omega_p/\sqrt{3}$. Finally, we can also see the strong dependence of the resonance frequency on the dielectric function from the Fröhlich condition.

Now we can return back to the question proposed at the beginning of this section: how to evaluate the distribution of the electric field from the above results about the potentials.

$$\boldsymbol{E}_{in} = \frac{3\varepsilon_m}{\varepsilon + 2\varepsilon_m}\boldsymbol{E}_0 \tag{2.47}$$

$$\boldsymbol{E}_{out} = \boldsymbol{E}_0 + \frac{3\boldsymbol{e_r}(\boldsymbol{e_r}\cdot\boldsymbol{P}) - \boldsymbol{P}}{4\pi\varepsilon_0\varepsilon_m}\frac{1}{r^3} \tag{2.48}$$

As expected, the resonance in α leads to a resonant enhancement of both the inside and outside fields. This is also the key motivation to drive a great deal of scientific interest in plasmonics. The enhanced interaction between the metallic nanoparticles and the high sensitivity of the resonance position dependent on the surroundings makes them show a big potential for optical devices and sensors.

2.2.2 *Far-field response*

Up to now, we have already discussed the near-field optical properties of the metallic nanoparticles. A metallic particle reacts with the surrounding medium and also the adjacent other nanoparticles through the near-field response. This near-field response can be probed via certain means, like the scanning of near-field optical microscopy (SNOM), electron energy-loss spectroscopy (EELS) and so on. On the

other hand, metallic nanoparticles also have strong far-field responses dominated by absorption and scattering light (named extinction in combination). In the quasi-static regime, a metal sphere with small size (much smaller than wavelength of light) can be regarded as an ideal dipole in an applied field. The radiation of this dipole conducts the scattering of plane-wave illumination by the sphere.

The problem about the scattering and absorption of a spherical metallic nanoparticle was first solved by Gustav Mie.[51]. This solution allows us to predict the linear response The absorption and scattering cross-sections can be written as[49]:

$$\sigma_{abs} = k \cdot Im[\alpha(\omega)] \tag{2.49}$$

$$\sigma_{sca} = \frac{k^4}{6\pi} \mid \alpha(\omega) \mid^2 \tag{2.50}$$

Here, k is the wave-vector in the surrounding dielectric medium and α is the polarizability determined by equation 2.46. Then we can get the conclusion that the efficiency of absorption scales with a^3, while the efficiency of scattering is proportional to a^6.

Now, we continue with another example: the rod-like nanoparticles with a size still much smaller than the wavelength of the light. The scattering problem of a small ellipsoidal particle was first solved by Gans.[52] Based on it, the linear polarizability along one certain axes $n(1, 2, 3)$ is written as:[49, 53]

$$\alpha_n(\omega) = V \frac{\varepsilon - \varepsilon_m}{g_n(\varepsilon - \varepsilon_m) + \varepsilon_m} \tag{2.51}$$

Here, V is the volume of the rod-like nanoparticle and g_n is geometric factors along the axes of the ellipsoid. Regarding to the case of rod-like shape, in which the two axes are equal and another one is long ($a > b = c$), the geometrical factors can be written as:

$$g_1 = (1/d^2 - 1)\left[(1/2d)\ln\left(\frac{1+d}{1-d}\right) - 1\right] \tag{2.52}$$

$$g_2 = g_3 = (1 - g_1)/2 \tag{2.53}$$

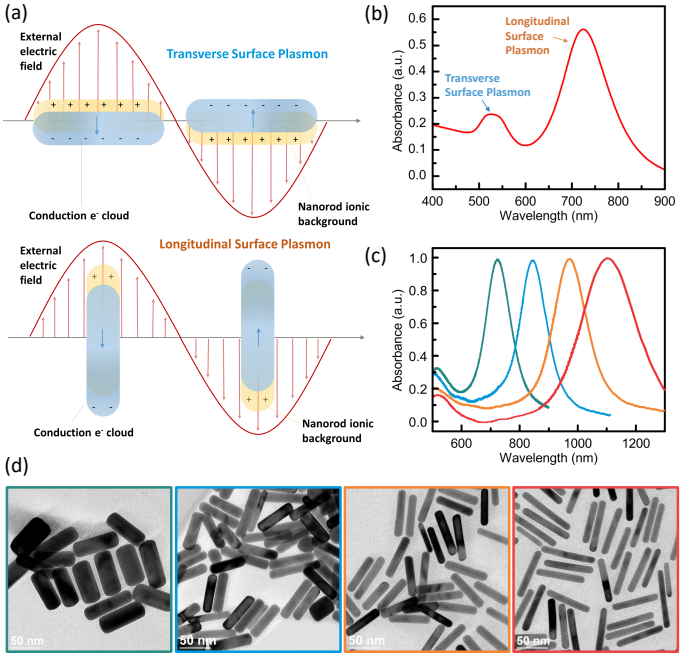

Figure 2.4. (a) Schematic of longitudinal and transverse surface plasmon oscillations for a nanorod. (b) A typical measured absorbance spectrum of a gold nanorod solution.(c) Measured absorbance spectra of gold nanorods with different aspect ratio, whose corresponding transmission electron microscope images are presented in (d).

where $d = \sqrt{1 - b^2/a^2}$ stands for the eccentricity ratio of the particle, which is related to the aspect ratio a/b.

By combining equations 2.51, 2.49, and 2.50, the scattering and absorption cross-sections for the nanorods can be calculated. It clearly shows there will be two resonances in the spectrum involving the electron oscillations along the long axis called the longitudinal surface plamson (LSP) and the one along the short axis called the transverse surface plasmon(TSP), see Figure 2.4(a) and (b). Meanwhile, the

aspect ratio has a significant effect on the LSP resonance but only slightly influence the TSP resonance. The measurement results in Figure 2.4(c) and 2.4(d) provide clear presentation. Furthermore, a bigger aspect ratio leads to a larger corss-section as the volume of the particle increases.

A few things need be noticed here. Firstly, for small particles with sizes much smaller than the wavelength, one can neglect its scattering and the measured extinction cross-section is governed by the absorption cross-section. Relatively, the scattering cross-section σ_{sca} will fast become larger than σ_{abs} as the particle size increase. Thus the optical response from a single particle is dominated by scattering. Secondly, not only the particles' size but also the surrounding dielectric medium contribute the tuning of the surface plasmon resonance. All those parameters are considered in our designed hybrid system.

2.3 NONLINEAR OPTICS

The research interest on nonlinear optics can be traced back to the advent of the laser. Nonlinear optical processes only can occur when a large enough amount of photons is confined in a small volume. The ultrafast laser sources with duration from picoseconds to femtoseconds made it possible in practice. The temporal interaction between the laser pulse and the target medium decrease the risk of optically induced damage. Furthermore, the energy carried by the short pulse gives rise to high light intensities. Thus, the ultrafast laser sources are the ideal means to provoke a variety of nonlinear optical phenomena.

Nonlinear optical effects are inherently weak since they are governed by photon-photon interactions enabled by materials. Meanwhile, the phase matching is a critical precondition for a variety of nonlinear optical processes, for example, the high-order generations, coherent anti-Stokes Raman scattering, and so on. However, the optical near field interacting with matter in metallic nanostrucutres is just subwavelength scales, where the phase matching is no longer the sufficient condition for the nonlinear processes. Thus metallic

nanostructures become proper candidates to boost the nonlinear processes. In this emerging paradigm of nonlinear optical field, the key parameter to determine the efficiency of the optical processes is not the quality of the phase matching between the interacting optical beams anymore, but the degree of confinement of the optical near-field and nonlinear optical structures in a nanometer size volume.

In this section, the basic main theoretical concepts pertaining to nonlinear optics in metallic nanostrucutres will be introduced. We start with the explanation of wave interactions and propagation in bulk nonlinear optical media, which is mostly based on the argumentation in the work of Robert W.Boyd [6], and then continue with a more detailed discussion of the origins and theory of the nonlinear plasmonics which are nonlinear light-matter interaction in the sub-wavelength regime. In particular, we will focus on the second harmonic generation and multiphoton photoluminensce of metallic nanostructures, which is also the main research content in this thesis. Moreover, the extension of the Lorentz oscillator model to the nonlinear regime is given, which is important for the research of resonant optical nonlinearities. This model is used to predict the second harmonic response from our fiber-plasmon hybrid system and meanwhile inspires us to reveal the relation between the quality factor of the system and the SHG intensity experimentally, which will be introduced in later Chapter 5.

2.3.1 *Light-matter interaction in nonlinear media*

For a theoretical concepts of nonlinear optics, it is necessary to review back to the polarization of a medium in the time domain $\boldsymbol{P}(t)$, which was already introduced for the case of a linear optical response in Equation 2.13. In order to determine the nonlinear optical response

of a medium, the polarization can be expressed as a power series expansion in terms of the E-field.

$$\begin{aligned}\boldsymbol{p}(\boldsymbol{r},t) =&\varepsilon_0\chi^{(1)}(\boldsymbol{r},t)\boldsymbol{E}(\boldsymbol{r},t) + \varepsilon_0\chi^{(2)}(\boldsymbol{r},t)\boldsymbol{E}(\boldsymbol{r},t)^2 \\ &+ \varepsilon_0\chi^{(3)}(\boldsymbol{r},t)\boldsymbol{E}(\boldsymbol{r},t)^3 + \ldots\end{aligned} \tag{2.54}$$

where $\chi^{(n)}(\boldsymbol{r},t)$ is the nth-order optical susceptibility of the bulk materia, which is in general a $(n+1)th$ rank tensor and ε_0 is the vacuum permittivity. In the case of anisotropic materials, the susceptibility depends on the crystal structure of the medium. While, in the case of the isotopic and homogeneous materials, such as noble metals, it plays a key role in plasmonics and the tensorial character can be neglected when only one tensorial component is of interest. In this case, the susceptibility can be characterized by scalar quantities. Moreover, the symmetries of the crystal lattice will leads to the reduction of the number of nonzero tensorial components.[6] And the higer order ones are generally dependent on time or frequency.

Based on the power dependence on the electric field, the polarization above can be divided into linear and nonlinear parts as $\boldsymbol{p}(\boldsymbol{r},t) = \boldsymbol{p}_l(\boldsymbol{r},t) + \boldsymbol{p}_{nl}(\boldsymbol{r},t)$, where $\boldsymbol{p}_l(\boldsymbol{r},t) = \varepsilon_0\chi^{(1)}(\boldsymbol{r},t)\boldsymbol{E}(\boldsymbol{r},t)$ and $\boldsymbol{p}_{nl}(t)$ is the sum of the left terms in Equation 2.54.

In order to analyze the second-order response more convenient in the following part, we specify the second-order polarization here:

$$\boldsymbol{p}_2(\boldsymbol{r},t) = \varepsilon_0\chi^{(2)}(\boldsymbol{r},t)\boldsymbol{E}(\boldsymbol{r},t)^2 \tag{2.55}$$

Meanwhile, we assume the driving EM field consists of the two co-propagating monochromatic plane waves with central frequencies ω_1 and ω_2, separately. For convenience, we also assume all fields are linearly polarzied in x direction. Hence the incident electric field can be expressed as:

$$\boldsymbol{E}(\boldsymbol{r},t) = \boldsymbol{E}_1 e^{i(\boldsymbol{k}_1\cdot\boldsymbol{r}-\omega_1 t)} + \boldsymbol{E}_2 e^{i(\boldsymbol{k}_2\cdot\boldsymbol{r}-\omega_2 t)} + cc \tag{2.56}$$

where $\boldsymbol{k}_1$ and $\boldsymbol{k}_2$ are corresponding wave vectors and cc stands for the compplex conjugation, since the electric field must be a real quantity.

By inserting Equation 2.56 into Equation 2.55, the second-order nonlinear polarization is obtained:

$$\begin{aligned}\boldsymbol{p}_2(\boldsymbol{r},t) =& \varepsilon_0\chi^{(2)}(\boldsymbol{r},t)[\boldsymbol{E}_1^2 e^{2i(\boldsymbol{k}_1\cdot\boldsymbol{r}-\omega_1 t)} + \boldsymbol{E}_2^2 e^{2i(\boldsymbol{k}_2\cdot\boldsymbol{r}-\omega_2 t)} \\ &+ 2\boldsymbol{E}_1\boldsymbol{E}_2 e^{i[(\boldsymbol{k}_1+\boldsymbol{k}_2)\cdot\boldsymbol{r}-(\omega_1+\omega_2)t]} \\ &+ 2\boldsymbol{E}_1\boldsymbol{E}_2^* e^{i[(\boldsymbol{k}_1-\boldsymbol{k}_2)\cdot\boldsymbol{r}-(\omega_1-\omega_2)t]} + cc] \\ &+ 2\varepsilon_0\chi^{(2)}(\boldsymbol{r},t)(\boldsymbol{E}_1\boldsymbol{E}_1^* + \boldsymbol{E}_2\boldsymbol{E}_2^*)\end{aligned} \tag{2.57}$$

In Equation 2.57, a series of important nonlinear processes in the bulk material are described. We will specify them later. One should note that strong, coherent nonlinear signals only can be generated when individual nonlinear sources sum up in phase. Hence, the phase-matching between two interacting fields plays a key role for the frequency conversion in samples with sizes much larger than the wavelength.

If we rewrite the second-order polarization $\boldsymbol{p}_2(\boldsymbol{r},t)$ as $\boldsymbol{p}_2(\boldsymbol{r},t) = \sum_n \boldsymbol{P}^{(2)}(\omega_n)e^{-i\omega_n t}$. Then the second-order polarizations in the different nonlinear optical processes in Equation 2.57 can be expressed as :

$$\boldsymbol{p}_2(2\omega_1) = \varepsilon_0\chi^{(2)}\boldsymbol{E}_1^2 \tag{2.58}$$

$$\boldsymbol{p}_2(2\omega_2) = \varepsilon_0\chi^{(2)}\boldsymbol{E}_2^2 \tag{2.59}$$

$$\boldsymbol{p}_2(\omega_1+\omega_2) = 2\varepsilon_0\chi^{(2)}\boldsymbol{E}_1\boldsymbol{E}_2 \tag{2.60}$$

$$\boldsymbol{p}_2(\omega_1-\omega_2) = 2\varepsilon_0\chi^{(2)}\boldsymbol{E}_1\boldsymbol{E}_2^* \tag{2.61}$$

$$\boldsymbol{p}_2(0) = 2\varepsilon_0\chi^{(2)}(\boldsymbol{E}_1\boldsymbol{E}_1^* + \boldsymbol{E}_2\boldsymbol{E}_2^*) \tag{2.62}$$

The above equations describe the most common second-order nonlinear optical processes in the bulk materials, namely second harmonic generation (SHG),[54] sum frequency generation (SFG), difference frequency generation (DFG), which are schematically illustrated in Figure 2.5 and optical rectification (OR).

In Figure 2.5, SHG, SFG and DFG are all quantified by the second order susceptibility as illustrated in Equations 2.58 to 2.61. Different

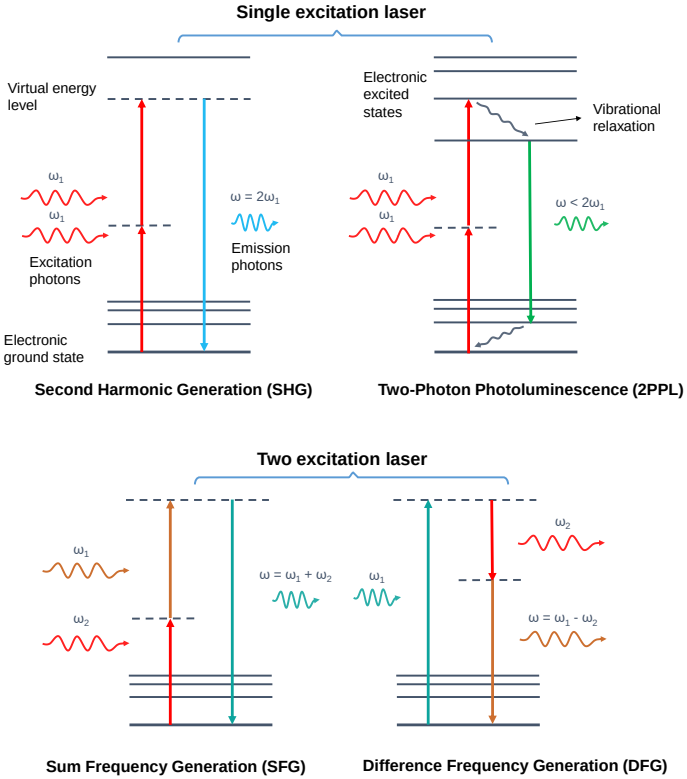

Figure 2.5. Energy diagrams for typical nonlinear optical processes including the SHG, 2PPL, SFG and DFG from the left to right diagrams, respectively.

with them, the two-photon absorption is a process related to third order susceptibility. Although both two photon induced photoluminescence (2PPL) and SHG include the process of absorbing two photons with the same frequency, SHG is a parametric effect (coherent process), while 2PPL is incoherent process. Although 2PPL is intrinsically highly spatially resolved. However, similar to harmonic generations in plasmonic nanostructures, it is also additionally influenced by local field enhancements. Finally, those nonlinear responses

can be predicted to scale with the excitation intensity when considering the collective oscillation in localized surface plasmon structures as an anharmonic oscillation. It will be introduced with the example of SHG in the following.

2.3.2 *Second harmonic generation*

Now, we focus our attention mainly on the second harmonic generation with the susceptibility described in Equation 2.58. Two parts need to be explained here, namely, the phase-matching condition[55] and the centrosymmety induced forbidden.[56]

As illustrated in Figure 2.5, SHG is a process involving electrons getting excited to the conduction band by absorbing two photons with the same frequency and then relaxing back to the ground state, emitting a new photon with double the frequency of the absorbed photons. Obviously, this is a coherent process, thus its generation requires phase-matching conditions, which is momentum conservation between the fundamental and nonlinear momentum- (k-) vectors. In other words, the coherent nonlinear response only grow over the coherence length of the interaction. Other than for the bulk materials, for particles with sizes on the order or smaller than wavelength, the phase-matching is not important anymore. Instead, the second harmonic emission from nanostructures depends strongly on their configurations.[40] The nonlinear light is scattered from the metallic nanoparticles in certain situations allowing for the separation of local surface and non-local bulk susceptibilities. We will discuss it in the following content.

It is well-established that the second-order nonlinear processes are forbidden in centrosymmetric materials within the dipolar approximation. It can be considered that if the sign of the applied E-field is changed, then the sign of the polarization must also change. However, when we apply an inverse E-field, we obtain:

$$\begin{aligned} -\boldsymbol{p}_2(2\omega) &= \varepsilon_0 \chi^{(2)}(-\boldsymbol{E})(-\boldsymbol{E}) \\ &= \varepsilon_0 \chi^{(2)} \boldsymbol{E}^2 = \boldsymbol{p}_2(2\omega) \end{aligned} \tag{2.63}$$

This case can only occurs when $-\boldsymbol{p}_2(2\omega) = 0$, which demonstrates that the nonlinear susceptibility $\chi^{(2)}$ must be zero in centrosymmetric materials. In other words, SHG is not allowed in centrosymmetric materials within the dipolar approximation. The crystal lattice in most of metals used in plasmonics retains centrosymmetry properties. However, the symmetry is broken at the interface between the centrosymmetric medium and its surroundings. Hence, a second-order nonlinear response can occur at the surfaces of the plasmonic particles. Moreover, even in symmetric materials, second-order effects also exist when higher-multipole effects are considered, in particular, the magnetic-dipole and electric-quadrupole.

The inferences above can be found and explained in a model,[57] which is widely used to study the SHG in centrosymmetric media. In this model, the second-order polarization is composed of two components. The first one is a local polarization as the contribution of the surface nonlinearity. The second is a nonlocal bulk nonlinear polarization , which is generated inside the materials and related to the higher-multiple effects mentioned in the last paragraph. They will be briefly introduced in the following.

Considering the surface contribution to the second-order response, we rewrite Equation 2.58 as:

$$\boldsymbol{p}_2^s(2\omega_1, \boldsymbol{r}) = \varepsilon_0 \chi_s^{(2)} \boldsymbol{E}_1^2 \delta(\boldsymbol{r} - \boldsymbol{r}_s) \tag{2.64}$$

where $\chi_s^{(2)}$ stands for the surface second-order susceptiblity tensor, $\boldsymbol{r}_s$ defines the surface, the δ function expresses the surface characteristic of the second-order polarization. One should notice here that the fields in Equation 2.64 are evaluated only side the materials. When we neglect the surface anisotropy, the nonlinear susceptiblity $\chi_s^{(2)}$ only has three components, namely $\chi_{s,\perp\perp\perp}^{(2)}$, $\chi_{s,\perp\parallel\parallel}^{(2)}$ $\chi_{s,\parallel\perp\parallel}^{(2)}$. Here, $\perp$ and $\parallel$ mean the direction perpendicular and tangent to the interface, respectively. In plasmonics, the component $\chi_{s,\perp\perp\perp}^{(2)}$ is the dominated one by the magnitude by 1 order.

Beyond the electric dipole approximation, the nonlocal bulk nonlinear polarization is also possible. One can write it as:

$$\begin{aligned} \boldsymbol{p}_2^b(2\omega_1, \boldsymbol{r}) =& \gamma \bigtriangledown_i [\boldsymbol{E}(\omega, \boldsymbol{r})]^2 + \delta' [\boldsymbol{E}(\omega, \boldsymbol{r}) \cdot \bigtriangledown] \boldsymbol{E}(\omega, \boldsymbol{r}) \\ &+ \beta [\bigtriangledown \cdot \boldsymbol{E}(\omega, \boldsymbol{r})] \boldsymbol{E}(\omega, \boldsymbol{r}) + \zeta \boldsymbol{E}(\omega, \boldsymbol{r}) \bigtriangledown \boldsymbol{E}(\omega, \boldsymbol{r}) \end{aligned} \tag{2.65}$$

where γ, δ' β ζ are material physical parameters related to the material properties describing the magnetic dipole and electric quadrupole interactions.

Considering the material is homogeneous, the third term in Equation 2.65 can be neglected. The second term is also usually neglected in most theoretical models due to the transverse character of the E-field at the fundamental frequency when the plane wave propagate in the homogeneous materials. Moreover, for the noble metals, the ratio between δ' and γ is of the order of the ratio between the damping frequency and frequency ω. This ratio can also be neglected at optical frequencies. The anisotropy parameter ζ in the noble metals has a nearly negligible value.

In the experiment, it is a big challenge to separate the surface and bulk contribution to the nonlinear response. However, it is proven that the bulk contributions are much weaker than the surface contributions.[58] Though the bulk contribution to the second-order nonlinear response in plasmonics is weak, one must still consider it together with the surface contribution to describe the nonlinear plasmonic systems dependence on the experimental conditions. The fundamental question related to the exact origin of SHG in metallic nanostructures is still under investigation. The contribution of the interband and intraband transitions, the enhancement effect from the intrinsic material and extrinsic structure resonances should always be considered and investigated in both theoretical and experimental research.

Regarding the enhancement effect in the nonlinear response of the plasmonic strucutres, two mechanisms are generally considered. The first one is that plasmons enhance the incident field at the fundamental frequency. In this mechanism, special structures which can

possess strong field localization are favorable candidates to boost the nonlinear response. The second one is that plasmons amplify the nonlinear emission efficiency, in general, by coupling the nonlinear signal to radiative localized surface plasmon modes. Both mechanisms are considered and play key roles in our hybrid systems.

2.3.3 *Anharmonic oscillation model*

As discussed above, the nonlinear susceptibility is the key to describe the nonlinear optical effect. For the nonlinear optical crystals, the nonlinear optical response is generally far off their material resonances. In this case, the nonlinear optical susceptibility can be considered as frequency-independent. However, the frequency dependence of the nonlinear susceptibilities will plays an increasingly important role as the fundamental or nonlinear optical frequency moves closer to the material resonance.

Consequently, a basic model based on the Lorentz model will be introduced to determine the frequency-dependent nonlinear susceptibilities for n^{th} harmonic generation. The classical Lorentz model which describes the harmonic oscillation of the nucleus-bounded electrons in an external E-field has been introduced in Section 2.2. Now, we will consider the case that the external electric field strength is high and induces large displacements of the electrons from the equilibrium positions. The nonlinear restoring term must also be included in the restoring force. Thus we include higher order corrections in the Taylor series of the restoring (binding) potential $V(x)$:

$$V(x) = \frac{1}{2}m_e\omega_0^2x^2 + \frac{1}{3}m_e a_2 x^3 + \frac{1}{4}m_e a_3 x^4 + \dots \tag{2.66}$$

Here $a_n (n = 1, 2, 3\dots)$ are coefficients that describe the strength of the n-th order of the anharmonicities of the potential V. Taking the negative derivative to the spatial coordinate x, the restoring

force is delivered and then inserted into the Lorentz model, a driven anharmonic oscillation is described as:

$$\ddot{x}(t) + \gamma\dot{x}(t) + \omega_0^2 x(t) + \sum_{n\geqslant 2} a_n [x(t)]^n = -\frac{e}{m_e} \boldsymbol{E}_0 e^{i\omega t}, \tag{2.67}$$

We will neglect the summation and only consider the first non-zero nonlinear term in Equation 2.67 for convenience in the following. Unfortunately, we cannot solve the differential equation 2.67 analytically. Instead, we can take a perturbative approach to solve it with a perturbative ansatz for $x(t)$:

$$x(t) = x_0(t) + a_n x_1(t) + a_n^2 x_2(t) + \ldots \tag{2.68}$$

Now we insert Equation 2.68 into Equation 2.67 and then divide the motion equation 2.67 into two according to the order of the perturbation (zeroth and first order):

$$\ddot{x}_0(t) + \gamma\dot{x}_0(t) + \omega_0^2 x_0(t) = -\frac{e}{m_e} E(t) \tag{2.69}$$

$$\ddot{x}_1(t) + \gamma\dot{x}_1(t) + \omega_0^2 x_1(t) = -[x_0(t)]^n \tag{2.70}$$

The Equation 2.69 is completely equivalent to the motion equation of the classical Lorentz model introduced in Equation 2.19. Hence, the solution in the frequency domain of Equation 2.69 is given by:

$$\boldsymbol{x}_0(\omega) = \frac{e}{m_e} \frac{1}{\omega^2 - \omega_0^2 + i\gamma\omega} \boldsymbol{E}(\omega) \tag{2.71}$$

In order to simplify the next steps, we here define a linear response function:

$$g(\omega) = -\frac{1}{\omega^2 - \omega_0^2 + i\gamma\omega} \tag{2.72}$$

In equation 2.25, one can clearly see that this linear response function is proportional to the linear susceptibility.

Now the solution 2.69 can be written as:

$$\boldsymbol{x}_0(\omega) = \frac{e}{m_e} g(\omega) \boldsymbol{E}(\omega) \tag{2.73}$$

We assume a uniform monochromatic illumination $E(t) = E_1 e^{-i\omega_1 t}$ for simplicity. It can be expressed in the frequency domain in terms of a delta function $E(\omega) = 2\pi E_1 \delta(\omega - \omega_1)$. Then the solution in 2.73 can rewritten again as:

$$\boldsymbol{x}_0(\omega) = \frac{e}{m_e} g(\omega_1) E_1 \delta(\omega - \omega_1) \tag{2.74}$$

corresponding to the time domain solution is given by Fourier transform:

$$\boldsymbol{x}_0(t) = \frac{e}{m_e} g(\omega_1) E_1 e^{-i\omega_1 t} \tag{2.75}$$

Now we can continue to solve the first order of perturbation. If we compare Equations 2.69 and 2.70, they have the same functional form on the left. on the right part, the zeroth order displacement $x_0(t)$ plays the role of an external field. Hence, we can express the solution for the displacement $x_1(\omega) = -g(\omega)\mathcal{F}[x_0(t)^n]$, where $\mathcal{F}$ stands for the Fourier transform. Then we insert $x_0(t)$ into it and then transform back to the time domain. The displacement $x_1(t)$ is obtained:

$$\boldsymbol{x}_1(t) = (-1)^n (\frac{e}{m_e})^n [g(\omega_1)]^n g(n\omega_1) E_1^n \cdot e^{-i\omega_1 t} \tag{2.76}$$

According to the relation between the displacement and the polarization, which is analogous to the case of the classical Lorentz model (see Equations 2.20 2.21 2.22 2.25), we can express the nonlinear susceptibilities of nth-order as:

$$\begin{aligned} P^{(n)}(t) &= \varepsilon_0 \chi^{(n)} E(t)^n = -e n_e a_n x_1(t) \\ &= (-1)^n a_n \frac{e^{n+1}}{m_e^n} [g(\omega_1)]^n g(n\omega_1) E(t)^n \end{aligned} \tag{2.77}$$

Then nth order nonlinear susceptibility for the nth harmonic generation is obtained:

$$\chi^{(n)}(\omega) = (-1)^n a_n \frac{e^{n+1}}{\varepsilon_0 m_e^n} [g(\omega)]^n g(n\omega) \tag{2.78}$$

Equation 2.78 is the most important conclusion in this section. It relates the nth nonlinear susceptibility $\chi^{(n)}(\omega)$ to the nth power of

the linear response function $g(\omega)$. Meanwhile, this linear response function leads to a response of the generation frequency with $g(n\omega)$ in the nonlinear susceptibility function. Therefore, we can get the conclusion that the linear optical properties of the medium largely determine its nonlinear response.

Moreover, this results provide us with critical guidance to model the resonance shape and even nonlinear frequency of SHG and design the systems with the high SHG efficiency. A brief introduction and derivation of the SHG efficiency will be given in the following. As mentioned above, the source term of the nonlinear response is the plasmon oscillation amplitude $x_0(t)$. And it is directly proportional to the effective electric field enhancement in the near field of the plasmonic nano structures.

As mentioned above, the solution $x_1(\omega)$ can be expressed as $x_1(\omega) = -g(\omega)\mathcal{F}[x_0(t)^2]$, where $\mathcal{F}$ stands for the Fourier transform. The macroscopic SH polarization $P_{SH}(\omega)$ is the source term for the SH and directly proportional to the perturbed solution $\boldsymbol{x}_1(\omega)$. Therefore, the SH intensity radiated into the far-field can be expressed as:

$$I_{SH}(\omega) \sim \mid E_{SH}(\omega) \mid^2 \sim \mid \omega \cdot \boldsymbol{x}_1(\omega) \mid^2 \tag{2.79}$$

Thus, this anharmonic model can be used to predict not only the shape of the SH resonance but also the SH intensity. For sure, it is a purely classical model to do simple prediction while neglecting a lot of effect, which can notbe accounted for by this model. Therefore, it cannot replace the full quantitative electrodynamic simulations in certain real systems. However, it gives an intuitive understanding of the microscopic origin of the nonlinear optical processes in plasmonic systems.

Notably, the maximum near-field enhancements always take place at the red-shifted wavelength with respect to its corresponding far-field spectrum due to the damped nature of the plasmon oscillator. This universal phenomenon is also explained by a driven and damped harmonic oscillator.[59] As a result, the plasmon oscillation amplitude

does not peak at the resonance frequency ω_0. Instead, the peak is at a red-shifted near-field resonance frequency $\omega_{NF} = \sqrt{\omega_0^2 - 2\gamma^2}$.

According to the derivation of the $x(\omega)$ in the anharmonic oscillator model, the absolute value of the plasmon oscillation amplitude is $\mid x_0(\omega) \mid = \mid g(\omega) \cdot E(\omega) \mid$. For continuous illumination with $E(t) = E_0 \cdot e^{-i\omega t}$, we have:

$$\mid x_0(\omega) \mid = \frac{2\pi e E_0}{m} \frac{1}{\sqrt{(\omega^2 - \omega_0^2)^2 + 4\gamma^2\omega^2}} \tag{2.80}$$

Thus, the peak value of the oscillation amplitude at the red-shifted near-field resonance frequency ω_{NF} should be calculated as:

$$\begin{aligned} \mid x_0(\omega_{NF}) \mid &= \frac{2\pi e E_1}{m} \frac{1}{2\gamma\sqrt{\omega_0^2 - \gamma^2}} \\ &\simeq \frac{2\pi e E_1}{m} \frac{1}{2\gamma\omega_0} \sim \frac{1}{\gamma\omega_0} \end{aligned} \tag{2.81}$$

Here, we considered $\gamma \ll \omega_0$ in plasmonic systems.

Now, we can briefly conclude on the influence factors on the linear and nonlinear response in this classical model based on the above derivations. Firstly, the resonance position ω_0 influences the near-field enhancement. It can be easily understood when the term ω_0^2 is considered as the restoring force in our anharmonic oscillator. The lower resonance ω_0 stands for a smaller restoring force and thus results in a bigger oscillation amplitude. Secondly, the damping constant γ largely determine the amplitude of the oscillation, namely, a long lifetime τ or a narrow linewidth of the plasmon resonant corresponding to the smaller damping γ leading to higher field enhancements. Finally, the nonlinear effect scales with a higher power of the local near-field enhancement. In particular, the SH response scales with the $4th$ power of the plasmon oscillation amplitude $x_0(t)$. Combining Equations 2.79 and 2.81 and also the relation $\gamma \simeq \triangle\omega$, we can clearly see that the SH intensity is proportional to the $4th$ power of the Q factor, which is defined by $\omega/\triangle\omega$.

2.4 WHISPERING GALLERY MODES

Optical cavities plays an important role in modern atomic, molecular, and optical physics. They are widely used in a great deal of optical devices, such as lasers, narrow filters, optical switching, nonlinear optical devices and also act as powerful tools to enhance the detection sensitivity, nonlinear interactions, and quantum dynamics in measurements and nonlinear optical experiments.[60–64] Bulk optical cavities in some applications, however, meet big challenges caused by their size, alignment and stability problems. In this situation, the integrated optics approach, particularly the integrated ring resonators, was proposed to overcome most of these problems.[65] Another class of miniaturized optical resonators that emerges rapidly is the dielectric structures having circular symmetry, which sustain the named *whispering gallery modes*, that are the main structure introduced in this chapter.

FIGURE 2.6. Photographs of (a) St Paul's Cathedral in London. (b) Temple of Heaven in Beijing.

WGMs were first discovered in acoustic structures. In some old buildings, such as the dome of St Paul's Cathedral in London and the Temple of Heaven in Beijing (see the photographs in Figure

2.6), one can found a common characteristic. People can hear at any point around the gallery with an ear held to the wall when a whisper against the wall at any other point around the gallery occurs. John William Strutt (Lord Rayleigh) who observed and studied this characteristic defined it as *whispering gallery modes*.[66]

Similarly, optical whispering gallery modes take places when light waves are confined in the dielectric microstructures where the refractive index is greater than that of outside material as a consequence of internal total reflection. When the light beam returns to the incoming point in phase, a standing wave is formed. Figure 2.7 illustrates the geometrical optics and wave optics representation of a whispering gallery mode. By confining light as WGMs on the cavity interface, The photon storage time can be very long, i.e. exceeding a microsecond.[67] Based on this, the low threshold optical effects such as lasing and nonlinear wave generation can be realized.[68, 69] Moreover, the Q factor of these whispering gallery mode resonators can be as high as several billions.[67] This ability of confining light for a significant long time in a micro-size volume have profound implications for various areas.[70–75]

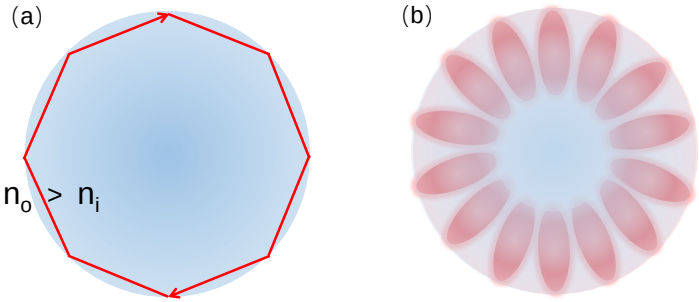

Figure 2.7. (a) Geometrical optics and (b) wave optics representation of a whispering gallery mode.

2.4.1 *Basic properties*

Whispering gallery mode microcavities as one important category of microcavities have the advantages of *low mode volume*, *a high quality factor* and *a large optical field strength* which are induced by the enhanced light-matter iteration. Those properties are of great interest for lasers, quantum optics, optical and RF communications and sensors.[76, 77] Thus they are extensively studied by researchers. Up to now, various structures have been designed and investigated for sustaining whispering gallery modes. They are not limited to spherical.[76, 78] Cylindrical-,[79] toroidal-,[80] bottle-,[81] and bubble-shaped[82] dielectric resonators have been also explored in abundant application. Specific structures are designed for certain purposes of applications and research. In order to characterize them, basically, there are key parameters needed to be considered: *quality factor* and *resonant position* of a whispering gallery mode.

Before we introduce those two parameters, we first need to make it clear that the optical modes of a spherical-like dielectric cavity can be characterized by a set of four quantum numbers (r, m, l, p), where r denotes the radial mode order, l and m the angular and azimuthal mode numbers, and p the polarization (TE or TM). Depending on these mode numbers, the WGM wavelengths vary. For azimuthal and radial modes, the spatial distribution of the electromagnetic field also depends on the mode numbers as illustrated in Figure 2.8. In other cases of various shape cavities, the optical modes can be quite complicated. Moreover, different systems have specific coupling and exciting themes, and there are always defects of geometry and material presenting during the fabrication process of the cavities. It is impossible to predict precise parameters including the resonance positions and Q factors for each whispering gallery resonator. Here, we only consider the simple analysis for the perfect sphere-shaped whispering gallery resonators.

Approximated positions of resonances

As one of the important parameters, the resonance position can be directly measured in the WGMs resonators through excited by proper

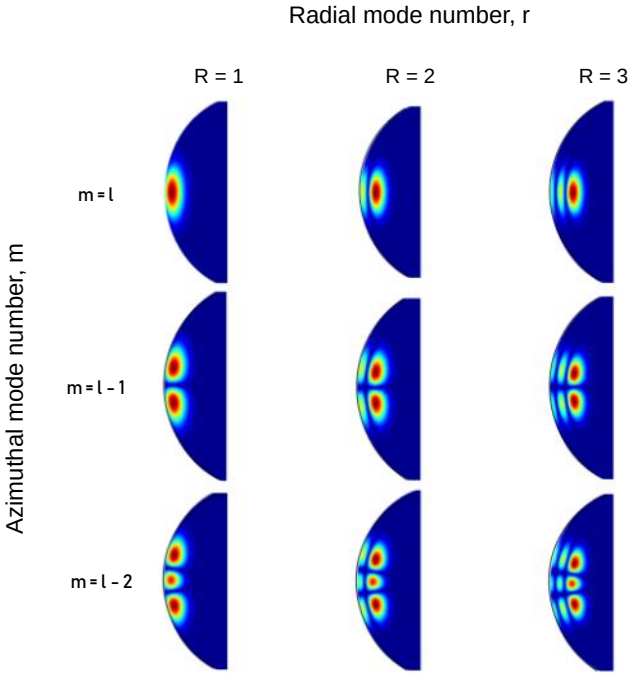

Figure 2.8. Distribution of electric field with different azimuthal and radial mode numbers.[83]

coupling methods. The main coupling methods will be introduced later in the next subsection. However, in general, the resonant position need be predicted in advance in order to design proper systems. Basically, the methods for predicting the resonance position of whispering gallery modes can be divided into two types: one is an analytic model based on the classical Mie Scattering theory[84] and the other one is the computational simulation based on the Finite-Difference Time-Domain (FDTD) or Finite Element Method (FEM).[85] Each method has advantages and disadvantages and still can be divided into different categories.

Considering the planar graph of a whispering gallery cavity as shown in Figure 2.7 (a), light is confined near the circular boundary of the resonator as a result of the total internal reflection. The simple geometric picture shown in Figure 2.7 leads to the concept of resonances. For large microsphere (diameter is larger than the wavelength of the light), the trapped ray propagates close to the surface, and traverses a distance of circumference of the microcavity in a round trip. If one round trip exactly equals l times wavelength in the medium with the effective refractive index n_{eff}, then one can expects a standing wave to occur. The condition can be described with the following equation:

$$l\lambda = Ln_{eff} \tag{2.82}$$

However, whispering gallery mode resonators can sustain transverse electric (TE) modes and transverse magnetic (TM) modes. Thus, correction term needs be added to Equation 2.82 to deduce more accurate resonance wavelengths of the cavity. In 1992, the framework of explicit asymptotic expansion of the characteristics equation in powers of $v^{-1/3}$ was developed by Lam et al. for numerical approximation of the resonances, where $v = m + 1/2$.[84] Here, we only consider the case of $l = m$

$$\begin{aligned}\frac{n}{\lambda_{r,m}} =& \frac{1}{\pi D}\Big[v + 2^{-1/3}A_r v^{1/3} - \frac{P}{(n^2-1)^{1/2}} + \frac{3}{10}2^{-2/3}{A_r}^2 v^{-1/3} \\ &- \frac{2^{-1/3}P(n^2 - 2P^2/3)}{(n^2-1)^{3/2}}A_r v^{-2/3} + O(v^{-1})\Big],\end{aligned} \tag{2.83}$$

$$P = \begin{cases} n & for\ TE\ modes \\ 1/n & for\ TM\ modes \end{cases} \tag{2.84}$$

where n is the refractive index of the whispering gallery cavity, A_r is the rth zero of the Airy function Ai(-z), D is the diameter of the whispering gallery resonator. Afterwards, some improved models were developed but still based on the basis of this asymptotic expansion. These analytic models used in the literature are comparatively efficient to calculate. However, these models all rely on the

assumption that whispering gallery cavities are perfect spheres without any roughness and that the medium of the structure is totally homogeneous in terms of the refractive index.

Compared to efficient analytic models, the Finite-Difference Time-Domain technique (FDTD) is more flexible. It simulates the evolution of electromagnetic fields by discretizing a volume into a $3D$ spatial lattice. Then Maxwell's Equations are used to solve every point on the lattice, for a finite amount of time increments. In these models, a certain geometry and dielectric medium of the whispering gallery resonators can be defined and placed in the discretized volume. FDTD shows a big advantage with its ability to incorporate effects such as various geometries and material inhomogeneities. It means the specific modes or resonant position can be reliably identified, and tailored by altering the initial configuration of the resonator.

In this thesis, regarding the case that only a rough wavelength position needs to be known and the structure is a complicated coupled system, the analytic models shown in the Equation 2.83 is picked to estimate the wavelength position of the WGMs in the pure microfiber cavities.

Quality factor

Q-factor is another fundamental parameter that is conventionally used to quantify the quality of any optical cavities. As mentioned above, the electromagnetic wave is confined in the small volume as the WGMs. As the result of the minimal reflection losses and potentially very low material absorption, extraordinarily high quality factor $Q = \lambda/\Delta\lambda$ can be achieved in those microresonators, where λ is the resonance wavelength and $\Delta\lambda$ is the full width at the half maximum of the resonance. More basic definition of Q-factor is

$$Q = \omega\tau \tag{2.85}$$

where ω is the optical angular frequency of the resonant mode. τ is the cavity photon life-time, which means the time effectively spent by the light wave within the cavity on resonance. Q-factor indicates the energy storage ability of microcavities. It is easily seen that longer

resonant lifetime (narrower resonance line-width) corresponds to a bigger Q factor. In the simplest ideal case where material absorption is the only loss channel:

$$Q_{abs} = \frac{2\pi n}{\alpha\lambda} \tag{2.86}$$

where n and α are the refractive index and absorption coefficient at wavelength λ, respectively. However, in more general cases, a set of loss channels need be considered.[85] More comprehensively, the Q-factor of a microcavity for a specific WGM, with optical frequency :

$$Q^{-1} = \sum_i Q_i^{-1} \tag{2.87}$$

where Q represents a set of surface scattering loss factor Q_{scatt}, radiative loss factor Q_{rad}, material absorption loss factor Q_{mat} and contaminant loss factor Q_{con}.

Equation 2.86 already indicates the material absorption loss considering the linear absorption coefficient α of the material. While, the refractive index of a dielectric material is given by:

$$n = \tilde{n} + i\kappa \tag{2.88}$$

where κ is the extinction coefficient and characterizes the incoming radiation absorption of a material.

The scattering loss channel is mainly caused by the surface inhomogeneity-induced Rayleigh scattering during the resonant recirculation. The scattering loss factor can be expressed by:

$$Q_{scatt} = \frac{\lambda^2 R}{\pi^2 \sigma_{rms}^2 B} \tag{2.89}$$

where σ_{rms} is the root-mean-squared size and B is the correlation length, or the length of inhomogeneity. In order to have a high quality microcavity, both the size and the length of inhomogeneity need to be minimized. Meanwhile, one can clearly see that the Q_{scatt} is linearly related to the cavity radius R.

The radiative loss factor Q_{rad} is an intrinsic parameter, which is determined by the curved boundaries of the microcavities. Regarding to the geometries, light with the certain wavelength experiences less total internal reflection during the recirculation in small microcavities with larger curvature. As a result, the efficiency of light confinement is reduced. In general, the radiative loss factor can be expressed by:

$$Q_{rad} = \frac{Re(k_{r,m})}{Im(k_{r,m})} = \frac{1}{2}(m+\frac{1}{2})n^{(2p-1)}\sqrt{n^2-1}e^{2T_{r,m}} \tag{2.90}$$

where

$$P = \begin{cases} 0 & \text{for TE modes} \\ 1/n & \text{for TM modes} \end{cases}$$

$$T_{r,m} = (m+\frac{1}{2})[\beta_{r,m} - \tanh\beta_{r,m}]$$

and,

$$\begin{aligned} \beta_{r,m} = \cosh^{-1}\{n[1-(\frac{1}{m+\frac{1}{2}})(A_r\sqrt[3]{\frac{2m+1}{4}} \\ + \frac{n^{1-2p}}{\sqrt{n^2-1}})]^{-1}\} \end{aligned} \tag{2.91}$$

where m is the angular mode number and r is radial mode number, which is illustrated in Figure 2.8.

The Q factor is decided by various elements, not only the morphology and dielectric properties, but also some minute characteristics, such as the surface roughness, material inhomogeneities and so on. Thus, predicting the Q factor of the microcavities represents a principal challenge. There are still two main methods namely analytic models and FDTD computational tools to predict the quality factors of WGM resonators. The analytic models generally rely on the assumption that the resonators are perfect spheres without any surface roughness. Meanwhile, the refractive index of the medium is consistent in the resonators and the total radiated power is collected in a certain long time. As mentioned above, in the FDTD method, varing

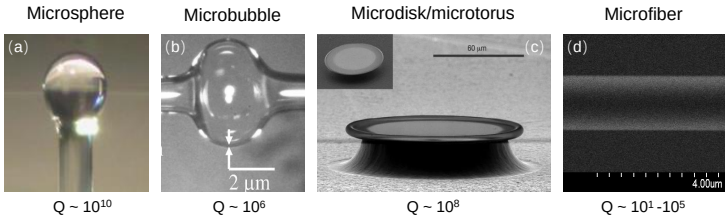

Figure 2.9. (a) microsphere,[86, 87] (b) microbubble,[82] (c) microdisk,[80] (d) microfiber and their corresponding order of typical high Q-factors.

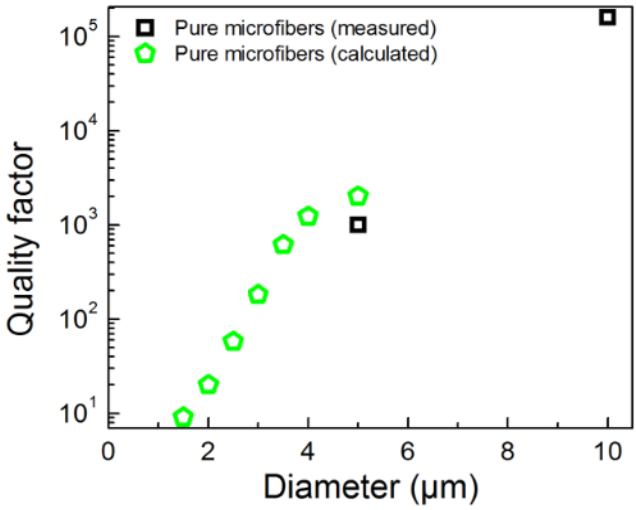

Figure 2.10. Quality factors of pure microfibers (black hollow squares for measured results, green hollow pentagons for calculated results.[88]

of the resonator geometry, refractive index, material inhomogeneities can be considered and accommodated.

Figure 2.9 shows the images of four basic WGM microresonator structures and their responding order of typcial quality factors. They all consist of fused silica. In Figure 2.9(d) a broad range of Q factors are pointed out on purpose to demonstrate the flexibility of the microfibers in various of applications. The measured Q factors of pure

microfibers with 5 µm and 10 µm and calculated ones with smaller diameters are shown in Figure 2.10. Compared to the structures depicted in Figure 2.9(a-c) which are designed to achieve super high-Q factor in order to realize high-sensitivity sensors, the microfibers are much easier to be customized with the certain diameters to get the desired Q factors for the specific aims.

Free spectral range

The free spectral range (FSR) $\Delta\lambda$ is the definition of the distance between two adjacent optical modes with angular mode number m and $m-1$. In a whispering gallery resonator, we have the equation for the modes with the radial mode number $r = 1$ (fundamental modes) as following:

$$2n_{eff}\pi R = m\lambda_m = (m-1)\lambda_{m-1} = (m-1)(\lambda_m + \Delta\lambda) \tag{2.92}$$

where n_{eff} is the effective index, R is the radius of the whispering gallery resonator, λ_m and λ_{m-1} presents the wavlength of two adjacent modes. When m is large, the FSR can be considered as constant and derived from Equation 2.92:

$$\Delta\lambda = \frac{\lambda_m^2}{2n_{eff}\pi R} \tag{2.93}$$

It is clearly seen that whispering gallery resonators with a smaller radius have bigger FSR, which is also proven in our later measurement.

2.4.2 *Fabrication and excitation schemes*

As mentioned above, WGM resonators vary a lot in terms of their geometries. Each of them having its pros and cons. Meanwhile, WGRs are made from a variety of materials from polymer to diamond.[89, 90] In order to realize certain goals with a given type, three main parameters must be considered: the expected value of the Q-factor, the

complexity of fabrication, and the integrability. The most common materials used to fabricate WGRs is silicon dioxide. And the most commonly used microresonator structures are spherical microresonators. Two main fabrication techniques for glass microspherical resonators are melting process and sol-gel chemistry.[91, 92] At the early stage, some melting methodologies such as dropping the melting glass onto the rotating plate, melting of glass levitated in high magnetic fields[93] rotating electric arc melting[94] and microwave plasma torch melting[95]. With those methods, the microspheres generally are big and the size of them is quite difficult to be controlled precisely.

Now an improved method is developed in which the fiber are heated until they soften and then are inserted it into the splicer arm which generates electric arcs to melt the fiber tip to induce the spherical microcavity.[87] The microspheres can be controlled by modulating the number of electric arcs. A minimum diameter around 40 μm can be fabricated by this fiber splicing technique. The microresonators with several ten or hundreds of μm can sustain WGMs with Q factors up to 10^8. Smaller microspheres are generally produced by a chemical approach such as the sol-gel process mentioned before. It is a relatively flexible and cheap method and it can even be combined with the melting process. The typical diameter of those microspheres are several hundreds nm to several μm.

Besides the spherical structures, the cylindrical, toroidal and microdisk WGM resonators are the most general types of whispering-gallery microresonators. The main topic we will discuss in this thesis is the nonlinear optical response from the coupling system between the gold nano particles and the microfibers, which belongs to the cylindrical WGM microresonators. Those microresonators are easy to be fabricated. In general, they are fabricated from silica optical fibers by removing that jacket and pulling with fire. This is also the fabrication process we used to produce the WGM resonators. It will be introduced detail in the Chapter 3. By modulating the pulling strength, the diameters of the fibers and the length of the shoulder part can be precisely controlled.

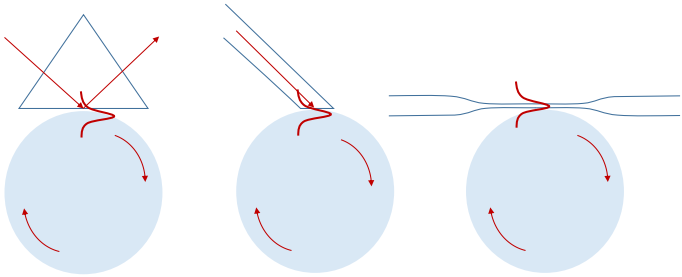

Figure 2.11. Three basic light-coupling methods to excite the WGMs in a microcavity with the help of (a) a prism, (b) a polished microresonator (c) an optical fiber.

We introduced the main types of the WGM resonators and fabrication processes. Now an obvious question arises: how can the WGMs be efficiently excited in a micrometer-sized sphere? Namely, how can the light couple in or out of microresonators efficiently? Initially, a free-space laser beam is focused onto the edge of the sphere and enters it. The result is certainly not good enough. The interaction between the resonator and laser beam is very small since the scattering cross section of a microsphere is much smaller than the cross section of the beam. Exciting the certain high-Q modes of a microsphere with the free-space beam with very small coupling efficiency is a big challenge even in theory. Afterwards, the efficient coupling method via the overlap of evanescent fields is developed. The laser beam is coupled into the microresonator from an adjacent guiding structure such as *a prism*,[85, 96] *a polished fiber*,[97] *an optical fiber*,[98, 99] and so on. A typical 80 – 90% coupling efficiency can be achieved with a prism(see the Figure 2.11). While, the coupling efficiency using an adiabatic tapered fiber can reach to 99.99%, which is almost perfect coupling. Those methods are in general used to excited the WGMs with relatively high-Q factors, for example 10^8. In this thesis, a totally different coupling method is used due to the relative low-Q factors of the coupling system between the gold nanoparticles and the microfibers. The localized surface plasmon resonance of a gold nanoparticle on the surface of a microfiber is firstly excited with a

free-space beam and then the WGMs of the microcavity are excited by the evanescent fields from this plasmon resonance.

3

EXPERIMENTAL TECHNIQUES

3.1 FIBER PREPARATION

Silica miro-/nanofibers have been widely used in a series of investigations and applications and play a key role in many modern techonologies, such as sensing, medical, communications and so on. In 1887, C. V. Boys et al. already reported a way to make silica filaments from heated-minerals and researched their mechanical properties.[100] The optical properties and their applications became a hot research topic after almost one century when the optical waveguide theory was set up completely. Afterwards, the laser- and flame-heated method to make thinner fibers from normal fibers are developed very soon. However, the diameters of fibers fabricated with those methods are generally in the range from several micrometers to several tens micrometers.[101] Still later, L. Tong, G. Brambilla, M. Sumetsky, J. M. Ward et al. improved the heating sources and the heating methods in the micro-/nanofibers preparation technique successively.[102–104] The quality of micro-/nanofibers is improved gradually. Nowadays, there are different forming technologies to fabricate silica micro-/ nanofibers according to the different uses. Except the above method of tapering normal fibers, directly drawing from bulk glasses is another key technique.[105] Based on those methods, the diameters of silica micro-/nanofibers extends from a few nanometers to a few micrometers.

At beginning, tapering fibers to decrease the diameter of an optical fiber is mainly used to achieve anomalous dispersion at femtosecond laser wavelengths, which is critical to get solitonic supercontinuum generation.[106–108] Instead of acting as the wave-guide, the microfibers used in this thesis act as the whispering gallery modes cavities and are fabricated from the single mode fibers (SMF) by a home-made heating fiber pulling machine. In my case, it is the single mode fiber SMF-28 manufactured by Corning Inc..

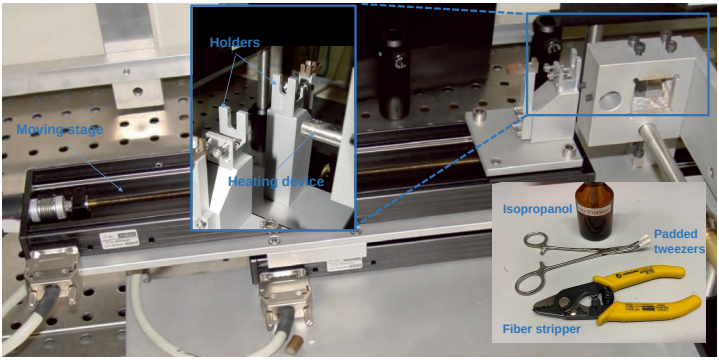

Figure 3.1. Photos of the fiber pulling machine and equipment needed to strip and clean optical fibers

The first step of preparing the fibers is to remove the protection polymer coating of the fiber by using a standard *fiber optic stripper* (i.e. Clauss, model CFS-2). Then moisturise the piece of fiber without coating using padded tweezers with isopropanol (CHO). The end of the cleaning fiber can be fixed to two holders in the fiber pulling machine. As another main component of the pulling machine, a motor is used to control the movement of two holders along a moving stage. In this process, a heating device travels along the fiber axis. A certain program will give detailed instruction to the motor according to the

parameters we set, such as the diameter of the tapered fiber, the length of the pulled waist and so on. A mixture of 30% propane and 70% butane and oxygen running as stable gas flow provides the flame. The temperature distribution of the heating device, the motion of the heating device with respect to the fiber during the tapering process and the initial geometry of the normal fiber decide the shape of the tapered fiber. The setup photo is shown in Figure 3.1.

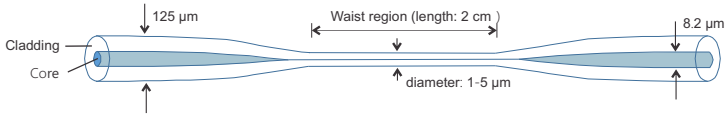

Figure 3.2. Sketch of a typical tapered fiber with a waist region (2 cm length and 1 – 5 μm diameter

Figure 3.2 shows the sketch of a typcial tapered SMF-28 fiber with an original core diameter of 8.2 μm, a cladding diameter of 125 μm. The length of waist region varies around 2 cm and the diameter is in the range of 1 – 5 μm. The coupled cavities is prepared by coating gold nanoparticles onto the surface of the waist region of the fibers.

3.2 PREPARATION OF GOLD NANOPARTICLES

Gold nanoparticles (AuNPs) have been widely used and provide a powerful platform in a broad range of applications, such as bionanotechnology, biomedical and so on. They have unique physical, stable chemical properties, and multiple surface functionalities, they especially show a big potential in enhancing the interaction between the light and matter. The optical and electronic properties of AuNPs can be adjusted by changing their size, shape, surface chemistry and aggregation state. A wide array of solution based approaches has been developed in the past few decades to control them.[109–115] The

synthesis method developed fast after Turkevich et al. created AuNPs in 1951 by treating hydrogen tetrachloroaurate ($HAuCl_4$) with citric acid in boiling water.[116] This section will introduce the main preparation and purification process of single-crystalline AuNPs used in this thesis as following:

Chemicals: Chloroauric acid trihydrate ($HAuCl_4 \cdot 3H_2O$), sodium borohydride ($NaBH_4$), silver nitrate (AgNO), trisodium citrate (TSC), cetyltrimethylammonium chloride (CTAC), L-ascorbic acid (AA) and hydroquinone (HQ) were all purchased from Sigma-Aldrich. Cetyltrimethylammonium bromide (CTAB) was obtained from Alfa Aesar. Ammonia solution (NH_2O) was ordered from E. Merck (Germany). Hydrogen peroxide solution (H_2O_2) was purchased from Aladdin Chemical (China). All chemicals were used without further purification. Deionized (DI) water (Direct-Q@5UV, Millipore) with a resistivity of 18.2 MΩ cm was used throughout the experiments. Tetrachloropalladic acid (H_2PdCl_4) solution was prepared by dissolving palladium dichloride($PdCl_2$) (0.07 g, 0.2 mmol) in HCl solution (4 mL, 0.2 M), followed by dilution with deionized water (200 mL).

Preparation of the Au Nanorods: Single-crystalline gold nanorods used in this thesis were synthesized using an alternative seed-mediated method by exchanging the reducing agent with an excess of hydroquinone[117, 118] First, $NaBH_4$ solution(600 Ml, 0.01 M) was quickly added into CTAB solution (mixed solution composed of 43.4 μL of a 0.11518 M$HAuCl_4$ and 5 Ml water) while forced stirring. 2 min stirring results in a browning yellow solution as seed solution. Then it was kept at room temperature at least 30 minutes until usage. The solution composed of AgNO (5 Ml, 0.1 M) and $HAuCl_4$ (4.341 Ml, 0.11518 M) were added to an aqueous CTAB solution (dissolving 36.45g CTAB into 1000 Ml of purified water). At least 5 min later, HQ solution (50 Ml, 0.1 M) was added while stirring. After 2 min, the seed solution (24 Ml) was then added. The resultant solution was kept at 32 ℃ for 48 h.

Purification of the Au Nanorods: CTAC (11.34 g, 0.0354 mol) was dissolved in purified water (88 ml) in a graduated cylinder. The as-prepared gold nanorods solution (140 ml) was centrifuged for 30 min

at 8500 rcf to reduce the volume to 12 ml. The resulting gold nanorods dispersion was then added to the CTAC solution (CTAC: 0.354 M, CTAB: 0.012 M). The colloidal solution was kept 21 h. Then 95 Ml of the supernatant was decanted. The remaining solution (5 ML) was diluted with Milli-Q water (CTAC: 0.177 M, CTAB:0.006 M). After 24 h, by carefully removing the brown supernatant, the brown sediment was left for the further use.

Preparation of the Au Nanobipyramids: The Au nanobipyramids (NBPs) were grown using the seed-mediated growth method, as reported in the previous works.[119, 120] Specifically, the seed solution was prepared by adding a freshly prepared, ice-cold $NaBH_4$ solution (150 µL, 0.01 M) into an aqueous solution composed of DI water (9.625 mL), $HAuCl_4$ (125 µL, 0.01 M) and TSC (250 µL, 0.01 M). The resultant seed solution was stirred for 30 s and then left undisturbed at 35℃ for 2 h before further use. The growth solution was prepared through the sequential addition of $HAuCl_4$ (2 mL, 0.01 M), AgNO (400 µL, 0.01 M), HCl (800 µL, 1 M), and AA (320 µL, 0.1 M) into an aqueous CTAB solution (40 mL, 0.1 M). The seed solution (50 µL) was then added into the growth solution, followed by inversion mixing for 5 s. The resultant solution was kept undisturbed at 35℃ for 6 h.

Purification of the Au Nanobipyramids: The as-prepared Au NBP solution (40 mL, longitudinal plasmon wavelength: 950 nm, extinction value at the longitudinal plasmon peak: 4) was centrifuged at 5500 rpm for 10 min and redispersed in a CTAC solution (30 mL, 0.08 M). AgNO (8 mL, 0.01 M) and AA (4 mL, 0.1 M) were subsequently added into the CTAC-stabilized Au NBP solution under gentle shaking. The resultant solution was kept at 60°C for 6 h, during which Ag was overgrown on the Au nanocrystals to produce bimetallic Au/Ag products. The Au/Ag products were then centrifuged at 5000 rpm for 10 min and redispersed in CTAB (30 mL, 0.05 M). The solution was left undisturbed at 35℃ overnight, during which the Au/Ag heteronanorods agglomerated and precipitated to the bottom of the container, while the polyhedral Au/Ag nanoparticles remained in the

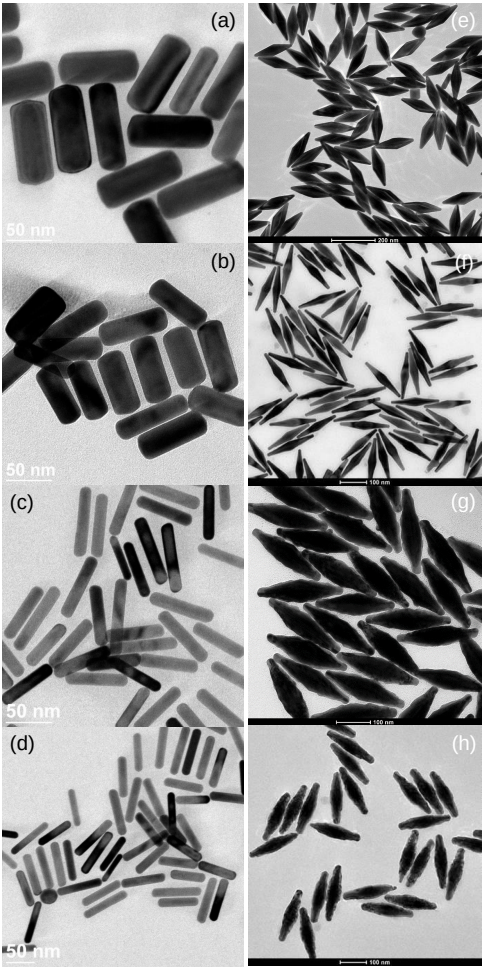

Figure 3.3. Representative transmission electron microscope images of gold nanorods (a-d), gold nanobipyramids (e,f) and gold nanobipyramid@palladium bimetallic nanostructures.

supernatant. The Au/Ag heteronanorods were redispersed in DI water (20 mL) and subsequently mixed with $NH{\cdot}H_2O$ (400 µL, 30 wt%) and H_2O_2 (300 µL, 0.1 M) and kept for 4 h. During this process, the Ag segments were gradually etched away. The clear supernatant was carefully taken out. The resultant pure Au NBPs were separated by centrifugation (5500 rpm, 10 min) and redispersed in DI water for further use.

Preparation of the Au NBP@Pd Bimetallic Nanostructures: The starting Au NBPs were grown according to a reported procedure as demonstrated above.[121] The Au NBP@Pd nanostructures were prepared according to a previous report with slight modification.[121] Specifically, the Au NBP solution (20 mL, longitudinal plasmon wavelength: 950 nm, extinction value at the longitudinal plasmon peak: 3) was centrifuged at 5500 rpm for 10 min and redispersed into CTAB solution (0.03 M) at the same volume. H_2PdCl_4 (30 µL, 0.01 M) and L-ascorbic acid (15 µL, 0.1 M) were subsequently added into the Au NBP solution under gentle shaking. The resultant solution was kept undisturbed at 35℃ overnight. The resultant Au NBP@Pd nanostructures were separated by centrifugation (5000 rpm, 10 min) and redispersed in deionized water for further use. Figure 3.4 presents the electron microscope images of the Au NBP@Pd Bimetallic Nanostructures on the substrate.

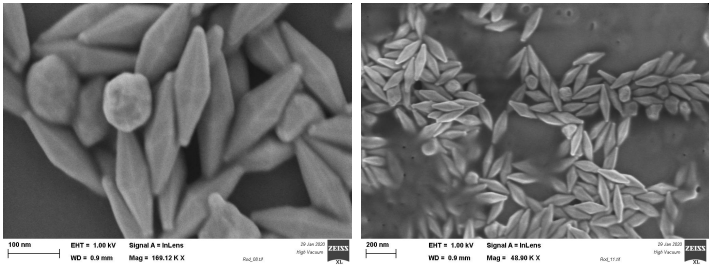

Figure 3.4. Scanning electron microscope images of gold nanobipyramid@palladium bimetallic nanostrucures.

3.3 PREPARATION OF HYBRID PLASMON-FIBER CAVITIES

So far, the preparation of the microfiber and gold nanoparticles as two components of the hybrid cavities has been introduced in Section 3.1 and 3.2. Now we can continue to prepare the hybrid cavities. Figure 3.6 and 3.7 presents the scanning electron microscope images of hybrid plasmon-fiber cavities with different situations. Figure 3.5 demonstrates the basic preparation procedure:

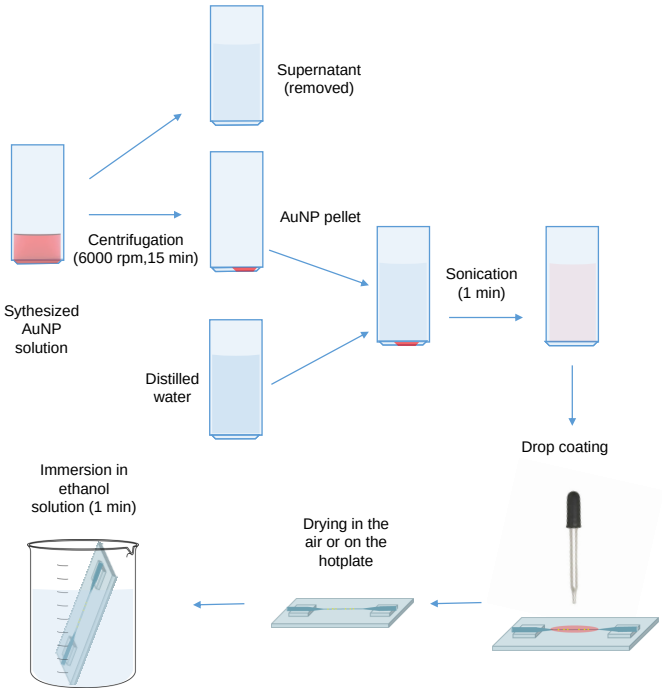

FIGURE 3.5. Preparation procedure of plasmon-fiber cavities.

- If the synthesized AuNPs solution is found with a lot of crystal-like particles after a long time storing, putting the bottle of solution into a water bath and keep the temperature at 40°C until the crystals disappear.
- Centrifuging 100 µL synthesized AuNPs solution at a speed of 6000 rpm for 15 minutes.
- Removing the supernatant after the centrifugation in the last step carefully. In fact, the supernatant can be transferred to a vial and further centrifuged to recover some AuNPs. If it is found there are too many impurities (mostly CTAB or CTAC) left on the surface of microfibers in the later preparation procedure(this case is shown in Figure 3.7(c) and (d)), a second round of centrifugation can be processed. Basically, operating the second round as the first one is enough to get the pure particles.
- Dispersing the centrifuged AuNP pellets into 500 µL distilled water and shaking in a ultrasonic cleaner for 1 min.

  The volume of synthesized AuNPs solution and the distilled water used to dilute the centrifuged AuNP pellets can be adjusted according to the specific piece of synthesized AuNPs solution (gold nanorods, gold nanobipyramids or gold bipyramids@palladium nanoparticles). If the sample is diluted too much, it will be quite difficult to find a proper hybrid cavity. On the other hand, if they are not diluted enough, too many particles gathering or staying too closed to each other is also dissatisfactory for the measurements. (see Figure 3.6(a) and (b) and 3.7(c-e))
- Drop coating onto the surface of microfibers prepared from the Section refsec:Microfiber tapering. Drying in air or on a hot plate.
- Immersing the dried microfiber into the ethanol solution for 1 minute to remove extra CTAB or CTAC.

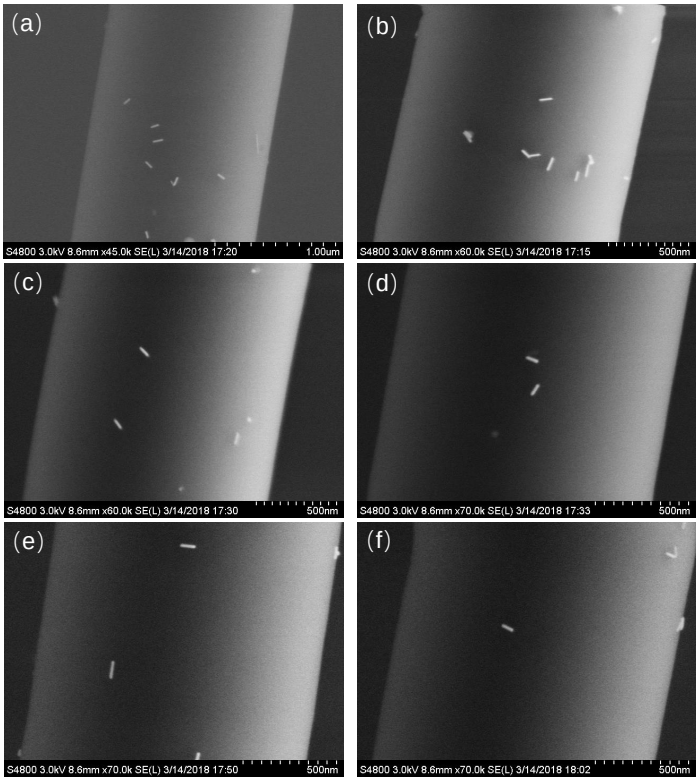

Figure 3.6. Representative scanning electron microscope images of fiber-coupled gold nanorods.

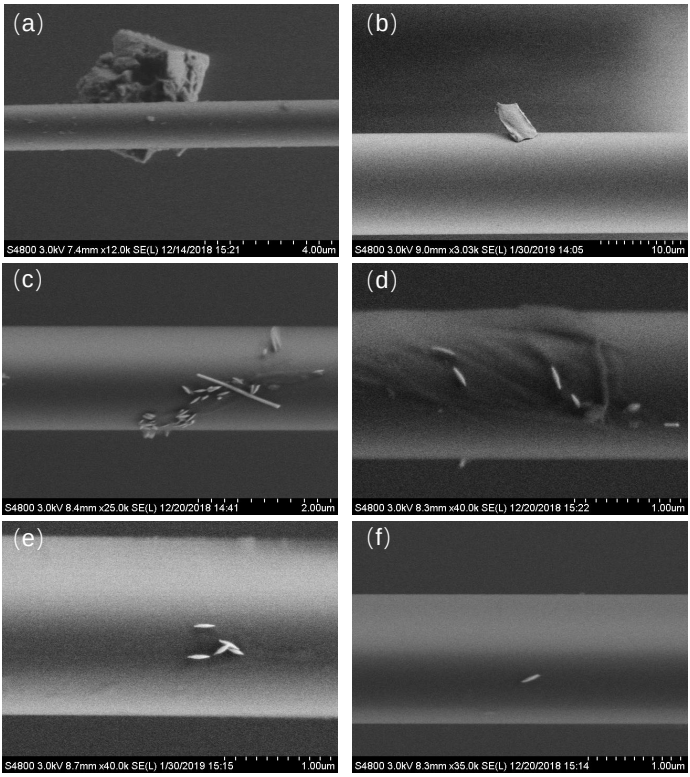

Figure 3.7. Representative scanning electron microscope images of fiber-coupled Au NBP@Pd nanostructures.

3.4 MICROSPECTROSCOPY

If we retrospect on the long history of studying single metal particles in physical science, it can date back to the turn of the last century when Zsigmondy and coworkers developed the dark-field immersion microscope.[122] This microscope made it possible to estimate the size of single metal particles by observing and even counting them in a liquid. Besides this, it also can be used to study the kinetics of the coagulation of particles, the structure of various of heterogeneous systems. Those abilities make dark-field microscopy widely used in materials and biological sciences. This technique has been rediscovered and developed in the past decade to study single metal particles. By combining an imaging monochromator and a charge-coupled devive (CCD) camera with a dark-field microscope, the Rayleigh scattering spectra from single metal particles are readily measured.[123] The Schultz and Feldmann groups firstly reported the spectroscopy of single metal particles.[123–125] They succeed to determine how the frequency of the localized surface plasmon resonance depends on silver particles' shape and size.

Afterwards, microspectroscopy which is the combination of microscopic with spectroscopic measurement methods became an essential technique to study single metallic particles. There are various components from light source to detectors for performing microspectroscopic measurement. The proper components should be picked for the certain systems and the different research aims.

Basically, the microscope includes the microscope objective, the eyepiece, illumination sources, and a host of other components. The microscope objective is complexly composed by a set of lenses and used to generate an image of a tiny area of a sample in the front of the objective. Three factors of their characteristics need be considered regarding to the investigated system in an experiment: *the magnification*, *the numerical aperture (NA)*, and *the working distance*. The *magnification* defines how large a spatial feature occurs in the image plane. The *numerical aperture* is a measure of its ability to

gather light and resolve fine specimen detail at a fixed object distance, hence decide the resolution of imaging. The *working distance* is fixed by the objective and is mainly decided by the NA and the size of the objective front lens. In general, there is no direct influence on the performance of the objective based on the working distance. However, it limits the available space between the sample and the objective and indeed should be considered in the experiment.

Illumination within a microscope is as important as selecting the proper objectives. It is crucial to choose the correct illumination to get a conclusive results regarding different objects of study. There are wide variety of light sources and illumination paths available. Most basically, one can distinct them as *reflected* and *transmitted* light depending also on whether it is reflected from or passes through the sample. Now, both can be used simultaneously. In this case, the microscope is divided into two types: *upright* and *inverted* microscope depending on the geometry of the microscope itself. Furthermore, regarding the microspectroscopy, there is another important distinction namely *dark-field* and *bright-field*. There is a big difference in regards to the collection of light. In the *dark-field* illumination, only *scattered* light is collected, in contrast to both *transmitted* and *reflected* light being collected in the *bright-field* illumination. Particles on the substrate appear as bright, diffraction-limited spots on a dark background. Hence, the dark-field is the good option to observe the isolated metal particles.

So far, the basic illumination methods used in microscopes is briefly introduced. However, we use a specific side-illumination instead of the traditional one. It is mainly decided by the optical properties of our studied systems. A side-illumination, which is always along the direction of the long axis of microfibers, is utilized to avoid overly strong scattering light from the fiber itself (see Figure 3.8). A similar side-illuminated microscopy is also introduced in other studies.[126] Figure 3.8 shows the setup used in the measurements of the fiber-coupled gold nanorods. For the linear measurement, an incoherent white-light source (Energetiq Laser-Driven Light Source EQ-99) is collimated to the sample with an incident angle of around 30 degrees.

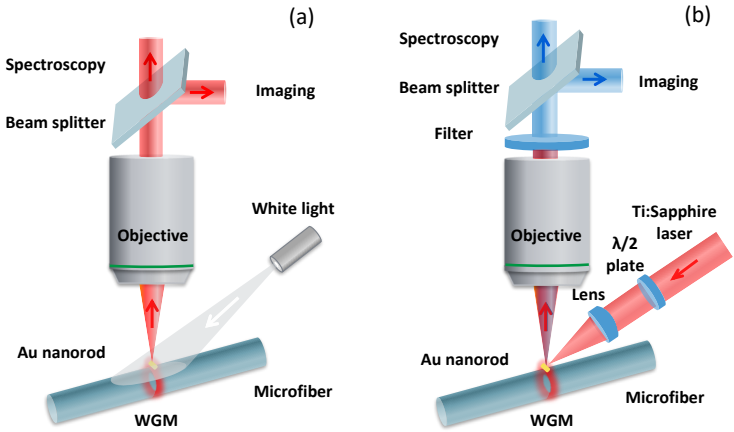

Figure 3.8. Schematic dark-field setup for white light scattering (a) and nonlinear spectroscopy(b) with separate illumination path.

To excite the nonlinear response of the hybrid systems, a mode-lock Ti:sapphire laser which allows wavelength tuning in the range of 780 – 855 nm is employed. Its pulse duration is 100 fs at 80 MHz repetition rate. A half wave plate is used to ensure the illumination light is s-polarized, which is parallel to the lab table. An achromatic lens of 75 mm focal length is added before the sample to focus laser beam onto the sample.

In later measurements of the fiber-coupled gold NBPs, an improved illumination system is developed to control the white light and laser source (see Figure 3.9. In this illumination system, dismounting and re-fixing the different excitation source is unnecessary. By a flipped mirror shown as the dashed outline in the set-up figure, the illumination can be easily switched from white light source to the laser source. Meanwhile, the incident angle and focus condition stay the same during the switching process. Two threaded iris are added in the excitation path to keep the same size of the focus spot between the white light and laser source. A neutral density filter is used to implement the excitation laser power dependent measurement.

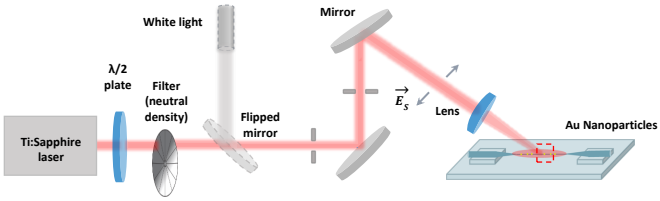

Figure 3.9. Schematic dark-field setup for white light scattering and nonlinear spectroscopy with improved illumination system in which the white light source and excitation laser source can be switched easily when keeping the same incident case. The schematic diagram of the coupling system between isolated Au nanoparticles and optical microfibers are shown in the red dashed frame. The incident light is s-polarized.

The other part of the microspectroscopy setup is a grating spectrometer. The performance and spectral resolution concerned most are influenced by a number of parameters, including the width of the entrance slit in microscope image plane, the grating parameters, the size and the pixel columns numbers of the 2D detector, and so on. In our microspectroscopy setup, a grating monochrometer (Princeton Instruments IsoPlane 160, 300 lines/mm, 300 nm blaze) and 2D Peltier-cooled CCD detector (Princeton Instruments PIXIS 256) combined with an upright microscope (Nikon LV100) are used as shown in Figure 3.10. A short-pass filter (FGB37, Thorlabs) is inserted before detectors to filter out the intensely scattered laser. A Nikon TU plan ELWD 50x, NA 0.6 and a Nikon TU Plan Fluor ELWD 60x, NA 0.7 objective are respectively utilized to collect scattered and emitted light under side-illumination in specific experiment. It will be specified in each measurement. A photograph of the our microspectroscopy setup is shown in Figure 3.10.

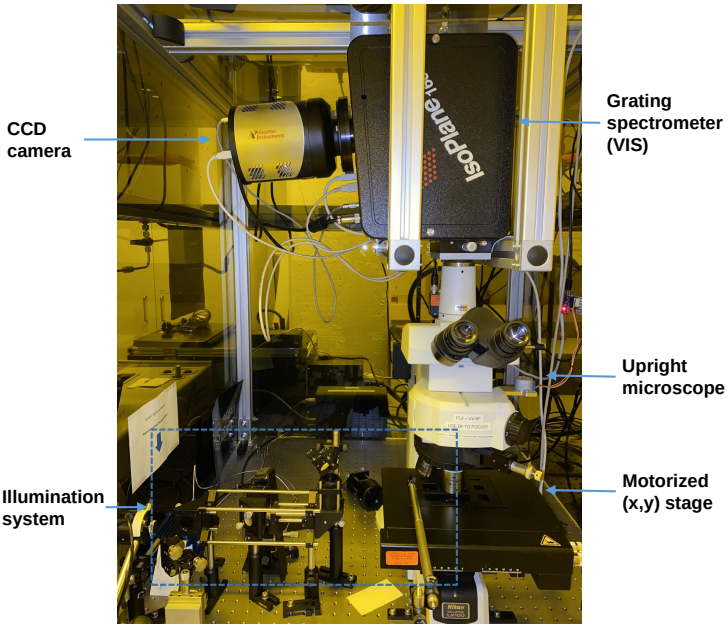

Figure 3.10. Photograph of the microspectroscopy setup based on a Nikon Eclipse LV100 upright microscope and a Princeton Instruments IsoPlane-160 monochromator used.

4

PLASMON-FIBER HYBRID CAVITIES

As mentioned in chapter 2, the metallic nanoparticles can confine light into the subwavelength benefitting from the *localized surface plasmon resonance*. However, their plasmon life is generally short and the resonance line-width is broad due to large damping losses. The full width at half-maximum (FWHM) is typically hundreds nanometers resulting in a very low quality factor. While the microcavities have a big advantage in the tunable and high quality factor. In this chapter, a new coupled system between plasmonic particles and fiber microcavities is described. We investigate both the linear and nonlinear optical properties of those hybrid cavities, including the second-harmonic response and multiphoton photoluminenscence.

This chapter are mostly based on the following publications:
Q. Ai, L. Gui, D. Paone, B. Metzger, M. Mayer, K. Weber, A.Fery, H. Giessen,
"**Ultranarrow Second-Harmonic Resonances in Hybrid Plasmon-Fiber Cavities**",
Nano Letters **18**(9), 5576-5582 (2018),
DOI 10.1021/acs.nanolett.8b02005.

Q. Ai, H. Zhang, J. Wang, and H. Giessen,
"**Multiphoton Photoluminescence in Hybrid Plasmon-Fiber Cavities with Au and Au@Pd Nanobipyramids: Two-Photon versus Four-Photon processes and rapid quenching**",
ACS Photonics **8**(7), 2088–2094 (2021),
DOI 10.1021/acsphotonics.1c00470.

4.1 INTRODUCTION

Experiments with femtosecond lasers and resonant plasmonic systems yielded efficient nonlinear effects such as second- and third-harmonic generation (SHG and THG),[127–131] four-wave mixing,[132, 133] ultrafast optical switching,[134] and multiphoton photoluminescence (MPPL)[135–139] from very small volumes beyond the diffraction limit, opening the door for nonlinear photonic devices on the nanometer scale.

Until now, the power of the generated nonlinear light in nanostructures is still very weak. Several approaches have been applied in order to promote the conversion efficiency. One prominent way is to combine other highly nonlinear materials such as semiconductors,[140, 141] polymers,[142, 143] dielectrics,[144] etc., in which the plasmonic structures are usually resonant at the excitation wavelength. Another method is using multiresonance designs. It will be introduced more detailed in Chapter 5. The nonlinear conversion efficiency can be boosted further. However, near-field enhancement using the former two methods is still limited, mainly due to large damping losses from the metallic particles.

On the theory side, an anharmonic oscillator model has been successfully exploited to provide instructive connections between linear and nonlinear properties of a plasmonic system,[44, 128, 130] in which the linewidth $\Delta\omega$ of the linear resonance plays a key role in nonlinear yield. Intuitively, a narrow linewidth, which indicates a higher quality factor Q of the resonance, allows for light-matter interaction over a longer time period, and also implies insignificant damping channels which bring benefit to strong near-field enhancement. The anharmonic oscillator model is able to predict a nonlinear signal that is superlinearly proportional to the inverse of the resonance linewidth[44, 46] (e.g, for SHG, the nonlinear efficiency scales to $1/\Delta\omega^4$ if the plasmon resonance matches the fundamental frequency), which paves exciting avenues for highly efficient nonlinear optical processes at the nanoscale.

So far, different approaches have been used to decrease the linewidth of plasmonic resonances. One way is to tailor the aspect ratio towards very elongated rods.[125, 145, 146] Another way is to choose high-quality single-crystalline materials, which reduces damping by scattering at grain boundaries.[147] Still, the typical linewidths of single plasmonic rod antennas are around 50 nm.

Coupled systems with dark modes in plasmonic dimers,[148, 149] trimers,[150] or oligomers[141, 151] are capable to exhibit very sharp and narrow linewidths due to the inhibited radiative losses. In contrast to electromagnetically-induced-transparency (EIT)-type coupling,[152] in which through destructive interference the transmission is enhanced and therefore weak light-matter interaction occurs, electromagnetically-induced-absorption (EIA)- type coupling enables enhanced absorption of light by constructive interference of the coupled resonances in the materials. Previous attempts[153, 154] achieved linewidths as small as several nanometers, and indeed succeeded in enhanced light-matter interaction for example in magneto-plasmonics.[155]

Meanwhile, nonlinear photoluminescence, especially two-photon photoluminescence [156–158] of noble metallic nanostructures is also attracting increasing attention because of existent and potential applications in the areas of theranostic biomarkers,[159] bioimaging,[137] and so on. Multiphoton-induced luminescence from noble metals and its enhancement on roughened surfaces have first been reported in the pioneering experiments of Boyd in 1986.[160] Thereafter, gold nanoparticles became one of the most promising photostable and non-blinking single optical biomarkers due to their large extinction cross sections, while the two-photon absorbing process provides the possibility for local heating.[161, 162] However, when compared to the investigations about coherent nonlinear processes, such as second- and third-harmonic generation, research about MPPL from isolated gold nanoantennas is still quite rare, and some more analysis is necessary to fully understand and utilize this process. It is

mainly limited by its low quantum efficiency. Particularly, higher-order photoluminescence requires even larger peak intensities and local fields.

On the other hand, photoluminescence quite often overlaps with the coherent optical response of the nanoantenna systems in nonlinear spectra, for example in second- or third-harmonic generation processes.[161, 163, 164] In this case, controlling and modifying the PL process is required for applications. A comprehensive knowledge of the MPPL characteristics and full understanding of the mechanisms are the preconditions of the desired precise control. It is already well known that 2PPL can be enhanced by a strong local field.[165–167] Our research will offer strong support for this conclusion. Three-photon absorption from single gold nanoantennas has been reported.[168] 4PPL has been observed from resonant gold dipole antennas.[169] The dynamics of MPPL has been investigated in gold nanostructures.[136, 170] The two- and multi-photon photoluminescence in gold nanoparticles with different shapes and sizes have also been described in numerous publications.[171–174] However, there is still no clear idea on how to modify them in a controlled manner. In addition, knowledge of the spectral and polarization characteristics of MPPL is essential for the control of plasmonic properties.

4.2 LINEAR OPTICAL PROPERTIES

The localized surface plasmons of the bare plasmonic nanoparticles on the silica substrate and the linear optical properties of the hybrid resonances are firstly investigated. In this section, we will focus on unraveling how the parameters in both systems (bare gold nano particles and fiber-plasmon hybrid cavities) decide the resonance linear properties such as resonant positions and linewidth of the scattering spectra. Regarding to the clear studying and understanding of LSPR in the metal nanopartilces,[10, 110, 175–179] we will just briefly present two batches of gold nanorods with different aspect

ratio. Besides that, we will introduce a particular geometry nanoparticles, namely nanobipyramids. The larger blue-shift of the resonant wavelength is discovered by growing thicker palladium shell onto the gold nanobipyramids. All those particles will be used to study the nonlinear optical response in the plamson-fiber hybrid cavities. Meanwhile, the influence of the incident angle of the excitation light is also discussed. At last, the enhancement effect and prolonging life time from the coupling with the microfiber cavity are presented by comparing the scattering spectra between gold nanorods on the substrate and the fiber-coupled gold nanorods.

4.2.1 *Plasmon resonance of gold nanoparticles*

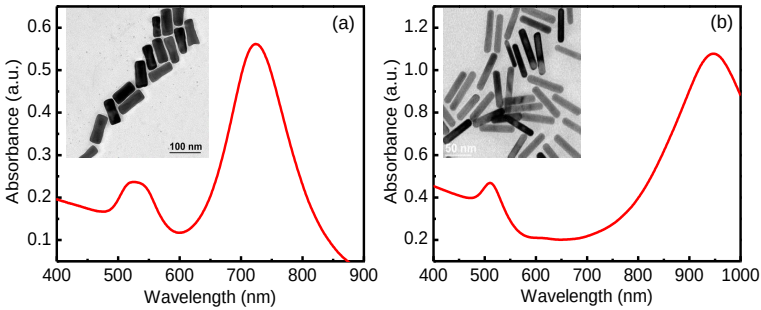

Figure 4.1. The schematic absorbance spectra of a solution of gold nanorods with an aspect radio about 3 (a) and 5 (b). Corresponding TEM images are shown in the inset figures.

The plasmon resonance of gold nano particles, especially gold nanorods has been investigated a lot and it is well known that the longitudinal localized surface plasmon resonance red shifts as the aspect ratio increases. Figure 4.1 demonstrates this characteristic. After those gold nanoparticles are coated onto a silica substrate, the resonance blue shifts as shown in Figure 4.8(a) which shows the

scattering spectrum of one gold nanorod from the solution measured in Figure 4.1(b). This shift is caused by the change of surrounding dielectric material.

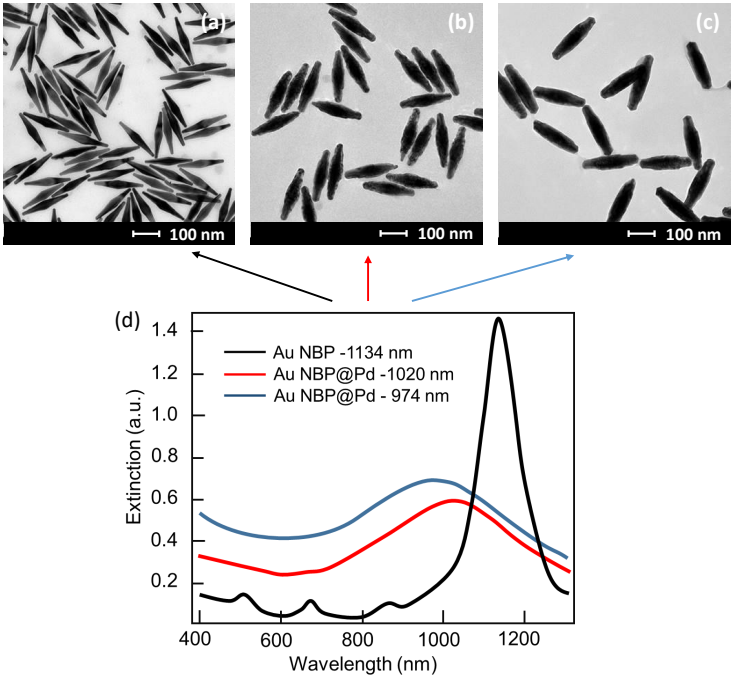

Figure 4.2. (a) SEM image of gold nano bipyramids particles. (b,c) SEM images of the gold nanobipyramid core@Pd shell bimetallic nanostructures. (d) Their corresponding extinction spectra.

Figure 4.2 shows another structure investigated in this thesis, namely bipyramid nanoparticles. Those geometries are supposed to obtain more efficient coupling with microfibers considering the sharp tips. The gold nanobipyramid core@Pd hell bimetallic nanostructures

depicted in Figure 4.2(b) and 4.2(c) are utilized to investigate and realize the quenching effect of MPPL.

4.2.2 *Coupled resonance of plasmon-fiber cavities*

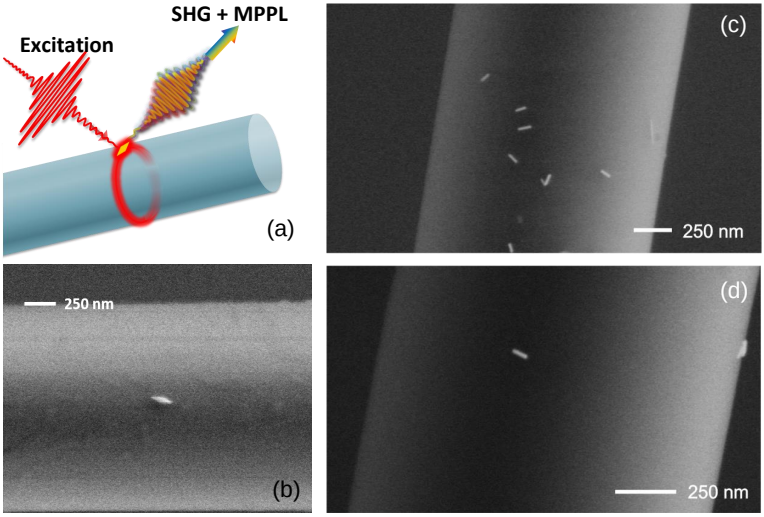

Figure 4.3. (a) The schematic diagram of the plasmon-fiber cavities. (b) SEM image of the coupling system between an isolated gold nanobipyramid particle and an optical microfiber. (c,d) SEM images of the coupling systems between gold nanorods and microfibers

The basic idea of the plasmon-fiber cavities is using gold nanoparticles as an optical antenna to intercept and concentrate the incident electromagnetic energy by localized plasmon resonance and then utilizing the fiber as a microcavity to confine the light inside and enhance the interaction between the light and nanoparticles by whispering gallery modes. The schematic diagram of the coupling system between an gold nanorods and an opticla microfiber is shown in

Figure 4.3(a). Other coupling systems used to investigate the multi-photon photoluminescence and enhanced second harmonic generation in the next chapter are similar. The gold nanorods are simply replaced by gold nano bipyramids. Figure 4.3(b-d) show scanning electron microscopy images of these coupling particles.

In the coupling systems, several main factors including the size of gold nano particles, the diameter of the microfibers, the orientation and position of the particles on the surface of the fibers influence the coupling strength, thus induce the resonances with different Q factors. Regarding the drop-coating method used to achieve the coupling cavities, we are not able to control the orientation and position of the particles on the surface of fibers. While, the diameters of fibers and the sizes of gold nanoparticles can be designed and controlled. In the later linear scattering spectroscopy, the setup in Figure3.8 (a) in Chapter 3 is utilized.

Figure 4.4 illustrates the scattering spectra of coupled systems in which the nanoparticles are from the same gold nanorods solution, while the diameters of microfibers varying from 10 μm to 1.5 μm. As the diameter decreases, the coupling strength between plasmon modes of gold nanorods and the WGMs of microfibers increases. Those peaks in the scattering spectra are coupled resonant modes. Their wavelength position is different from the WGMs of the microfiber, however, their mode number still can be determined by Airy theory introduced in Chapter 2. For example, the mode in the Figure 4.4(c) can be considered as TM7 as it closed to the position of this mode in the Airy calculated result. Then one can determine the number 7 mode is efficiently coupled to the fiber with a diameter around 1.5 μm.

On the other hand, the wavelength range of the coupled resonance is also determined by the plasmon modes of gold nano particles. Hence, efficient coupling between plasmon modes and WGMs which supports a high Q factor at a certain wavelength can be obtained by tailoring the diameter of microfibers and aspect ratio of gold nanorods. In other words, the resonant wavelength of the hybrid systems is tunable by adjusting the size parameters. Figure 4.5 illustrates

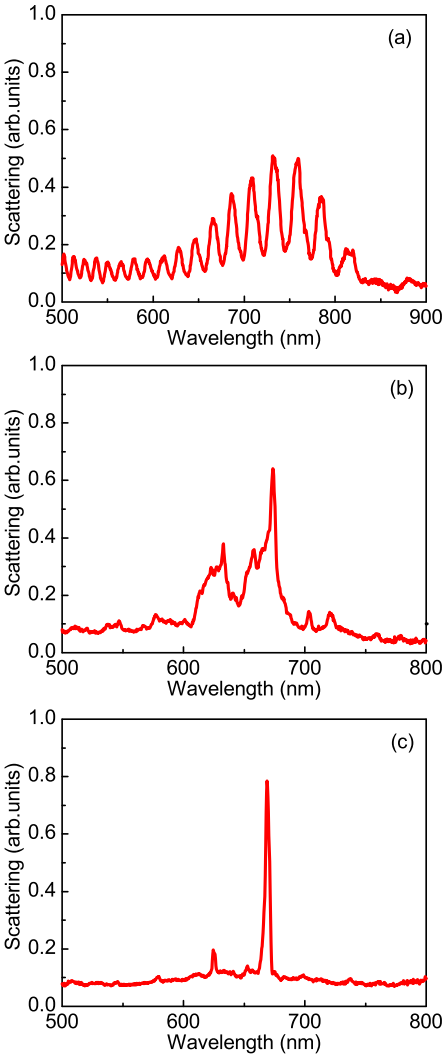

Figure 4.4. Scattering spectra of coupled system with different microfiber diamters, The diameters are 10 μm in (a), 5 μm in (b) and 1.5 μm in (c), respectively.

some typical single-band narrow scattering spectra with different resonance positions in the range of 700 nm to 900 nm. The plasmon mode of gold nanorods in aqueous solution exhibits resonances ranging from 873 nm to 1138 nm. It shifts to shorter wavelengths when deposited onto glass substrates or fibers, leaving the upper half exposed to air. The diameters of different tapered fibers are varied from 1.5 μm to 1.9 μm.

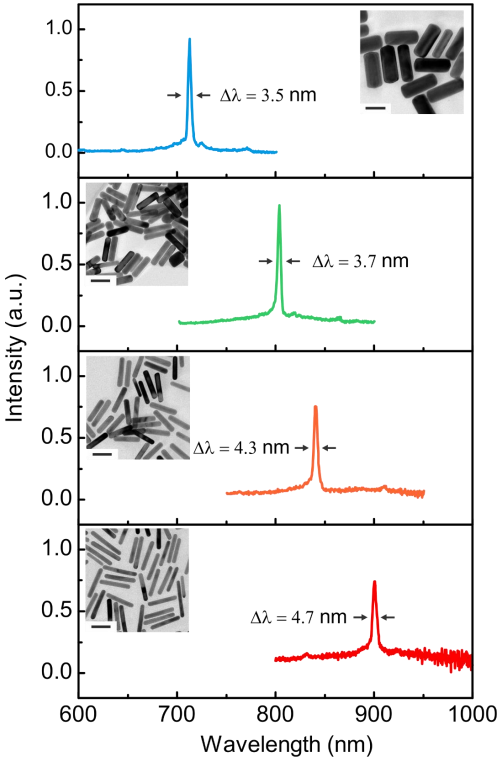

Figure 4.5. Scattering spectra of coupled systems with different gold nanorod aspect ratios and microfiber diameters. The insets show representative transmission electron microscope images of gold nanorods. Scale bar: 50 nm.

Based on the prediction of modes and Airy theory, the typical coupling systems are designed with a certain size of gold nanoparticles and microfibers for each experiment, based on the different research purposes and experimental conditions. The specific parameters will be illustrated in any necessary case.

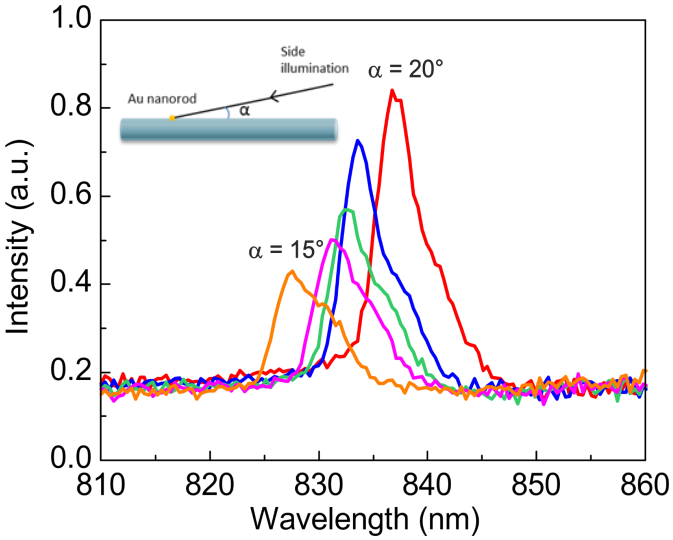

Figure 4.6. Linear scattering spectra from a gold nanorod on the surface of a microfiber at different incident angles as illustrated by the inset.

The resonance positions of localized surface plasmon modes in metallic nanoparticle systems are usually sensitive to excitation schemes, which is probably due to phase retardation. It holds true also in our coupled systems. Our experimental results suggest that varying the incident angle causes different resonance wavelengths, linewidths, and scattering intensities. As Figure 4.6 indicates, tuning the incident angle α from 15^o to 20^o results in red-shifting and narrowing of the resonance for one hybrid cavity. For different gold

nanorods on the fiber surface, we also find that the optimum incident angle which leads to the narrowest resonance linewidth and the highest scattering intensity is slightly different. This difference might be attributed to the varying conditions of the coupled systems, especially the orientation of the gold nanorods deposited on the tapered fibers.

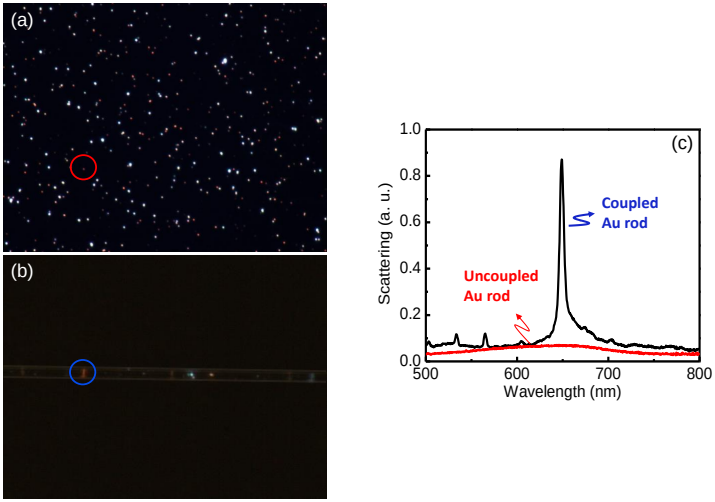

Figure 4.7. Imaging of the scattering light from gold nanorods on the substrate (a) and fiber-coupld ones (b) recorded by camera. (c) Linear scattering spectra from gold nanorods on the substrate and the surface of a microfiber under the same incident condition.

Figure 4.5 already present us the efficient coupling systems between gold nanorods with the different aspect ratio and the microfibers with the different diameter. It is nicely seen that the linewidth of their scattering spectra are all quite narrow, thus corresponds to a high quality factor. It is naturally supposed to possess the higher peak intensity of scattering. Figure 4.7 gives direct and

strong basic proof. The spectra of the gold nanorods on the substrate and the surface of microfibers are taken under totally same incident condition. Compared to the gold nanorod on the substrate where no coupling effect occurs, the one on the microfiber with a diameter around 1.55 μm is several tens times enchant in terms of the scattering peak intensity. It proves that our explanation about the enhanced interaction between light and material in the coupling system is correct and logical.

4.3 SECOND HARMONIC GENERATION

In the anharmonic model introduced in Section 2.3 of Chapter 2, we have already obtained the conclusion that the nonlinear effect scales with a higher power of the local near-field enhancement. Especially, the SH intensity is predicted to be proportional to the $4th$ power of the quality factor. Thus, the strong SHG response can be expected due to the narrow linewidth and big intensity of the hybrid mode in the plasmon-fiber cavity. In this section, we will mainly study the properties of second harmonic responses in the hybrid systems by implementing the wavelength-dependent nonlinear spectroscopy and modeling the corresponding SH resonances with the hybrid anharmonic oscillation model.

4.3.1 *Enhanced second harmonic generation*

In the Section 4.1, we have come to the conclusion that the small linewidth of the linear scattering resonance should induce a narrow SH resonance. Moreover, the high-Q system can bring us high nonlinear efficiencies. In order to verify it, we carry out a series of measurement as described in next paragraphs. As a result, an ultranarrow SH resonance with high intensity is achieved in the plasmon-fiber cavities.

To demonstrate the extreme narrowing of the linewidth benefited from the efficient coupling between plasmon and whispering gallery

modes, we compare the linear and nonlinear results from a single gold nanorod coupled to a silica tapered fiber with another uncoupled rod on a silica substrate. To ensure exactly the same experimental conditions (such as focus, illumination angle, etc.) for both systems, we drop coat part of the gold nanorods solution right next to the microfiber onto the glass slide which held the fiber (diameter of about 1.80 µm).

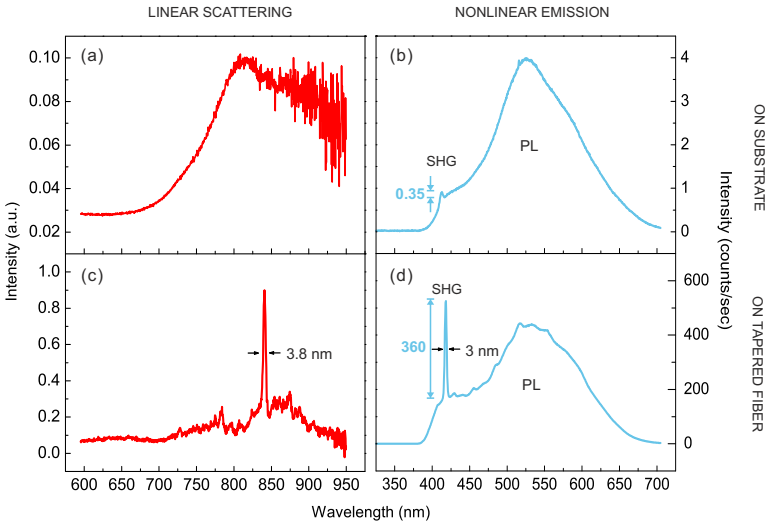

Figure 4.8. (a) Measured scattering and (b) nonlinear emission spectra of a single gold rod on a silica substrate surface. (c) Measured scattering and (d) nonlinear emission spectra of a single gold rod on a tapered fiber surface.

Figures 4.8(a) and 4.8(c) depict the linear scattering spectra of the uncoupled and coupled systems respectively. In stark contrast to the bare gold nanorod situation where scattering exhibits a FWHM of the spectrum on the order of 100 nm, the plasmon-fiber coupled configuration leads to a dramatic narrowing of the linewidth to

3.8 nm around 840 nm wavelength and simultaneously offers more than 10-fold enhancement in the peak scattering intensity.

For the nonlinear characterization, the setup in Figure 3.8(b) in Chapter 3 is utilized. The excitation laser wavelength is chosen to coincide with the spectral position where peak scattering occurs. Due to the unknown orientation of the individual gold nanorod, a half wave-plate is used to adjust the state of polarization of the illumination light.

By rotating the half waveplate and recording the nonlinear yield, we find the optimum irradiation condition for exciting the plasmon mode which led to maximum nonlinear light generation (see Figure 4.8(b)). The nonlinear spectrum of the isolated gold nanorod features a very weak SHG peak at about 420 nm together with a more pronounced and broader multiphoton photoluminescence background ranging from 400 nm beyond 700 nm. The SHG peak intensity on the top of the MPPL background is 0.35 counts per second, assuming incoherent superposition of SHG and MPPL spectra. In comparison, the coupled system yields much stronger nonlinear emission at the same excitation power (see Figure 4.8(d)).

The sharp SHG peak possesses a FWHM width of about 3 nm and yields an SHG intensity of 360 counts per second, three orders of magnitude stronger than that from the isolated gold nanorod alone in Figure 4.8(b). In addition, the plasmon-fiber coupling contributes to two orders of magnitude enhancement of the MPPL yield as well. It is interesting to see that the broad MPPL spectrum is regularly modulated by several whispering gallery modes located in the corresponding spectral window, which causes slight fringes while absent in the isolated gold nanorod situation. In both systems, the peaks of the MPPL spectra which are located at around 520 nm are dominated mainly by the band structure of gold. The entire profile of MPPL is determined by the single-crystalline gold nanoparticle[138] and our experimental setup, for instance, the short-pass filter before our detector. According to the similar nonlinear emission profiles from both uncoupled and coupled systems, we believe that it is gold which acts as our efficient nonlinear source for frequency up-conversion. Also,

it is worth noting that the 1000-fold enhancement of SHG scattering is a moderate value, since some uncoupled gold nanorods produced nearly undetectable SHG signals.

4.3.2 *Second harmonic spectroscopy and modelling*

In order to study the wavelength dependent SHG efficiency and characterize the second-harmonic resonances, we tune the center wavelength of our excitation laser over the linear resonances step by step. In the case of the linear resonance at 832 nm as shown in Figure 4.9(a), the excitation laser source is tuned from 812 nm to 850 nm. In the linear scattering wavelength range, the scattered laser spectra are shown in Figure 4.9(b). Their responding nonlinear emission are demonstrated in Figure 4.9(c). Only some ones with relevant high intensity are plotted here, while, others are absent because of weakness. For every spectrum, we analyze the SHG peak intensity and then plotting it as a function of excitation wavelength. In such a way, an ultranarrow second-harmonic resonances of a coupled system is achieved. More parameter details will be given again in the next paragraph (the system shown in Figure 4.9 is the same with the Figure 4.10(a) and (b)). Here, it is more emphasized to show the experiment order and therefore to explain how to get the SH resonances, which is essential for the later experiment.

For better comparison, we choose two hybrid cavities which exhibit different linewidths as well as distinct resonance wavelengths. Figures 4.10(a) and 4.10(c) show the linear scattering spectra (red curves, normalized to [0, 1]) from two gold nanorods coated onto the surface of tapered fibers with diameters around 1.78 µm and 1.80 µm, respectively. The FWHM $\Delta\lambda$ of the single-band scattering is equal to 3.3 nm and 4.3 nm, which corresponds to a high Q factor $lambd/\Delta\lambda$ of 250 and 190, respectively. The resonances λ are located at 832.3 nm and 829.2 nm. Here, more efficient coupling between plasmon and WGMs causes a higher signal-to-noise ratio, and hence several tiny peaks arising from other WGMs are easily visible in the background, as opposed to Figure 4.8(c).

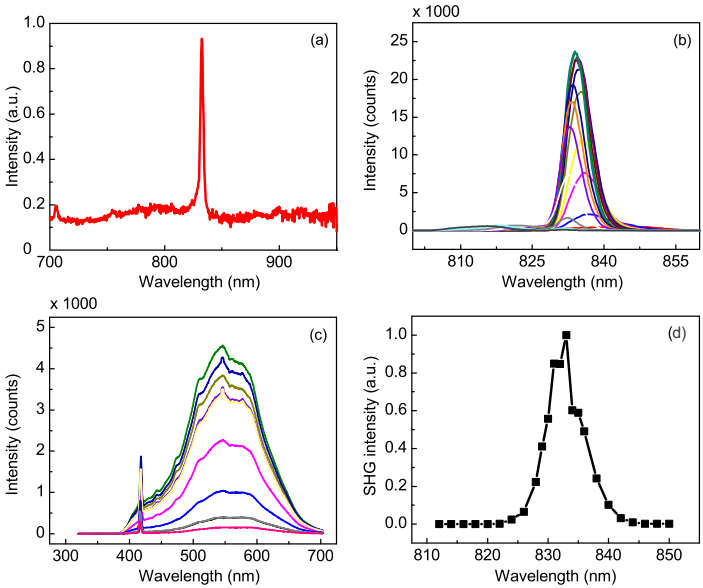

Figure 4.9. (a) Measured scattering, (b) laser scattered spectra, (c) nolinear emission spectra and (d) SH resonance of a single gold nanorod on the surface of a tapered fiber.

By sweeping the laser wavelength, we get a series of nonlinear emission spectra in which SHG and MPPL features are both observable (see the insets in Figures 4.10(b) and 4.10(d) for exemplary results, all normalized to the same incident power and exposure time). Similar to Figure 4.8(b), the linewidth of the SHG peak is again roughly 3 nm, although a slight dependence on the excitation wavelength is present which ranges between half the linear resonance linewidth and half the laser spectral width. The SHG peak position is also determined by the interplay between linear properties of the system and the excitation laser (see Figure 4.11).

For every spectrum, we analyze the SHG peak intensity by subtracting the MPPL baseline and then dividing it by the product of laser power squared and exposure time. After plotting it as a function

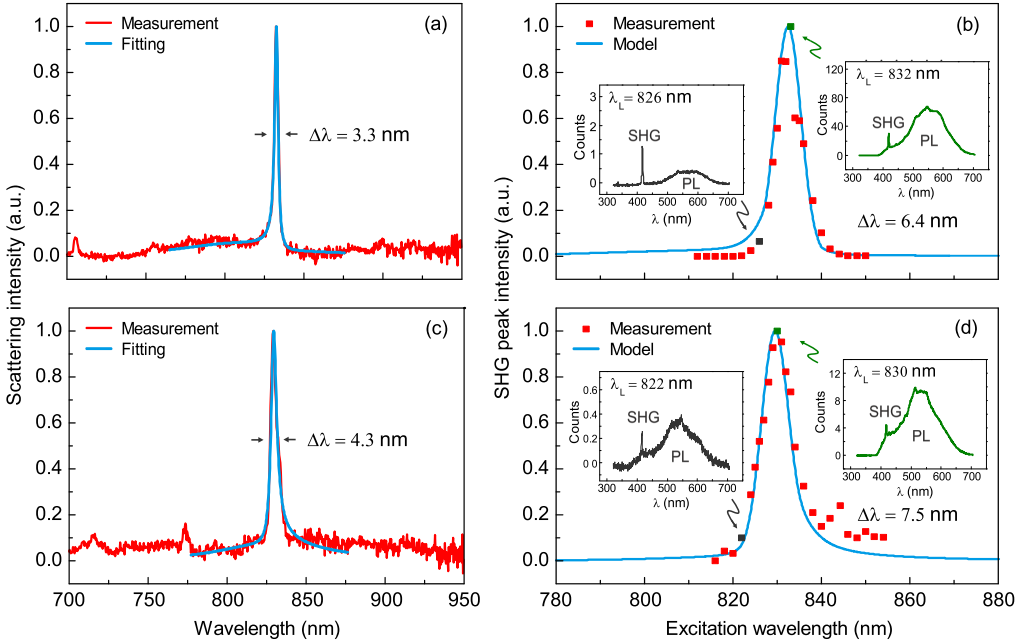

Figure 4.10. (a) and (c) show scattering spectra (red: measurement, blue: fit) from two gold rods coupled to similar microfibers with a diameter of about 1.8 µm, while (b) and (d) are their corresponding SHG efficiency as a function of excitation laser wavelength (red dots: measurement, blue curves: model). In (b,d) nonlinear emission spectra at several typical excitation wavelengths (λ_L) are shown in the insets (black and green curves). The FWHM linewidths $\Delta\lambda$ of the linear and the second-harmonic resonances are marked in (a-d).

of excitation wavelength, the nonlinear spectroscopy gives rise to ultranarrow second-harmonic resonances of the two coupled systems, as depicted by the red squares in Figures 4.10(b) and 4.10(d) (normalized again to [0, 1], for convenient comparison with our model shown later). The linewidths of the nonlinear resonances are 6.4 nm and 7.5 nm respectively if calculated at the fundamental wavelength, which lies between the value for the width of the linear resonance and our excitation laser linewidth (about 9 nm). Furthermore, it is apparent that the maximum SHG efficiency occurs almost at the wavelength of the linear resonance.

In order to analyze the relationship between the linear and nonlinear optical responses from these hybrid cavities, we employ a coupled anharmonic oscillator model in which the plasmon mode (P subscript) and the WGM (W subscript) are treated as two classical oscillators. The equations of motion considering a small perturbation as the origin of SHG read then

$$\ddot{x}_P + 2\gamma_P \dot{x}_P + \omega_P^2 x_P - \kappa x_W + a_P x_P^2 = -\frac{e}{m} E_{(t)}, \tag{4.1}$$

$$\ddot{x}_W + 2\gamma_W \dot{x}_W + \omega_W^2 x_W - \kappa x_P + a_W x_W^2 = 0, \tag{4.2}$$

where x_j denotes the displacement, γ_j represents the damping constant that is proportional to the linewidth of the mode, ω_j corresponds to the resonance frequency of an unperturbed oscillator, κ is the coupling constant addressing energy interchange between these two modes, and a_j describes the SHG strength ($j = P$ or W). e and m are the charge and the mass of the oscillator corresponding to the plasmon mode.

Solving the equations in the unperturbed situation by means of Fourier transform leads to scattering which is proportional to $|\frac{g_P}{1-\gamma^2 g_P g_W}|^2$, where the linear response function $g_j = \frac{1}{\omega_j^2 - \omega^2 - 2i\gamma_j\omega}$ ($j = P$ or W). By fitting our measured scattering spectra of the hybrid systems with this expression, the constant parameters γ_j, ω_j, and κ can be extracted. The blue curves

in Figures 4.10(a) and 4.10(c) depict the excellent fitting results, which reflects the good applicability of our model here. In particular, it is able to reproduce the asymmetrical profiles of the scattering spectra on the edge (see more results in Figure 4.5) which stem from Fano-like coupling between plasmon and WGMs.

Based on the ansatz $x_P(t) = x_P^{(1)}(t) + a_P x_P^{(2)}(t)$, the second correction term oscillating at the SHG frequency is described by $x_P^{(2)}(2\omega) \propto FT[x_P^{(1)}(t)]^2$ in frequency domain, where FT denotes Fourier transform. Here we neglect the linear response function g_P at the SHG frequency since it is spectrally flat and small for our gold nanorods which show no resonance at the harmonic frequency.

In addition, we assume that the nonlinear emission we observe experimentally mainly stems from the single gold nanorod, rather than from the microfiber. On the one hand, linear simulation enables the prediction of a much higher near-field in the vicinity of the gold nanorod than along the microfiber.[88] On the other hand, gold is considered a highly nonlinear material in general, while fused silica possesses vanishing second-order susceptibilities owing to inversion symmetry. Even if the microscopic symmetry is broken, for instance by placing the gold rod on the surface, the nonlinearity from fused silica should still be very weak. One indirect proof is that one observes highly efficient MPPL mainly related to the band structure of gold in all of our nonlinear emission spectra). Indeed, this assumption works quite well, as one can see from the excellent agreement between the SHG measurement and the results predicted by our nonlinear oscillator model (denoted by blue curves).

Fitting parameters in the anharmonic oscillator model for two hybrid systems in Figure 4.10 is depicted in Table 4.1. Note that in our model we use an ultrashort optical pulse with FWHM of 100 fs in accordance with the experimental laser source. This way, the second-harmonic resonances show broader linewidths than the linear counterparts, since they involve convolution effects arising from the broader spectral width of the excitation laser. Therefore, the linewidths of our SHG resonances are limited by our laser source at this moment.

Our model suggests that it is possible to achieve a nonlinear resonance as narrow as that in the linear regime as long as the excitation laser exhibits a narrower optical spectrum than the resonance itself (all considered at fundamental wavelength). The nonlinear oscillator model is also able to predict the much higher nonlinear conversion efficiency from the coupled cavity with higher Q factor in Figure 4.10(a) when compared to that with the lower Q factor in Figure 4.10(c). Indeed, as shown by the insets of Figures 4.10(b) and 4.10(d), the hybrid plasmon-fiber cavity with narrower linewidth and higher Q factor enables stronger nonlinear emission experimentally. It confirms once more the advantage of our coupling system which leads to less radiative losses.

ω_P(Hz)	γ_P(Hz)	ω_W(Hz)	γ_W(Hz)	κ (Hz^2)
2.37E+15	1.02E+14	2.25E+15	1.77E+13	(2.18E+29)$e^{i(-1.430)}$
2.27E+15	6.87E+13	2.28E+15	2.25E+13	(2.12E+29)$e^{i(-1.469)}$

Table 4.1. Fitting parameters in the anharmonic oscillator model for two hybrid systems in Figure 4.10.

In order to demonstrate the SHG efficiency dependence on the excitation wavelength, a series of scattered laser spectra, as well as the second-harmonic emission spectra (with the MPPL baseline subtracted) are presented in Figures 4.11(a) and 4.11(b). All these results are the measurement from the hybrid cavity shown in Figures 4.10(a) and 4.10(b). Its linear resonance is located at 832.3 nm. We tune the laser center wavelength from 810 nm to 850 nm with 4 nm step size. The scattered laser spectra and corresponding second harmonic emission spectra with the same incident laser are recorded simultaneously (shown in the same colours in Figures 4.11(a) and 4.11(b)). They are normalized to the same incident power and exposure time. When the excitation wavelength is far away from the linear resonance, scattered laser spectra have only one peak with

lower intensity near the excitation wavelength position (see black curve in Figure 4.11(a)). Meanwhile, no SHG signal is detectable (see black curve in Figure4.11(b)). As the excitation wavelength is tuned closer to the resonance position, another peak near the resonance appears and grows fast (see sky blue, pink, dark blue and red curves in Figure 4.11(a)).

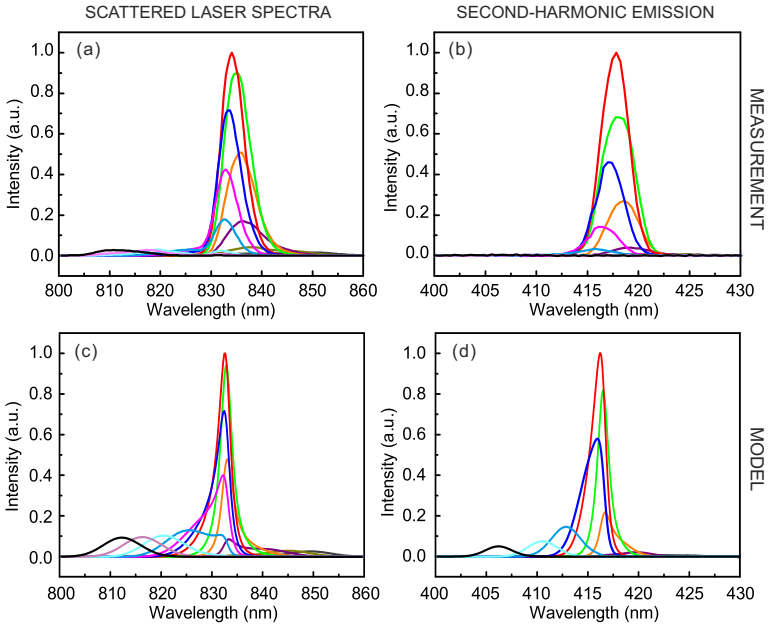

Figure 4.11. (a) and (c) are the measured scattered laser spectra, while (b) and (d) are their corresponding second harmonic emission (the spectra with the same excitation wavelength are shown in the same colour in a-d)

Accordingly, the SH emission has the same trend (see corresponding sky blue, pink, dark blue and red curves in Figure 4.11(b)). When we continue to shift the laser spectrum towards longer wavelengths, the intensity of both the scattered laser and SH spectra decreases

gradually until they vanish (see green, orange, and purple curves in Figures 4.11(a) and 4.11(b)). The wavelengths of the SH emission are nearly half of the corresponding scattered laser spectra (it is half the wavelength of the dominating peak close to the hybrid resonance when there are two peaks in the scattered laser spectra). The linewidths of those main peaks in scattered laser spectra are roughly 6 nm. The corresponding SH emission has around 3 nm linewidth, which is smaller than half the linewidth of the fundamental laser1, giving an additional hint of the ultranarrow linear resonance of our hybrid system. Figures 4.11(c) and 4.11(d) show the corresponding model results which predict similar features of the scattered laser spectra and second-harmonic emission as a function of the excitation wavelength when compared with our measurement including the overall shape and peak position.

There still is some discrepancy in terms of the linewidth mismatch. We suppose that such a disagreement is related to different illumination conditions for laser excitation and white light excitation. The linear scattering was measured by using an unfocused white light source. In Figure 4.11(a) and 4.11(b), a focused laser source was utilized, which might change the optical response of the hybrid system (highly sensitive to illumination condition as shown in Figure 4.6). Our model also employs the extracted parameters by fitting the measured linear scattering.

4.4 MULTIPHOTON PHOTOLUMINENSCENCE

When the SHG process was investigated in the hybrid plasmon-fiber cavities composed of the microfibers and gold nanorods, strong MPPL background was observed in the nonlinear response spectra. Through carrying out the spectrally resolved analysis of the nonlinear order, an efficient MPPL emission with nonlinear order up to 6 is determined. Interestingly, we find that the MPPL emission of the fiber coupled gold NBPs presents the different properties. Particularly, there are two distinguished peaks including. In order to determine and understand those PL processes, we implement the

excitation power dependent measurement and investigate the polarization characteristic of the PL emission as well. Based on the experimental results and several representative studies about the MPPL, a complete and convincing scheme of the MPPL process in those fiber-gold NBPs coupled systems is obtained. Moreover, the quenching effect of 4PPL is successfully realized by fiber-coupled gold core and palladium shell bipyramid nanostructures. This process is supposed to take place when the electron transfer from gold to palladium takes place.

4.4.1 *MPPL from the fiber-coupled gold nanorods*

When we compare the SHG peak and MPPL peak carefully in all the insets of Figures 4.10(b) and 4.10(d), it is interesting to see that the intensity ratio between them is sensitive to the excitation wavelength. It implies that the two nonlinear optical processes might originate from different nonlinear orders.

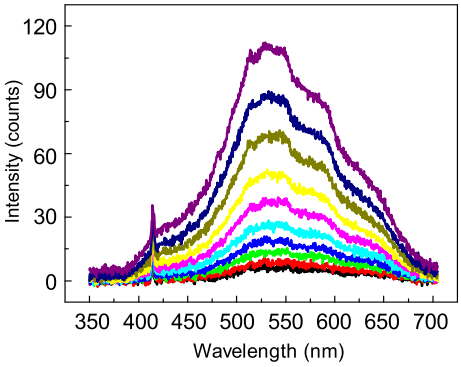

Figure 4.12. Nonlinear emission spectra of a fiber-coupled gold nanorod under the different excitation power.

To fully determine the two nonlinear processes, we measure a series of nonlinear emission spectra as a function of excitation laser power from 330 mW to 600 mW, for a typical coupled system (shown in Figure 4.12). The incident laser is fixed at 828 nm which matches the resonance of the plasmon-fiber cavity.

By assuming again incoherent interplay between SHG and MPPL, we are able to plot SHG peak intensity and MPPL integrated intensity (area of the MPPL envelope from 380 nm to 700 nm) in dependence of the excitation power. The results are plotted in Figure 4.13(a) on double logarithmic scale (red squares and open circles, respectively). The measurement results are then fitted by a linear function, where the fitted slope represents the nonlinear order. The red and black solid curves exhibit excellent fitting for SHG and MPPL, where the SHG process is confirmed by the slope of 2, while MPPL seems to involve cascaded absorption of higher photon numbers (slope of nearly 5).

In order to gain more insight on the MPPL process, we evaluate the MPPL intensity at each emission wavelength as a function of the laser power so that a spectrally resolved analysis of the excitation power dependence can be achieved (see Figure 4.13(b)). Despite increasing fitting error on both edges (near 450 nm and 650 nm) due to the limitation of our setup, the nonlinear order shows a clear trend of monotonic decrease towards longer emission wavelength. The slope changes from roughly 6.1 to 4.5 from 450 nm to 650 nm, leading to an average nonlinear order of about 5. To demonstrate our reliable fitting, data points at four selected emission wavelengths are given in Figure 4.13(c) in detail (marked by A, B, C, and D), where excellent linear fitting is confirmed by solid curves.

Similar phenomena of high-nonlinear-order MPPL sensitive to emission wavelength have recently been reported by V. Knittel et al.[139] A hot electron bath out of equilibrium can be created when the material interacts with intense ultrashort pulses and hence the exponential tail of the Fermi-Dirac distribution generates the high-energy photoluminescence with an effectively higher nonlinear order.[137, 139] Additionally, it has been found that the MPPL order is

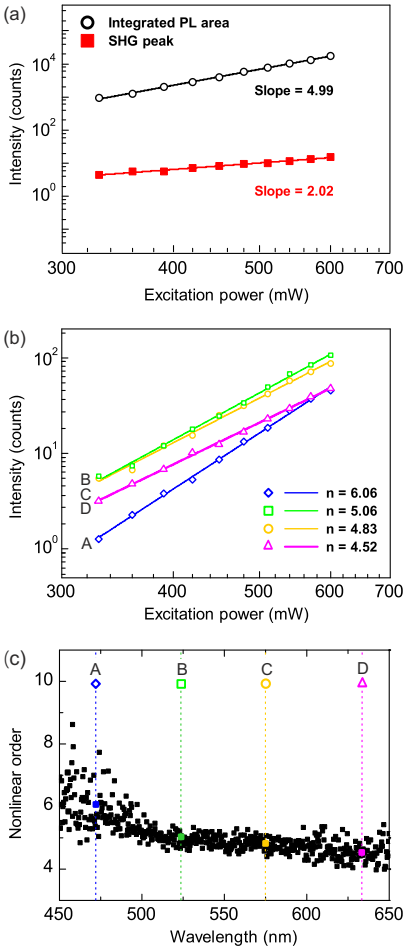

Figure 4.13. Power dependence of the nonlinear emission obtained from a gold nanorod on a tapered fiber. (a)Peak intensity of SHG and integrated intensity of multiphoton photoluminescence in dependence on excitation power. Excellent linear fitting at log-log scale shows anticipated power-law of the nonlinear responses. (b) Nonlinear order of MPPL as a function of emission wavelength. The vertical lines (A, B, C, and D) mark spectral positions where the measurements and fits of the power dependence are shown in (c). The experimental data points in (c) are denoted by symbols, while the solid lines in this double-logarithmic graph show the linear fits determining the nonlinear order plotted in (b).

sensitively dependent on the pump laser properties as well.[136, 169] Its spectral shape is related to the geometry and crystallinity of the gold nanoparticles.[137, 180, 181] In our hybrid systems, the MPPL yield can be similarly high or even much stronger compared to SHG scattering, when the excitation laser hits the resonance perfectly (also see the insets of Figures 4.10(b) and (d)). Such an efficient MPPL emission with nonlinear order up to 6 is very rare in single gold nanoparticle systems reported so far and might also benefit from the large nonlinearities of our hybrid cavities.

4.4.2 *MPPL from the fiber-coupled gold nanobipyramids*

Very interestingly, when we measure the nonlinear responses from the fiber-coupled gold nanobipyramids, the MPPL spectra shows the different features with two distinguished peaks when compared the fiber-coupled gold nanorods in Section 4.4.1. It proves that the MPPL processes also depend on the morphology. How the size and geometry influence the MPPL processes is another complicated question. Here, basically, we should first determine the certain PL processes corresponding to two peaks at the different spectral range.

Figure 4.14(a) and 4.14(b) depict the linear and nonlinear scattering spectra of an isolated gold NBP on the tapered fiber surface. Besides the narrow second harmonic peak, two peaks on the broad luminescence background can clearly be seen in the nonlinear spectrum. Considering these two distinguished peaks showing up, a representative multiple peak Lorentz fitting for the luminescence back ground in the wavelength range between 425 – 680 nm is depicted as green curve (cumulative fitting) in Figure Figure 4.14(b). It shows excellent match with the measurement result. In addition, two spectra centered at 520 nm and 360 nm generated from the fitting results are shown as red and black curves in Figure 4.14(b). They could be considered arising from two different PL processes.

In order to determine which PL process takes place at what spectral position, we measured and recorded a series of nonlinear emission

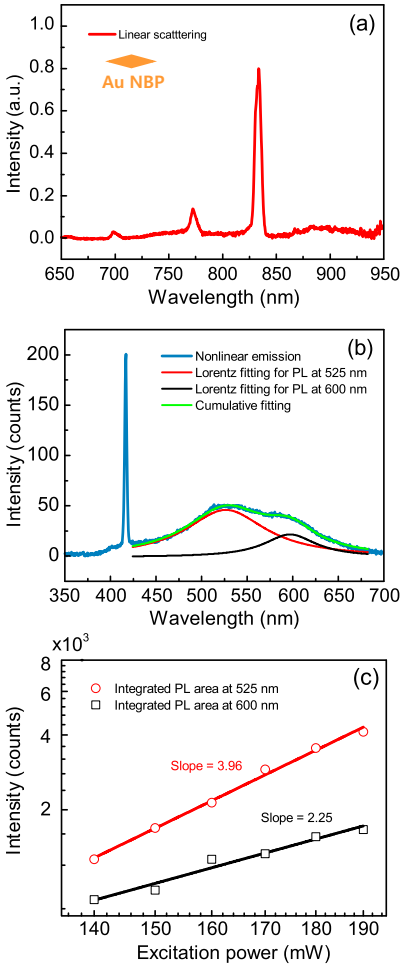

Figure 4.14. (a) Measured scattering and (b) nonlinear emission spectra of a single gold nanobipyramid particle on a tapered fiber surface. The red and black curves in (b) show the results of multiple (two) peaks Lorentz fitting for the broad PL emission spectra (blue curve) in the range from 425 nm to 600 nm. The cumulative fitting result (light green curve) fits the measurement spectrum excellent. (c) Integrated intensity of multiphoton photoluminescence centered at 525 nm and 600 nm in dependence on the excitation power. Excellent linear fitting at log-log scale shows anticipated power-law of the nonlinear responses.

spectra excited with laser powers from 140 mW to 190 mW. Meanwhile, in this measurement, the incident laser wavelength is fixed at 830 nm to match the linear resonance of the coupled system. After applying the multi-peak Lorentz fitting to all the measured nonlinear emission spectra above in the same wavelength range, we are able to plot integrated intensities of these two peaks as a function of the excitation power on a double logarithmic scale. The results are displayed in Figure 4.14(c) as red open circles and black squares while the linear fitting of them are depicted as red and black lines. The slope of fitting lines gives the nonlinear order, namely 2.25 for the PL centered at 600 nm and 3.96 for that at 525 nm. Therefore, we can conclude that the PL process at shorter wavelengths range is mainly dominated by 4PPL, while that one at longer wavelength range is mainly 2PPL.

Compared to the method used in section 4.4.1 and some other studies[138], in particular spectrally resolved analysis of the nonlinear order, this analysis combined with the multiple peak Lorentz fitting is more appropriate for the case of two PL peaks arises in the nonlinear response spectra. It provides us with most precise information about the nonlinear PL process. Considering the multi-peak Lorentz fitting is carried out in the wavelength range from 425 nm to 680 nm to exclude the SHG effect, the nonlinear order is possibly influenced somehow by the missing part in the shorter wavelength range. In addition, there might be a competition between the 2-photon and 4-photon processes to make a bigger value than 2 for the PL centered at 600 nm.

In order to investigate the polarization characteristics of the PL emission, a polarizer is placed in front of the spectrometer and utilized to perform the emission polarization analysis. As mentioned before, considering the side-illumination and the random orientation of the gold NBPs on the fiber surface, the excitation polarization parallel to the optical table is generated and rotated by a half-wave plate.

Figure 4.15 indicates the dependence of the nonlinear emission intensity on the polarizations of the emitted photons. Unexpectedly, the polarization characteristics of the PL centered at about 525 nm

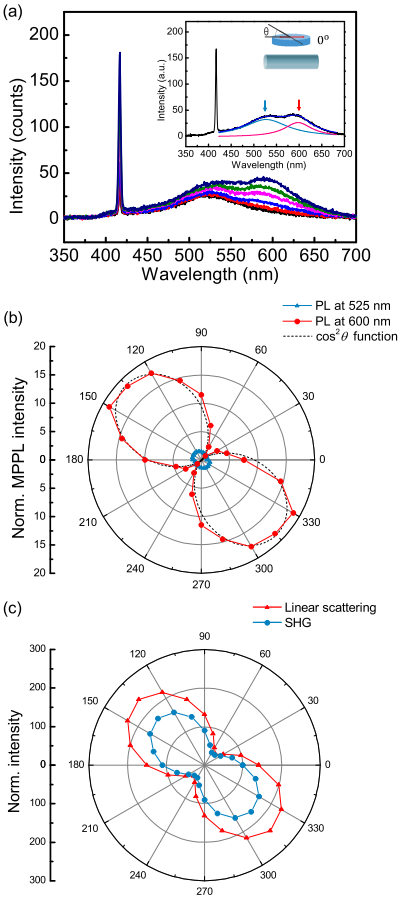

Figure 4.15. (a) Measured nonlinear polarized emission spectra. Inset figure shows the typical two peaks Lorenz fitting for each nonlinear emission spectrum in the range from 425 nm to 680 nm. (b) Polar plots of the fitted PL area centered at 525 nm (blue curve) and 600 nm (red curve) as a function of angle θ. The dashed black curve shows a $cos(2\theta)$ function that is characteristic for linearly polarized dipolar emission.(c)Polar plots of normalized linear scattering and second harmonic generation intensity as a function of the angle θ.

and 600 nm turn out to be different. In the case of the mixed two PL processes, multiple peak Lorentz fitting is still essential for the precise analysis of polarization characteristics. The inset figure in Figure 4.15(a) is a typical fitted result. The upper figure inside indicates the angle θ of the polarizer related to the long axis of fiber. After the multiple peak Lorentz fitting is applied to all the θ-dependent nonlinear emission spectra in the wavelength range from 425 nm to 680 nm, the polar plots of the intensity of fitted PL integrated area as a function of angle θ are displayed in Figure 4.15(b). It proves unambiguously that the 4PPL centered at 525 nm (blue triangles) exhibits definite random polarization, while the 2PPL centered at 600 nm (red dots) shows an almost perfect linear polarization along a certain direction, which is the same as that of the linear scattering emission (Figure 4.15(c)). This direction is supposed to be along the long axis of the gold NBP. The black dashed line in Figure 4.15(b) is a theoretical linearly polarized dipolar-emission generated from a $cos2\theta$ function. It perfectly matches with our measurement results.

In order to confirm the supposed linear resonance enhanced 2PPL process, measurement results from another coupled gold NBP are shown in Figure 4.16. A similar linear resonance with narrow linewidth around 5 nm is obtained as shown in Figure 4.16(a). Different from before, instead of the wavelength position of the main peak, we fixed the laser wavelength at 842 nm, at the position of the smaller peak. In this case, a weak 2PPL is detected. Figure 4.16(b) depicts the complete nonlinear response in the visible range. In order to get a stark contrast, the excitation power dependent measurement is taken as well. Through observing any single one of those spectra carefully, one can easily find that the weaker 2PPL makes the PL emission to be a mixed envelope without two distinct peaks. With it, the conclusion is confirmed again that the polarized 2PPL is strongly enhanced by the linear resonance, while the random polarized 4PPL is more determined by the crystalline structure of gold NBPs.

Regarding to the different relative intensity between PL at shorter wavelengths and longer wavelengths, the shape of nonlinear spectrum varies in the different coupled particles. Meanwhile, it makes

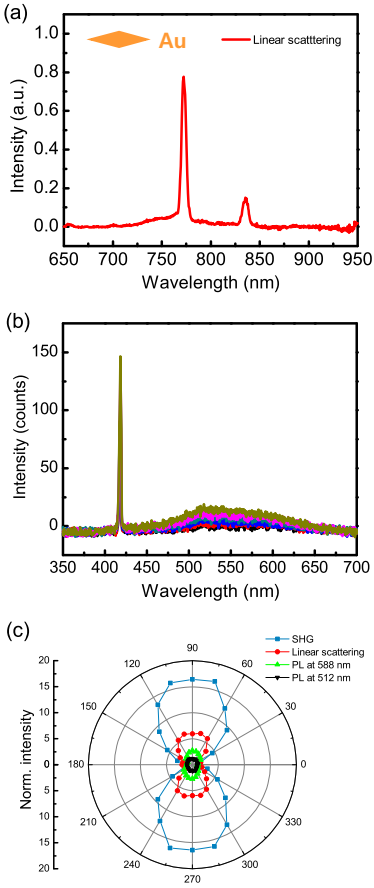

Figure 4.16. (a) and nonlinear emission spectra excited by increasing laser power (b) from another coupled gold NBP. (c) Polar plots of linear scattering, second harmonic generation and PL peak at 512 and 588 nm intensities as a function of the angle θ.

the visible peaks located at slightly different wavelength position. The polarization characteristics of the linear scattering, the PL at 512 nm, the PL at 588 nm and the second harmonic generation are

depicted by the polar plots in Figure 4.16(c). In details, the linear scattering, the second harmonic generation and the PL at 588 nm contain the linear polarization along the same direction. On the other hand, the PL at 512 nm shows almost random polarization. All those characteristics are consistent with the results from the sample in Figure 4.15. It proves the reproducibility of our experiment. It is also worth mentioning that all the measurement conditions during the linear and nonlinear measurement processes are the same with those that are utilized to measure the sample in Figure 4.15.

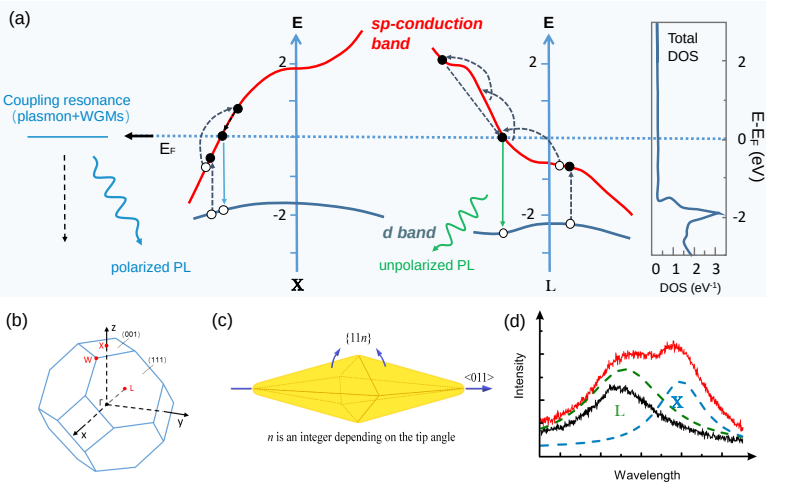

FIGURE 4.17. (a) Sketch of the MPPL process within the gold band structure near the X and L symmetry point (2PPL near the X symmetry point and 4PPL near the L symmetry point). (b) Schematic structure of the gold nanobipyramids. (c) Measured polarized MPPL spectra with maximum and minimum intensity (red curve: $\theta = 135^o$, black curve: $\theta = 45^o$). Green and blue dashed lines are generated from the two peaks Lorentz fitting for the red curve. They correspond to the two processes illustrated in (a) near X and L symmetry points respectively.

The origin of the broadband luminescence from plasmonic metals, which is not related to interband radiative recombination, has also been discussed.[182–184] In those investigations, rough disordered noble-metal nanoparticle films or continuous-wave lasers with low power densities are utilized which are not able to excite efficient MPPL. In contrast, high nonlinearity of our hybrid system is confirmed by the excitation power-dependent analyses as depicted in Figure 4.14(c). Moreover, the 2PPL process in gold nanostructures excited by short pulse laser sources with strong intensities, which are similar to our excitation conditions, has been experimentally demonstrated to be the result of the radiative recombination of the d holes.[157, 185] Combined together with several representative studies about the MPPL, we obtain a complete and convincing scheme of the MPPL process in our coupled gold NBP system as illustrated in Figure 4.17(a). It is well known that in gold crystals optical transitions preferentially occur near the X and L symmetry points in the first Brillouin zone, where the density of states is high. Figure 4.17(a) illustrates the band structures mainly including the sp-conduction band and d-band near the X and L symmetry points. According to the calculated band structure, the band gap energy between the d-band and the Fermi surface near the X and L symmetry points are about 1.9 eV and 2.4 eV, respectively.[186, 187] This implies that the peak of PL emission arising from the electron-hole recombination between sp- and d-bands should be observed at around wavelengths of 652 nm and 517 nm.

The spectral peak position at shorter wavelengths observed in Figure 4.14(b) and 4.15(a) shows perfect agreement with this expectation, while another peak at longer wavelength appears blue shifted compared to the above calculated result. The main reason is that we use the short-pass filter before the spectrometer, which rejects the signal longer than 600 nm. In this case, it turns out to be difficult to reveal a certain peak position. Meanwhile, the intensity of 2PPL can vary in different fiber-coupled Au NBPs, since 2PPL is strongly enhanced by the linear electron oscillation. We will discuss this enhancement effect later.

In Figure 4.14(c), we already determined those two PL processes to rise with powers around 2 and 4, corresponding to the peaks at around 600 nm and 520 nm. Based on it, we conclude that the 2PPL mainly occurs near the L symmetry point and 4PPL preferentially occurs near the X symmetry point. This observation of 4PPL near the L symmetry point provides a solid confirmation of the temporal dynamics measurement results in resonant nanoantennas as investigated in ref [138]. Namely, near the L symmetry point, 4PPL takes place instead of 2PPL when the pulse duration of the excitation laser shortens from >700 fs to 100 fs. The 2PPL process near the X symmetry point in gold crystals has been widely investigated.[167, 188, 189] There is a consistent model that 2PPL is the result of two sequential one-photon absorption steps. In detail, an sp-hole is first created by the first photon. Then the second photon excites an electron from the d-band to recombine with the sp-hole in the conduction band. Afterwards, the hole in the d-band radiatively recombines with the electron from the conduction band, generating the emitted photon. Similar to 2PPL, 4PPL is triggered by sequential steps of photon absorption. Differently, three intraband transitions within the sp-conduction band occur in the first step. In fact, the multi-photon transition process can also result from sp- direct interband transitions as illustrated in ref [138]. Since a cascade of indirect absorption events is unlikely, direct interband transitions are believed to occur more likely. From our view, both processes are possible. The large near-field localization in our hybrid system can result in an increase of higher-order transition moments. In this case, even symmetry rules no longer prohibit intraband transitions. Thus, we just present one of the proposed processes of 3 -photon transitions in sp- band in Figure Figure 4.17(a) in order to specify the exact MPPL process at different symmetry points.

Thus, the following question remains: what causes the big difference in the polarization characteristics of the emitted photons between the 2PPL and the 4PPL in our coupled system? We base our explanation on the band and crystal structure of isolated gold NBPs.

The gold NBPs are chemically synthesized and thus single crystalline. As shown in Figure 4.17(b), the gold NBP is growing along the direction [011]. The side facets are (11n), where n is an integer depending on the tip angle. The allowed transitions of the recombination emission in the X and L regions follow atomic-dipole selection rules. They are restricted to certain directions.[190] In detail, the direction of transition moment in the X region must be parallel to the xy, yz, or xz planes. Directions of x, y, and z are defined in Figure 4.17(b). In other words, it must be parallel to the long axis of the gold NBPs. The observed emitted photons in the X region are perfectly linearly-polarized along the same polarized direction as the linear scattering emission. It is reasonable to suppose that it is caused by the electronic oscillation in the fiber-coupled gold NBP resonantly coupling strongly to the PL as depicted in Figure 4.17(a) (left part with the polarized PL emission. On the other hand, the transition moment in the L region only can take the direction parallel to the (111) planes. In the case of the facets of the gold NBP, the (111) plane is not parallel to any axis of the particle. It means the electric vectors of the emitted photons cannot be parallel to the long axis of the gold NBP. As a result, the PL from the L region is almost randomly polarized. Figure 4.17(d) illustrates this observation briefly. The red and black curves are the PL emission at $\theta = 45^o$ and $\theta = 135^o$, respectively.

The green and blue dashed lines indicate two PL processes generated from the multiple peak Lorentz fitting for the red curve. The PL in the X region is strongly enhanced at $\theta = 35^o$. Meanwhile, the PL in the L region depends on the angle θ quite only slightly. Hence, the polarization characteristics are properly explained by the crystalline structure and the band structure of the gold NBPs. Similar analysis and results about the polarization characteristics has been also described in a different paper[185].

4.4.3 *Quenching effect of 4PPL*

Benefitting from the clarification of the PL process and our understanding of the polarization characteristics of PL emission in the system, we designed fiber-coupled Au@Pd NBP to realize the control of the PL process. The EDX-SEM images for coupled Au@Pd NBP presenting its full profile, gold and palladium element are separately depicted in Figure 4.18. One can see palladium is deposited onto the surface of gold NBP homogeneous.

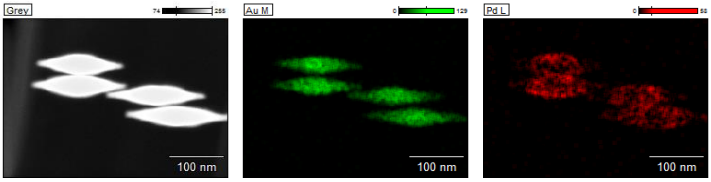

Figure 4.18. Energy-dispersive X-ray (EDX) SEM images of a gold nanobipyramid core@palladium shell structure depicting its full profile(left), gold nanobipyramid core (middle) and palladium shell (right).

Similar to the fiber-coupled gold NBP, an ultra-narrow linear scattering spectrum is achieved by the coupled Au@Pd NBP, as depicted in Figure 4.19(a). Figure 4.19(b) depicts the excitation power dependent nonlinear emission spectra. Quenching of 4PPL must be present as the second peak at the wavelength around 525 nm is absent. On the other hand, the 2PPL at longer wavelength is still observed since it is mainly enhanced by the linear electron oscillation. The nonlinear order of 1.52 is determined by the inset figure in Figure 4.19(b). It is worth noting that this result is influenced by the small intensity and the large noise of the PL signal. Figure 4.19(c) indicates the dependence of the nonlinear emission intensity on the polarization of the emitted photons. Furthermore, the polar plots of the intensity of linear scattering, SHG, and PL integrated area as a function of

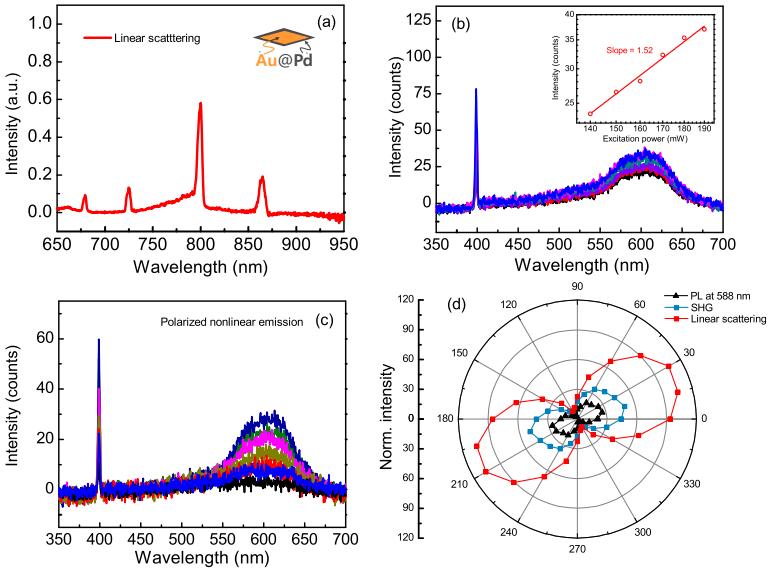

Figure 4.19. (a) Linear scattering spectrum of single (gold nanobipyramid core)@(palladium shell) bimetallic nanostructure on the tapered fiber surface. (b) The nonlinear emission spectra excited by different laser powers and the power dependence of integrated PL intensity (inset figure in (b)). (c) Nonlinear emission spectra from the output analyzer with different polarizations. (d) Polar plots of linear scattering, second harmonic generation and integrated PL intensity as a function of angle θ.

angle θ are plotted in Figure 4.19(d). The PL at longer wavelength is still strongly polarized along the same direction with the linear scattering and SHG. Still similar to the coupled gold NBPs, the PL at longer wavelengths can also vary with the different strength of the linear resonance.

As shown in Figure 4.16, a coupled Au@Pd NBP with weaker linear resonance induces a much weaker nonlinear response compared to that one investigated in Figure 4.19. The 4PPL peak at shorter wavelength is still absent. Meanwhile, a negligible PL peak at longer wavelength is detected. The quenching of PL from the single coupled Au@Pd particle reveals the electron transfer from gold to palladium.

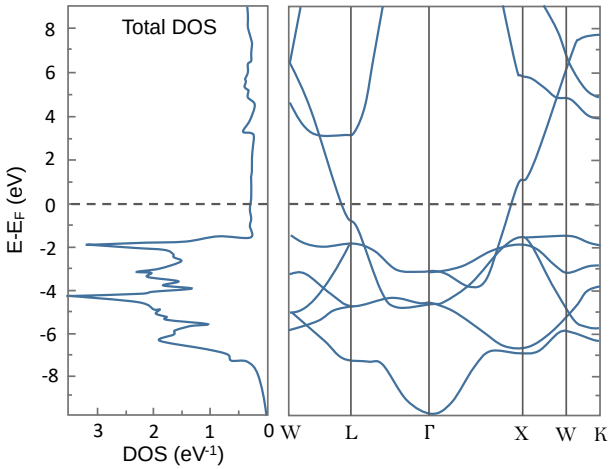

Figure 4.20. Band structure (right panel) and density of states (left panel) plot for gold.

Figure 4.20 depicts the band structure and the density of states for gold.

Figure 4.21(a) present an SEM image of the gold bipyramid core-palladium shell nanostructures, where on can nicely see the palladium covering the surface of the gold. The process can be explained reasonably with the band structure of gold and palladium (band structure and density of states for Pd plotted in Figure 4.21(d)). The d-band in palladium crosses and even exceeds the Fermi surface near the L symmetry point. Meanwhile, the band separation between sp- and d-band is smaller than that in gold. In this case, palladium provides a high density of states between 0 and 2.5 eV (between sp-band and d-band in gold). Thus, the excited electron in the sp-band of gold can transfer easily and fast to palladium before the recombination of electron-hole induces the PL emission. We depict this electron transfer process in Figure 4.21(d). In Figure 4.21(c) we indicate in a simplified energy level scheme an intermediate, lower-energy level

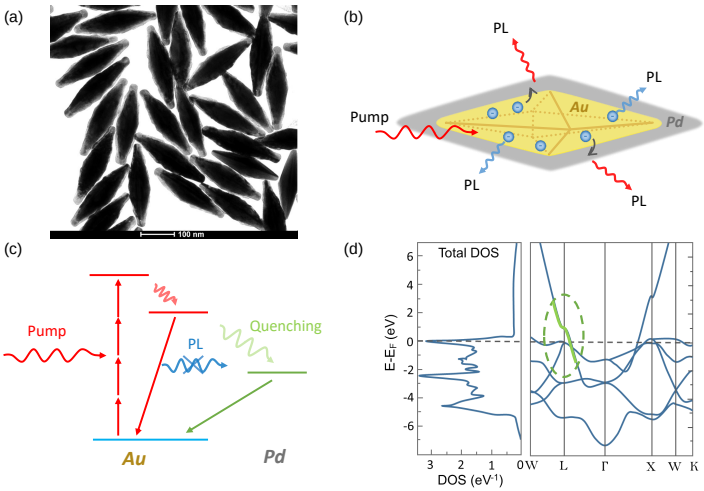

Figure 4.21. (a) Transmission electron microscope (TEM) image of (gold nanobipyramid core)@(palladium shell) bimetallic nanostructures in aqueous solution. Schematic structure of (b) the electron transfer process in gold@palladium bipyramids and (c) quenching process within the band structure of the gold@palladium bipyramids. (d) Sketch of band structure (right panel) and density of states (left panel) for palladium.

in Pd, to which the electrons can transfer after being exited in the gold. As a result, the 4PPL is quenched.

As we discussed before, the 2PPL is strongly enhanced by the linear electron oscillation. Since the linear resonance of coupled Au@Pd NBPs exhibits the similar linear optical properties as that of coupled Au NBPs, the enhanced 2PPL is still observed in the nonlinear spectra.

We already know that 2PPL in coupled gold NBPs is strongly enhanced by the linear electron oscillation. As expected, the 2PPL in coupled Au@Pd NBPs has the same property. Here we verify it from the backforward direction. A Au@Pd NBP with weaker linear scattering intensity than that one in Figure 4.19 is shown in Figure 4.22(a). There is no doubt that the peak intensity of the second harmonic generation is lower. At the same time, the PL intensity turns out to

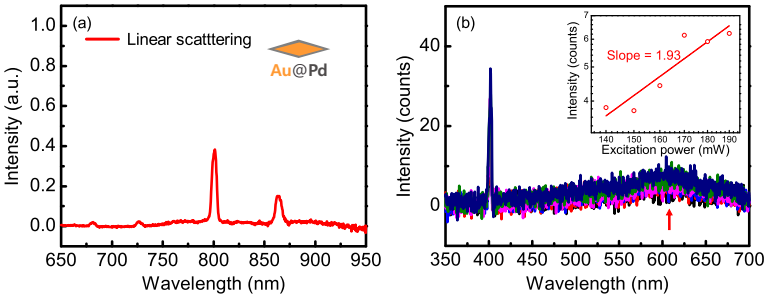

FIGURE 4.22. Linear scattering spectrum (a) and nonlinear emission spectra excited by increasing laser power (b) from another coupled Au@Pd NBP. The power dependence of PL peak intensity at a fixed wavelength (the position of the red arrow) is shown in the inset of figure (b).

be quite small. Specifically, a series of nonlinear response spectra with excitation power ranging from 140 mW to 190 mW are measured (Figure4.22(b)). As the excitation power increases, a quadratic growth of the 2PPL is detected. However, the emission is still feeble. In addition, the quenching effect on the 4PPL is clearly present again with the absence of the PL emission at shorter wavelengths.

4.5 CONCLUSION AND OUTLOOK

In this chapter, we have presented a coupled system between microfibers and plamsonic nanoparticles including gold nanorods, gold nanobipyramids, gold-core and palladium-shell nanobipyramids. In the linear optical regime, we realized the tuning of the wavelength and quality factor of the scattering response by tailoring the size of the microfibers and nanoparticles and also the illumination conditions, which lays a solid foundation to vary the nonlinear optical properties afterwards. The measurement results show that a narrow linear scattering spectrum can be achieved when the plasmon mode of nanoparticles efficiently couples to the whispering gallery modes of the microfibers. Such a narrow linewidth resonance leads to an expected strong second harmonic response and thus an ultranarrow

second harmonic resonance. An extended coupled anharmonic oscillator model based on the model introduced in Chapter 2 is built and implemented to represent the second harmonic resonance in the coupled system.

Besides the enhanced second harmonic generation, multiphoton photoluminescence is also detected with considerable intensity. Unexpected different polarization characteristics of the two PL processes have been observed. The analysis based on the band and crystalline structure of gold NBPs provides us with a deeper understanding of the MPPL process, demonstrating crystal structure dependence. Moreover, quenching of the 4PPL has been detected by coating palladium onto gold NBPs which are coupled to a tapered fiber, resulting from a fast electron transfer from Au to Pd. It opens a new door to design plasmon nanostructures and then modify the MPPL process in isolated nanoparticles which would be required in potential biotechnology applications.

5

HIGH-Q DOUBLY RESONANT PLASMON-FIBER HYBRID CAVITIES

Nonlinear optical processes consisting of second harmonic generation and multiphoton photoluminescence have been studied in Chapter 4. By comparison of the intensity of second harmonic generation between uncoupled gold nanorods and microfiber-coupled gold nanorods, we have clearly seen that much stronger second harmonic responses are detected in the fiber-coupled nanoparticles. Regarding to the theoretical prediction from the anharmonic oscillator model about the relationship between SH intensity and the linewidth of linear resonance, the quality factor dependence of the SHG efficiency was analyzed. It lays a solid foundation for boosting the second-harmonic process. Based on the plasmon-fiber hybrid system introduced in Chapter 4, we propose and study another improved hybrid system, namely high-Q doubly-resonant plasmon-fiber cavity in this chapter

This chapter is mostly based on the following publication:

Q. Ai, F. Sterl, H. Zhang, J. Wang, and H. Giessen,
"**Giant Second Harmonic Generation Enhancement in a High-Q Doubly Resonant Hybrid Plasmon-Fiber Cavity System**",
ACS Nano (2021),
DOI 10.1021/acsnano.1c05970.

5.1 INTRODUCTION

In recent years, a great deal of effort has been put into promoting the nonlinear conversion efficiency, especially the SH conversion efficiency of metallic nanostructures, such as combining nanostructures with highly nonlinear materials,[29, 191–193] designing special non-centrosymmetric structures,[31, 32, 144] utilizing the interaction between localized and delocalized plasmons,[33, 194] etc. Lately, multiresonant plasmonic structures have been investigated and attracted much attention due to their potential for augmenting SHG.[23, 26, 195, 196] These structures are composed of several plasmonic building blocks whose elementary plasmonic modes strongly interact with each other. Thus multiple new hybridized modes are generated and can be designed to be resonant at both the fundamental and the second harmonic frequencies. In this case, the input and signal fields of nonlinear origin are enhanced simultaneously. These enhancement mechanisms have also been demonstrated experimentally.[197] However, due to large damping losses from the metallic structures, the near-field enhancement using those multiple resonant systems is still limited.

In fact, dramatically more efficient nonlinear responses in doubly resonant systems can be expected, mainly considering that the quality factor of the resonances can be drastically improved by designing special coupled systems. For example, relatively high quality factors of up to 100 can be achieved by arranging metal nanoparticles into periodic arrays.[198, 199] A series of studies prove that the light-matter interaction is indeed enhanced in those high-Q plasmon systems.[141, 153, 155, 200] Very recently, the nonlinear responses of multiresonances with high Q factor in an array of L-shaped aluminum nanoparticles has been numerically investigated.[201] An over million-fold enhancement of the emitted SH intensity with conversion efficiency of 10^{-5} has been predicted when compared to an individual particle.

In this chapter, we demonstrate that by coupling to a fiber cavity with the proper diameter, in combination with a single gold nanoparticle a high-quality (Q∼ 160) resonance can be achieved . The high Q of the coupled mode aids a very efficient SHG because in a classical picture the incident electric field travels coherently Q times around the fiber during the nonlinear process. We accomplish two feats: First, we analyze the Q factor dependence of the SHG efficiency, proving the expected Q^4 dependence of the efficiency and thus confirming our coherent E-field amplification in the fiber cavity. Second, we carefully adjust the fiber size further and tune the plasmon response of a gold nanoparticle to a high-Q cavity mode and simultaneously make sure that the second harmonic wavelength is also in resonance with a higher order fiber cavity mode, which fulfills the doubly resonant condition. Thanks to the simultaneous realization of the high quality factor and the doubly resonant case, a giant SH response $5 \times 10^8\ W/cm^2$ for 100 fs pump pulses around 840 nm incident wavelength.

5.2 DESIGN IDEA AND WORKING PRINCIPLE

The idea of enhancing the second harmonic conversion efficiency in hybrid plasmon-fiber cavities is illustrated in Figure 5.1. It mainly includes two steps: The first step is to coat the nanoparticles onto the surface of tapered microfibers (see Figure 5.1(c)) to realize the efficient coupling between plasmon resonance and WGMs. In fact, this step has been realized and investigated in Chapter 4. Here, the gold NBPs are chosen as the component for the coupling systems instead of the gold nanorods due to the stronger electric near-field that can be expected on sharp tips. When illuminated, the gold nanoparticle on the fiber surface acts as an antenna interacting with the incident light. Meanhwile, the tapered fiber as an optical microcavity confines light at resonant frequencies. In such a way, the interaction time is extended and the interaction between light and the gold nanoparticle is altered fundamentally. Thus a high-Q resonance with a large field enhancement can be achieved (see Figure 5.1(d)).

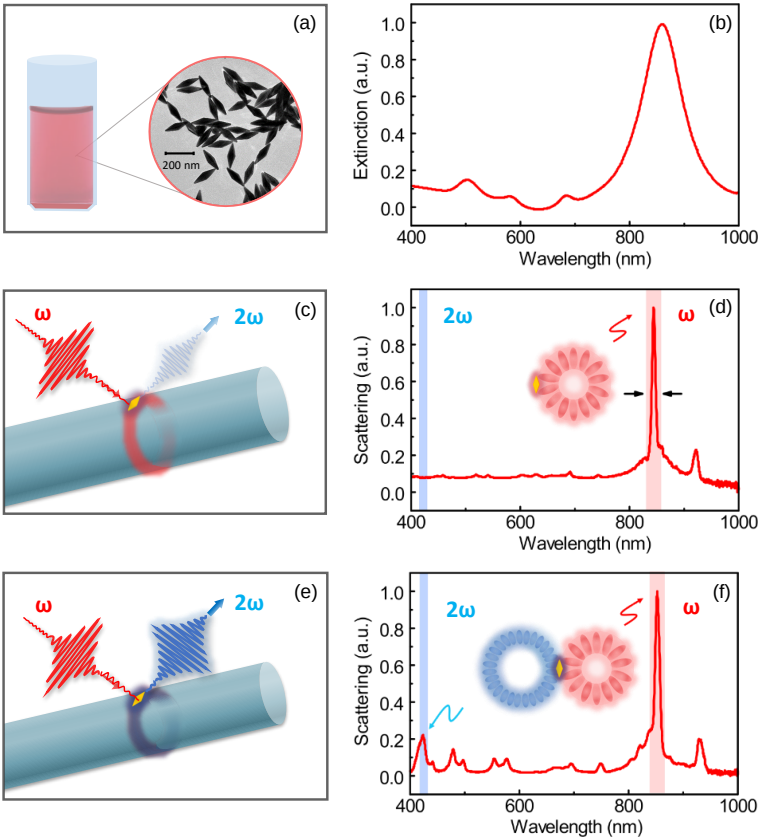

Figure 5.1. (a) Sketch and TEM image of gold nanobipyramids in solution. (b) Typical measured extinction spectrum of the sample shown in (a). (c) Sketch of a hybrid plasmon-fiber cavity. (d) Typical measured scattering spectrum of a hybrid system as shown in (c). (e) Sketch of a doubly resonant hybrid plasmon-fiber cavity. (f) Typical measured scattering spectrum of a doubly resonant plasmon-fiber cavity as shown in (e).

The second step is to decrease the diameter of microfibers in our hybrid system to observe higher-order cavity modes and then tune one resonantly to the SH wavelength by carefully adjusting the size of

the tapered fibers further (see Figure 5.1(e)). In contrast to the former multiresonant systems, in which the second resonance matched to the SH wavelength is just another hybrid plasmon mode, the second mode in our hybrid system arises from the coupling between the nanoantenna and the optical cavity. In this case, both the fundamental and the SH light are supposed to circulate and interact dozens of times in a coherent fashion inside the microcavities. This leads to high-Q resonances with a strongly enhanced response in both linear and nonlinear regimes (see Figure 5.1(f)). As a result, giant SHG can be achieved by enhancing the quality factor and by tuning into a doubly resonant condition.

In general, gold nanoparticles in an aqueous solution or on fused silica substrates feature only a weak plasmon resonance with a low quality factor mainly due to the large damping losses from the metallic nanoparticles. Single-crystalline gold nanobipyramids (NBPs) that be used in this paper were synthesized using an optimized seed-mediated method starting with a wild thermal treatment of common seeds. The high-purity NBPs with certain longitudinal surface plasmon resonances can be grown by modifying various parameters in the growth solution. Synthesis details are described in the Chapter 2.

The transmission electron microscopy image of the gold nanobipyramids (NBPs) is depicted in the inset of Figure 5.1(a). Figure 5.1(b) displays the UV-VIS spectrum of the corresponding NBPs in aqueous solution. Corresponding to the central wavelength (λ) 937 nm and the resonance linewidth ($\Delta\lambda$) around 100 nm, the Q-factor ($\lambda/\Delta\lambda$) is less than 10. When they are coated onto a fused silica substrate, the central wavelength of the individual particles will blue shift to around 860 nm (see Supplementary Figure 5.2) due to the change of refractive index of the surrounding materials. The full width at half-maximum (FWHM) of the scattering spectrum is still broad at around 100 nm (see Supplementary Figure 5.2).

The microfibers used in our coupled system are still manufactured by tapering single-mode fibers with a homemade flame-heated pulling machine which enables precise tailoring of the diameter of the

tapered fibers as well as their waist length. By drop coating the properly diluted gold NBPs onto the microfibers, hybrid plasmon-fiber cavities can be realized after they dried in ambient air. When the diameters of fibers are smaller than 2 μm, the Q-factor of WGMs of the pure fibers are less than 10.[88] In this case, the Q factors of plasmon resonance and the WGMs are comparable and thus they can easily couple to each other. Due to the large interparticle distance, no dipole-dipole coupling between two gold nanoparticles occurs. When gold NBPs are deposited on a microfiber with a diameter around 1.65 μm (see Figure 5.1(c)), a very narrow hybrid plasmon-fiber resonance with high Q factor of up to 160 is detected (see Figure 5.1(d))).

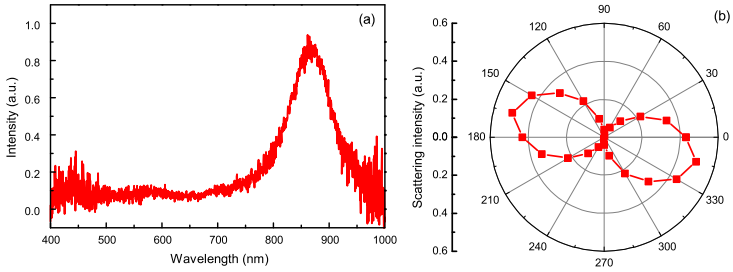

Figure 5.2. (a) Measured scattering spectrum of an isolated bare gold NBP on the silica substrate (using a Nikon TU Plan ELWD 50x, NA 0.6 dark-field objective). Considering the weak plasmon response from the single gold particle on the substrate, the polarization properties are detected to confirm that the particle we measured in (a) is an isolated gold NBP as depicted in (b).

In fact, a diameter of 1.65 μm is the proper fiber size to obtain the narrowest hybrid resonance, which was substantiated by a series of experiments. As the diameter of the fiber continues to decrease, the coupling with the light at fundamental wavelength turns out to be weaker, while some larger frequency modes arise, exhibiting weaker coupling (as displayed by the peak with the blue-striped background in Figure 5.1(f)). By carefully tuning the fiber diameter

to 1.44 μm, one of those higher-order cavity modes is matched to the SH wavelength(as displayed by the peak with the red-striped background in Figure 5.1(f)). In this case, the quality factor turns out to be smaller due to weaker coupling, but is still as high as 100. More details will be discussed later with regards to Figure 5.6.

5.3 QUALITY-FACTOR-DEPENDENT SECOND HARMONIC RESPONSE

We always emphasize the importance of revealing determines the properties of second harmonic generation in metallic nanostructures. Arrays of L-shaped gold particles were investigated for their SHG properties. The efficiency was found to depend strongly on particle ordering in the array[35]. Meanwhile, it was shown that geometric shape factors in some specific structures influence the resonant enhanced SHG significantly. For example, the spacing between two holes plays a key role in the generation of second harmonic emission.[36] A various of SHG of several orders of magnitude can be achieved by tuning the aspect ratio of rectangular holes.[202] Furthermore, the explicit origin of shape effect in these nonlinear optical nanostructures is investigated both experimentally and theoretically.[37] Another interesting observation must be mentioned here, that is breaking of the centrosymmetry doesn't induce an increasing SH intensity in coupled plasmonic nanoparticles, compared to the symmetric systems.[24, 38]

Hence, so far, the fundamental mechanism of those enhancement fact is still not clear. It is even a big challenge to completely describe the SHG process both the experimentally and theoretical side.[39, 40, 42, 203] However, it is evident that a resonance at the fundamental frequency and its quality are crucial for all the harmonic generation.[19, 43, 44, 204, 205] The anharmonic oscillator model has been already utilized well to predict a nonlinear signal that is superlinearly proportional to the inverse of the resonance linewidth,[47, 200, 206] which is directly related to quality factor. Nevertheless, a clarified Q-dependent SHG figure is still lack and highly desired.

The attractive properties of our fiber-coupled system are not only the enhanced optical response but also the tunable Q factors. As discussed in Section 4.2.2 of Chapter 4, the coupling strength and thus the quality factor in our hybrid system are mainly determined by the size of the gold NBPs and the diameters of the microfibers. Meanwhile, they are also varied by the different orientation of the particles lying on the fiber surface. This property was nicely demonstrated by Wang et al.[88] Meanwhile, the tapered fibers have a waist-like shape, which changes the cavity size slightly with respect to the positions of the particles on the fiber surface. Those properties enable us to study the hybrid systems with different Q factors. It is worth mentioning that the incident angle influences both the wavelength position and the linewidth of the hybrid resonance. Thus the excitation conditions including the incident angle and the focus case are kept the same during the entire measurement processes demonstrated in this paper.

The dark-field scattering microscopy setup depicted Figure 5.3 was utilized to perform linear and nonlinear spectroscopy. It is necessary to point out that compared to the one used in Chapter 4 some difference is made. Now both the white light and laser source are focused through the same lens, which can eliminate the influence of the incident situation. In Section 4.2.2 of Chapter 4, we discussed the incident angle dependent coupled resonances. When the excitation is collimating light, the incident angle can be considered as approximately the same, while, it will turn out to be a range of angles after the light is focused through lens. In this case, the coupled resonance will be broader when compared to the case with the sinlge-angle excitation. Regarding to this change direct related to the Q factor of systems, we develop the experimental setup as shown in Figure 5.3. With this setup, the white light in the linear response measurement and the laser source in the nonlinear response measurement can be easily switched while maintaining the same incident condition.

The linewidth $\Delta\omega$ of the linear resonance that corresponds to quality factor plays a key role in the nonlinear yield, as has been shown by an anharmonic oscillator model introduced in Section 4.3.2 of Chapter 4 Combined with the fact that the second-order nonlinear

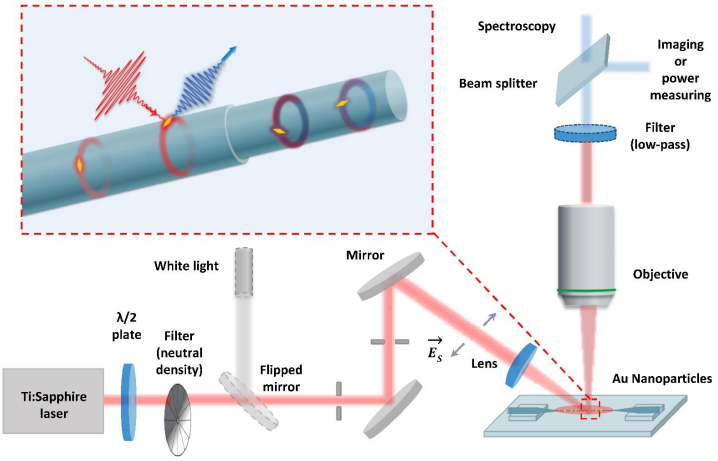

Figure 5.3. Schematic dark-field setup for white light scattering and nonlinear spectroscopy. The schematic diagram of the coupling system between isolated Au nanobipyramid particles and optical microfibers are shown in the red dashed frame. The orientation of the Au NBPs, the position of those particles on the surface of fibers and the tapered fiber sizes together determine the coupling strength between the gold NBPs and microfibers, thus induce both the linear and the nonlinear response with different intensity. The incident light is s-polarized.

polarization scales quadratically with the fundamental field intensity, the anharmonic oscillator model predicts that the nonlinear efficiency of SHG scales to $1/\Delta\omega^4$.

In order to study the Q-factor dependent SHG efficiency, we did the linear and nonlinear microspectroscopy for five hybrid plasmon-fiber cavities with different Q-factors as displayed in Figure 5.5. The gold NBPs displayed in Figure 5.1(a) are coated on the microfibers with diameters in the range of 1.70 – 1.90 μm. The spectra in the left column of Figure 5.4(a-e) present their linear scattering spectra. The FWHM of their Lorentz fitting resonances (blue curves in Figure 5.4(a-e)) varies from 8.4 nm to 5.1 nm, which are picked smaller than

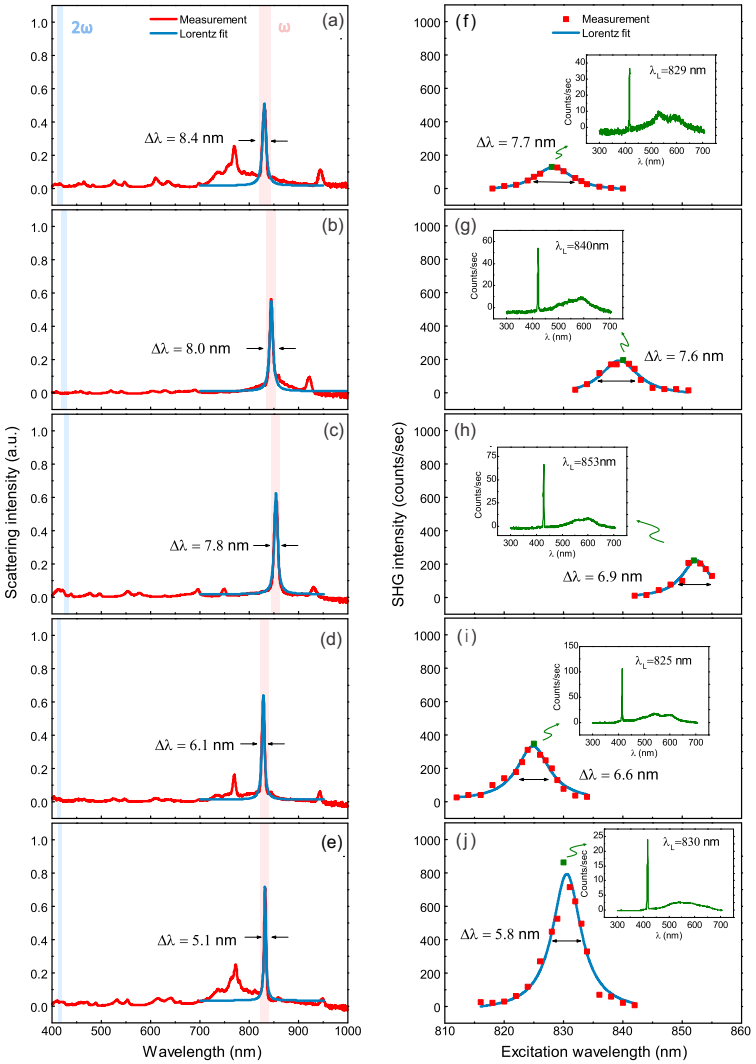

FIGURE 5.4. Q-dependent second harmonic generation. The figures at left (a-e) are scattering spectra of singly resonant coupling systems. The Q-factors vary from 96 to 160. The figures (f-j) at the right are their corresponding SHG efficiency as a function of excitation laser wavelength. The inset figures are the nonlinear emission spectra at the SHG resonance peak wavelength. The excitation and measurement conditions are kept the same during both the linear and nonlinear measurement processes.

the linedwidth of the laser spectra (9 nm). Their corresponding Q-factors range from 96 to 160. When efficient coupling between the plasmon resonances of the gold NBPs and the cavity modes resonant at around 840 nm occurs, other cavity modes are barely coupled to the plasmonic particle and thus no photons at other frequencies are radiated from the plasmonic antenna.

Next, the samples were illuminated by the laser and their nonlinear response spectra were detected and displayed in Figure 5.4(f-j). The green curves in the insets of Figure 5.4(f-j) are the nonlinear response spectra corresponding to the green squares in the SH resonances which occur when the laser excitation is at the peak wavelength of the linear resonance. A narrow SHG peak and broad photoluminenscence (PL) are both observable. The analysis of the photoluminenscence in this system was done in Section 4.4.2 of Chapter 4. By tuning the central wavelength of the excitation laser over the linear resonance step by step, we obtain a series of nonlinear emission spectra. For each spectrum, we determine the integrated SHG area by taking the overall SHG intensity minus the PL values. After plotting them as a function of excitation wavelength, the nonlinear spectroscopy gives rise to a narrow second-harmonic resonance as shown in Figure 5.4(f-j).

The linewidth of the SHG peak ranges between half the linear resonance linewidth and half the laser spectral width. Meanwhile, as the linewidth of the linear resonance decreases, which corresponds to a bigger Q-factor, the SH resonance turns out to be narrower as expected, while the SHG intensity increases. It is worth to mentioned that there are no other scattering linear resonant modes exist at the SH wavelength area as depicted with the blue stripes in Figure 5.4(a-e). The mode overlap between the nonlinear polarization and its harmonic modes is another key schematic to enhance the SH responses. Thus avoiding influence from the modes overlapping is necessary to analysis the Q-dependent SH efficiencies.

In order to investigate the Q-dependent SHG behavior, we plot the peak intensity of the SH resonance of those five systems as a function of their system quality factors and fit them by a linear function,

as shown in Figure 5.5(d). The results clearly demonstrate the Q^4 dependence of SHG efficiency as expect. The SHG peak intensity of the system with Q factor 165 shown in Figure 5.4(e) and 5.4(j) is enhanced by more than one order of magnitude compared to the system with a Q factor of 95 shown in Figure 5.4(a) and 5.4(f).

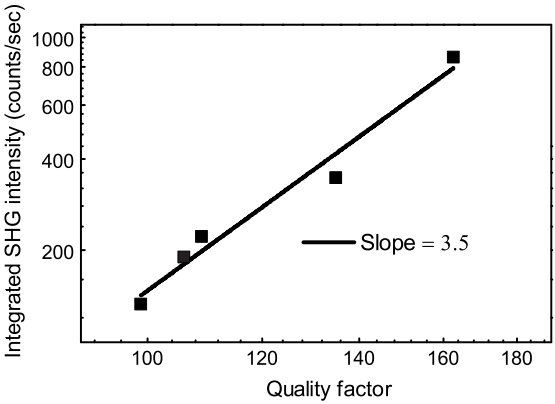

Figure 5.5. Q dependence of the SHG intensity. Five black squares correspond to the plasmon-fiber cavities shown in Figure 5.4.

Benefit from the plamson-fiber hybrid systems with tunable quality-factors as depicted in Figure 5.4, this power dependence is investigated in Figure 5.5 by plotting the peak intensity of the SH resonance of those five systems as a function of their system quality factors on a double-log plot. The Q-factors of those five hybrid systems are 97, 105, 112, 137, 164, respectively. By fitting them (black squares in Figure 5.5) by a linear function (black line in Figure 5.5), a slope of 3.5 is obtained, which presents the $Q^{3.5}$ dependence of SHG efficiency. This results matches well to the Q^4 relationship as predicted with a reasonable deviation. The deviation is believed mainly caused by the experimental conditions, especially the short laser pulse stabilities. We also considered other minute factors which

are in general claimed to affect the nonlinear efficiencies, such as the geometries and asymmetry ratios. It is true that the individual differences of the chemically synthesized gold nanoparticles cannot be avoided, even though those nanoparticles used in this work are from the same patch of the particle solution. Meanwhile, the symmetry profiles of the whole system vary with the coupling conditions between the gold particles and fiber cavities. In our case, it is decided by the coupling positions and orientations of the gold NBPs on the fiber surface. However, those elements also result in the different Q factors of the linear scattering spectra. Thus, we supposed that they have been included into Q-dependent SHG. Even if it is not the case, they play much weaker roles in the nonlinear efficiency compared to the quality factors.

In conclusion, we have experimentally demonstrated a coupled gold nanoparticle with tunable quality factors and systematically quantized how the nonlinear efficiencies, specifically of the SHG responses depend on the quality factors. Without introducing new high nonlinear materials or changing the sizes and shapes of the nanoparticles, the Q factors are tuned simplify by controlling the coupling between the plasmon modes and cavity modes. By developing a microspectroscopy setup with easily switchable two excitation resources, a reliable result of the $Q^{3.5}$ dependent SHG intensity is achieved. This result confirms the theoretical result predicted from the anharmonic oscillator model and explains reasonably the SHG enhancement effect of the high-Q systems in the former researches. It demonstrates clearly the importance of the high Q factors for efficient nonlinear light emission in designing and fabricating plasmonic structures.

5.4 GIANT SECOND HARMONIC GENERATION ENHANCEMENT

As mentioned before, 1.65 μm is the proper fiber size to couple with the gold NBPs used in this work. The electromagnetic energy of certain frequencies perfectly matches the modes of this whispering gallery without too much energy leaking.

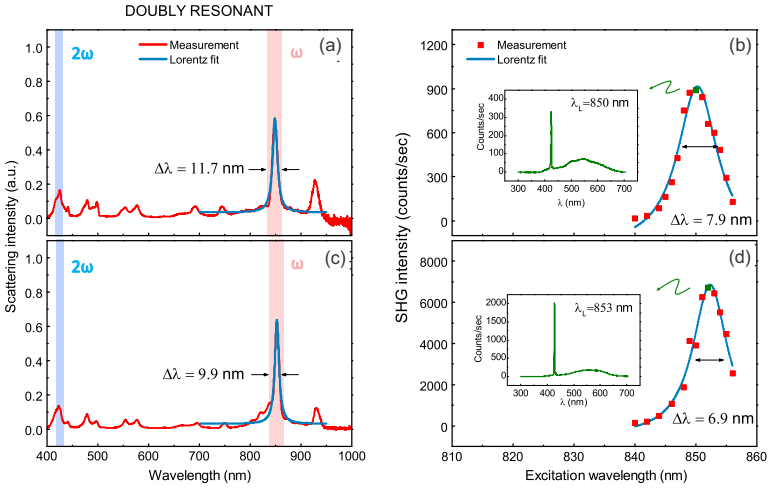

Figure 5.6. (a,c) Scattering spectra (red, measurement; blue, Lorentz fit) from two gold bipyramids coupled to the same microfiber with diameter about 1.4 μm, while (b,d) are their corresponding SHG efficiency as a function of excitation laser wavelength (red dots, measurement; blue curves, Lorentz fit). In (b,d), nonlinear emission spectra at peak wavelength of SHG resonance are shown in the inset (green curves). The FWHM linewidths $\Delta\lambda$ of the linear and the second-harmonic resonances are marked in (a-d).

As the diameter of the tapered fiber decreases, the higher-order cavity modes appear. By fine-tuning the fiber diameter to 1.44 μm, we obtain a *doubly* resonant system as displayed in Figure 5.6(a) and 5.6(c). The FWHM of those two typical systems are 11.7 nm and 9.9 nm. The corresponding Q factors are 73 and 86 respectively, which are somehow smaller than the perfect coupling systems as depicted in Figure 5.5 and Figure 5.4. On the other hand, the evident higher-modes are detected. the higher-modes overlap with the SHG spectral position of the laser (indicated by the blue vertical stripe). By sweeping the laser wavelength over the linear resonance range, we obtain a series of nonlinear emission spectra, and typical ones are plotted as the insets of 5.6(b) and 5.6(d) as green curves. After plotting the SHG peak intensity as a function of excitation wavelength, the

nonlinear spectroscopy reveals narrow second-harmonic resonances of those two systems. By comparing the doubly resonant systems (see 5.6, all normalized to the same incident power and exposure time) to the singly resonant systems (see Figure 5.4), the SHG peak intensity exhibits over *two orders of magnitude enhancement* even though the Q-factors are smaller. Meanwhile, the linewidths of the SH resonances of doubly resonant systems are narrower than those of singly resonant systems with equal Q-factor. This proves once more that the doubly resonant case enhances the nonlinear response by matching the SH light inside of the optical fiber cavities.

5.4.1 *Nonlinear response comparison between isolated gold NBPs on the substrate, singly and doubly resonant plasmon-fiber cavities*

All the measurement results shown in Figure 5.4 and Figure 5.6 are obtained under the same experimental condition, including the incident case, spectral solved setup and so on. When compared to the intensity of the second harmonic generation spectra in the singly resonant hybrid cavities, 50-fold enhancement of the SHG is achieved in the doubly resonant hybrid cavities with even smaller Q factor. It proves the enhancement effect from the doubly resonant cavities.

In order to confirm the huge SHG enhancement effect from our tailored high-Q doubly resonant systems further, we compared the nonlinear emission spectra from typical doubly and singly resonant systems with individual gold NBPs on a fused silica substrate. The excitation conditions and spectroscopy processes remained exactly the same during this comparison. By comparing Figure 5.7(a) to 5.7(b), we clearly find that the SHG peak is orders of magnitude enhanced by the doubly resonant case, while the intensities of fundamental peaks display a similar level. This proves that the second harmonic conversion efficiency is indeed drastically boosted by the doubly resonant case.

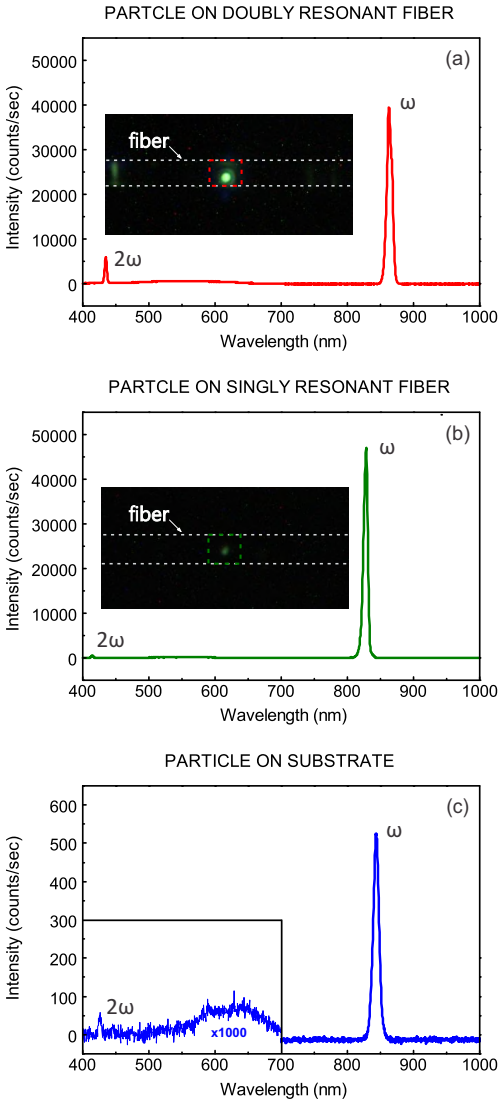

Figure 5.7. (a) Spectrum showing the fundamental mode and the SHG for the doubly resonant plasmon-fiber cavities. (b) Spectrum showing the fundamental mode and the SHG for the singly resonant plasmon-fiber cavities. Insets in (a-b) shows the SH light recorded by camera. (c) Spectrum showing the fundamental mode and the SHG for particle on the substrate. The intensity of left-bottom spectrum is amplified 1000 times.

As reference, the nonlinear emission spectrum of a single gold NBP on a fused silica substrate is displayed in Figure 5.7(c). As mentioned, the plasmon resonance from a single gold particle is quite weak because of the large damping losses (see Figure 5.2). Hence the fundamental scattered laser peak in the spectrum shown in Figure 5.7(c) is also quite weak compared to those in the fiber-coupled systems, as displayed in Figure 5.7(a) and 5.7(b). The nonlinear response spectrum with SHG peak in the left bottom of Figure 5.7(c) is amplified 1000 times. Even though the exposure time here is 20 minutes, the spectrum is still quite noisy. In fact, in most cases the SHG peaks cannot be detected with the same excitation power (160 mW) with an exposure time of 20 minutes. The nonlinear response under side-illumination conditions from the particles also depends on their orientation on the substrate. With a certain incidence angle and s-polarization, the particles with random orientations on the substrate possess different phase matching conditions with respect to the excitation light. Considering the weak nonlinear response, a set of measurements for the particles on the substrate have been carried out. Typical ones are displayed in Figure 5.8.

Comparing the intensity of SHG peaks in the nonlinear emission spectra of the doubly resonant system (around 6000 counts per second, Figure 5.7(a)) and the particle on the substrate (0.055 counts per second, see Figure 5.7), over five orders of magnitude enhancement is achieved. Photographic snapshots of the second-harmonic images of the particles are displayed as insets of Figure 5.7(a) and 5.7(b) and have been taken with an Allied Vision GC2450c CCD camera behind a short-pass filter and connected to our dark-field reflection setup as imaging component (see Figure 5.3). The observed green color is determined by the wavelength-dependent camera efficiency.

5.4.2 *Conversion efficiency of second harmonic generation*

Although the SHG enhancement factor of the doubly-resonant cavities is determined by the comparison measurement to the isolated gold NBPs on the silica substrate and the singly-resonant cavities,

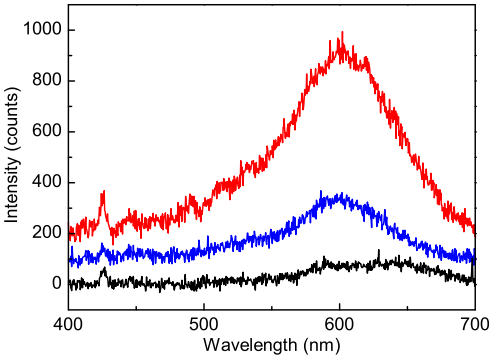

Figure 5.8. Three typical nonlinear response spectra of isolated gold NBPs on the fused silica substrate. The exposure time for detecting these spectra is 20 minutes.

the real intensity of the SH response is still needed to calculate the SH conversion efficiency. In order to quantify it, we use an indirect method to measure and calculate it as introduced in Appendix. A similar method to estimate the SH output power has also been utilized by other groups.[207] The conversion between the intensity and the counts taken from the spectrometer can be realized throughout the entire wavelength range.

Through assuming that almost all the SHG is emitted towards the objective side and collected by the objective, and by considering the losses due to the transmittance of the objective (85%) together with the short-pass filter (87%) in the collection path at SH wavelength, we get an SHG peak power 0.28 μW corresponding to 6000 counts/s shown as the blue square in the Figure 5.9 according to the result of power calibration of the spectrometer.

By considering the spot size of the excitation laser beam imping onto the sample (an oval area with long axis 800 μm and short axis 100 μm) and absorption cross-section of 56000 nm^2 of the isolated particles, we estimated that the SH conversion efficiency of $P_{SH}/P_F \cong 1.59 \times 10^{-5}$, where P_{SH} and P_F are the estimated average

power for the SHG emission and the FW illumination, respectively (see Table 5.1).

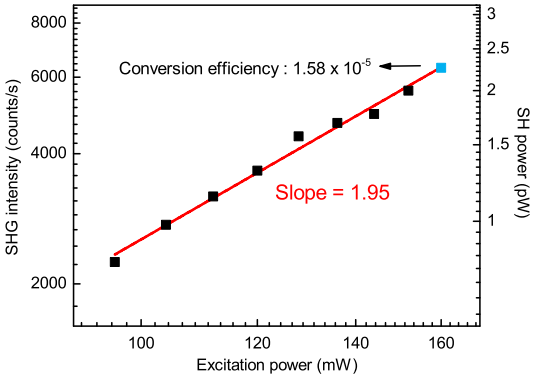

Figure 5.9. Excitation power dependence of SHG obtained from a doubly resonant system. The left y axis displays the SHG intensity directly measured with the spectrometer. The right y axis shows the corresponding calibrated SH peak power.

In fact, this metric is commonly used in the case that the finger print of the structure is much smaller than the excitation spot.[208] Meanwhile, the maximum employed incident power (160 mW) provides $5 \times 10^8\ W/cm^2$ pump intensity[26] which is well below the nanoparticles damage threshold.[28, 33] It was also verified to result in a stable SHG signal with the expected quadratic dependence on input power (see Figure 5.9). Compared to the doubly-resonant plasmonic nanoantenans with the low Q factor, we have an almost 4-orders-of-magnitude higher SH conversion efficiency. Both the comparison measurement between the coupled gold NBPs and the gold NBPs on the substrate and the calculated SHG peak intensity proves the extraordinarily strong SHG enhancement in our high-Q doubly resonant plasmonic system.

Experimental parameters				
Parameter	Laser repetation rate (MHz)	Laser pulse duration (fs)	Average power at fundamental wavelength (mW)	Spot size (μm^2)
Symbol	ν	τ	P_F	δ
Value	80	100	160	62800
Output power levels				
Parameter	SHG power (pW)	SHG peak power (μW)	Absorption cross-section (nm^2)	Conversion efficiency
Symbol	P_{SH}	$\hat{P}_{SH}$	σ	η_{SH}
Formula		$P_{SH}/\nu\tau$		$(P_{SH}\cdot\delta)/(P_F\cdot\sigma)$
Value	2.26	0.28	56000	1.59×10^{-5}

Table 5.1. Experimental parameters and output power level in the high-Q doubly-resonant plasmon-fiber cavities

5.5 CONCLUSION AND OUTLOOK

In this chapter, we have presented a novel concept of the multiresonant high-Q plasmonic system. It is based on efficient and tailored coupling between gold nanobipyramids and tapered microfibers. Excellent plasmonic properties in the linear as well as the nonlinear regime have been demonstrated experimentally. By tuning the diameters of the tapered fibers, the linewidth of the coupled resonance varies somewhat. The Q factor dependence of the second harmonic generation is analyzed. Besides the property of high quality factor, the doubly resonant condition is obtained by fine-tuning the diameter of the microfiber further. Benefitting from the simultaneous realization of high-Q and doubly resonant condition, a giant SHG intensity is achieved that represents a new record of nonlinear SHG conversion efficiency from single plasmonic nanoparticles. In our system, it is highly challenging to obtain exact quantitative conversion efficiencies due to the large size mismatch between our plasmonic system and the laser spot. In this case, we supposed a method of

power calibration of the spectrometer, which can be used to evaluate the weak signal detected by the spectrometer.

The measurement results in this chapter not only present a strong SH response in this particular system, but also provide us a new thought of designing high nonlinearity plasmonic system. By carefully designing and material engineering with optimized parameters, similar structures such as metasurfaces based on the same working principle could be realized to precisely evaluate the resulting SHG power and its conversion efficiency. Relying on more flexible parameters, even more efficient coupling strength and higher SHG power could be expected in high-Q double-resonant metasurfaces.[201] In addition, some other material which can sustain high temperatures, for example, Titanium Nitride,[209] could be considered to be used to boost the nonlinear process further with higher excitation power. For applications, our system with ultranarrow SH resonances and giant SHG peak intensities is a promising structure to realize nonlinear hydrogen sensing by replacing gold nanoparticles with palladium-capped gold nanoparticles in the future.

6

CONCLUSION AND OUTLOOK

In this thesis, we have explored in detail the nonlinear response mainly including second harmonic generation and multiphoton photoluminescense in the microfiber-coupled plasmonic system. The nonlinear plasmonic is still a very young and active research field. Although the fabrication and microscopy technology already improved a lot in the past twenty years, the research about the nonlinear plasmonic is facing a lot of difficulties and challenges. The purpose of the proposed plasmon-fiber hybrid system, on one hand, is to overcome the near-zero of the second order nonlinear susceptibility due to the crystalline symmetry structure of metal and thus enhance the second harmonic generation, on the other hand, is to boost all the nonlinear response in metallic nanoparticles and thus provide the chance to investigate them with their behind physical mechanism.

In Chapter 2, we discussed the theoretical background of plasmonics, nonlinear optics and whispering gallery modes. We have seen that how a driving electric field excite the plasmon resonances, how the material responses in the nonlinear optical regime, how the whispering gallery modes are created and influenced by the parameters of the system. Meanwhile, we have learned that how the plasmon resonance can be detected by far-field optical measurements of the transmission, scattering and reflection. In particular, parameters of plasmonic particles such as the size, shape, material and surrounding environment leads to the different spectral position and shape of

the plasmon resonance features in the far-field regime. Thus, microspectroscopic measurements using the dark-field reflection setup is employed in this thesis to study behavior of the plasmonic systems.

Moreover, the theory background of nonlinear optics, especially second harmonic generation has been introduced. Based on the Lorenz used to predict the dielectric function of bulk materials, an anharmonic oscillation model is developed to describe the frequency-dependent nonlinear susceptibilities for n^{th} harmonic generation. More important is the conclusion that the SH intensity is proportional to the $4th$ power of the quality factor, which is of significance and guidance for the later system design.

Besides the plasmonic nanoparticles, the microfibers which operate the whispering gallery modes inside of cross section are introduced in Chapter 2. Some basic properties of whispering gallery modes and their excitation schemes have been discussed to lay a foundation of the following measurements.

Following these theory backgrounds, we have presented the experiment methods in Chapter 3. It was arranged as the order of the experiment processes, namely pulling the tapered fibers, synthesizing gold nanoparticles, preparing the coupled system and implementing the microspectroscopy. A home-made nonlinear microspectroscopy setup combing the laser pulse, spectrometer to the microscopy was introduced. Meanwhile, a unique side illuminating method was explained.

Based on the theory and experiment methods background information, the plasmon-fiber hybrid system was designed in Chapter 4. The linear scattering measurement results depicted a ultra-narrow linewidth resonance corresponding to a long life time due to the efficient coupling between the plasmon resonance of the gold nanoparticles and the whispering gallery modes of the microfibers. Meanwhile, we have discussed the detailed tailored resonance position and linewidth in the various hybrid systems.

An intuitive idea of sensing comes to mind when we consider the ultra-narrow linewidth of the system. Especially, the efficient

coupling with the whispering gallery modes can also take place to metallic nanoparticles of different material . For example, hydrogen sensing could be attempted by replacing gold nanoparticles with some gold@palladium ones.

As the topic of this thesis, nonlinear optical responses were investigated. They were introduced and separated into two parts, second harmonic generation and multiphoton photoluminescence. Based on the anharmonic oscillation model introduced in Chapter 2, an improved coupled anharmonic oscillation model has been utilized to check the measurement results of SH resonances and gotten a nice match. It was further proven by the measurement results of quality factor dependent SH intensity in Chapter 5. The SH resonance intensity is experimentally $3.5th$ power of the quality factor of the coupled system, closed to the $4th$ power predicted in the anharmonic model. This discovery told us that we can design high quality factor system to boost the SH process.

In fact, the origin of the second harmonic generation is always an intriguing question even though a lot of effort has been done to enhance the SHG intensity. The explicit origin of the shape effect in the nonlinear optical nanostructures has also been investigated both experimentally and theoretically. However, so far, the fundamental mechanism of those enhancements is still not clear. The pursuit to answer those questions faces difficulties at just changing one parameter of the plasmonic system with any other parameters remaining. Anther intriguing question is the symmetry role in nonlinear plasmonics. Some studies have already clearly show that breaking of the centrosymmetry does not induce an increasing SH intensity in coupled plasmonic nanoparticles, compared to the symmetric systems.[24, 38] Can we expand the symmetry considerations to the second harmonic generation in the sample with sub-wavelength size? Can the symmetry rules be applied and when not? All those questions for sure need be solved in the next years as the fabrication techniques and also the theoretical and simulation improve.

The multiphoton photoluminescence as an incoherent nonlinear process in the plasmonic nanoparticles is generally very weak. However, we have detected a broad MPPL background with big intensity in the nonlinear emission spectra of the hybrid systems. We have firstly investigate it in the fiber-coupled gold nanorods and determined the frequency-dependent nonlinear order. The interesting thing is that we have discovered different shapes of the MPPL spectra when we investigated the fiber-coupled nanobipyramids. It is still unclear how the geometry of plamsonic particles influences the MPPL process. An unexpected property of the MPPL contracts our attention that the MPPL shows different polarizations in different wavelength ranges. For example, it shows random polarization in the range of 450 nm-570 nm, while containing nearly linear polarization in the longer wavelength range (570 – 680 nm). In order to understand these differences, we have implemented an excitation power dependence measurement and determined the broad MPPL background in the spectra with two different process, 4PPL and 2PPL (largely enhanced by the localized surface plasmon resonance). Meanwhile, the different polarization properties are well explained by the band and crystalline structure of gold. Based on the proposed electron movement in the bands of gold, we have realized and presented the quenching effect of 4PPL by depositing homogeneous palladium shell onto the gold bipyramids in the coupled system.

Here, some questions remain. As mentioned, we have discovered different shapes of the MPPL spectra in fiber-coupled gold nanorods and nanobipyramids. What brings the difference is an interesting topic. Meanwhile, it must be a very challenge work. Similarly to the challenging topic of the second harmonic generation in plasmonic systems, a bunch of parameters mixed together in more and more complex researched systems. To reveal the origin of the nonlinearity in the plasmonic system become difficult but is very critical. Some simple plasmonic systems with enough intensity of MPPL are needed. Furthermore, different nonlinear responses generally take place at the same time. The relation between them, for example, the relation between the SHG and MPPL is also a noteworthy point.

In Chapter 5, we have presented another unique hybrid system, namely high Q doubly resonant plasmon-fiber cavities. It was started with the introduction of the design idea. Besides the realization of the high quality factor in the former singly resonant plasmon-fiber cavities introduced in Chapter 4, the new hybrid system is designed to fulfill the doubly resonant condition. Specifically speaking, a higher-order cavity mode is excited and matched to the SH wavelength position. It was the first time to realize a high quality factor and a doubly resonant system simultaneously. In this case, the fundamental mode and SH light circulate and interact dozens of times in a coherent fashion inside the micrfibers and gold nanoparticles and thus leads to giant SHG response.

This result is not only research about the typical samples, it can be applied to more plasmonic systems as a new concept of highly efficient nonlinear plasmonics. For example, metasurfaces with similar structures can be attempted for not only their second harmonic response but also other nonlinear processes. Meanwhile, the single metallic wire-shaped nanostructures which contain the plasmonic cavity modes and multipole plasmon modes simultanously, are also excellent candidate to achieve efficient nonlinear optical responses.[210] Furthermore, combining the plasmon modes to the nonliear whispering modes is also believed to be able to boost the nonlinear process.[211] Even though those experiments are not enough to recover the origin of the nonlinear plasmon optics, realization of the high quality factor and the doubly resonant condition is proven to be the right direction to boost the SH process.

A

POWER CALIBRATION OF THE SPECTROMETER

Since the measured SHG signals are quite weak, it is very challenging to directly measure the corresponding SHG power. In order to estimate the SHG power from the intensity signal recorded by the spectrometer, an indirect method was carried out to do the power calibration of the spectrometer.

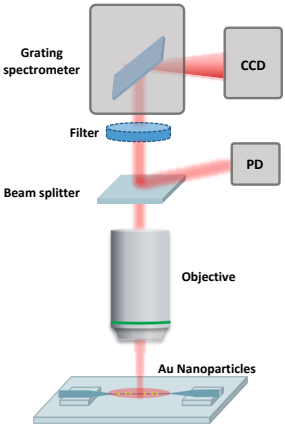

Figure A.1. Schematic overview of the power calibration of the spectrometer.

As shown in Figure A.1, two measurement devices are attached behind the microscope objective: a photodiode (PD) and a grating spectrometer with CCD camera (spec). A 45%/55% beamsplitter sends part of the light into the spectrometer and part into the photodiode. The light entering the spectrometer is attenuated by an ND filter (transmittance 10^{-3}). This is necessary because relatively high intensities must be used to get a meaningful signal in the PD, which would over-expose the spectrometer.

The goal is to be able to measure signals with a very low intensity at a different wavelength than the test signal (in this case: 430 nm vs. 860 nm) which can only be detected by the spectrometer, and convert these into a power value. The central question is thus: How can we calculate the power behind the objective from a spectral measurement? The difficulty here is that the sensitivity of the spectrometer as well as the photodiode are wavelength-dependent, as we will see in the following.

Photodiode

- Gain $G_{\mathrm{PD}}(\lambda)$ ($2.38e^5$ V/A for 50 dB; $0.75e^6$ V/A for 60 dB)

- Responsivity $R_{\mathrm{PD}}(\lambda)$ in A/W (from Thorlabs documentation) depicted in Figure A.2.

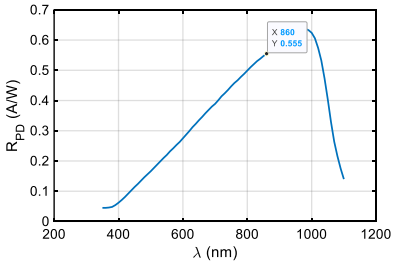

Figure A.2. The wavelength-dependent responsivity curve of the photodiode used to detect the power of the reference signal.

- Beamsplitter reflectivity 45%

Then, the efficiency factor can be presented as

$$\eta_{\mathrm{PD}} = R_{\mathrm{PD}}(\lambda) \cdot G_{PD}(\lambda) \cdot 0.45 \tag{A.1}$$

Spectrometer

- Grating efficiency $R_{\mathrm{grating}}(\lambda)$ (from Princetonin Instruments documentation) is depicted in Figure A.3.

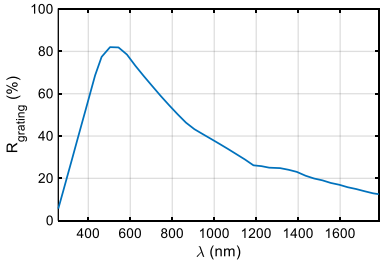

Figure A.3. The wavelength-dependent responsivity curve of the spectrometer used in this thesis.

- CCD camera efficiency $Q_{\mathrm{CCD}}(\lambda)$ (from Princeton Instruments documentation) is depicted in Figure A.4

Then, we can obtain the efficiency factor as

$$Q_{\mathrm{spec}}(\lambda) = R_{\mathrm{grating}}(\lambda) \cdot Q_{\mathrm{CCD}}(\lambda) \tag{A.2}$$

The resulting efficiencies including the efficiency factors of the CCD and spectrometer are depicted in Figure A.5.

Calculation of *power-to-counts* conversion factor

The spectrometer registers a number of counts per second in each wavelength channel. Thus the wavelength dependent intensity can be obtained in the following way:

$$I(\lambda) = P(\lambda) \cdot Q_{\mathrm{spec}}(\lambda) \cdot F, \tag{A.3}$$

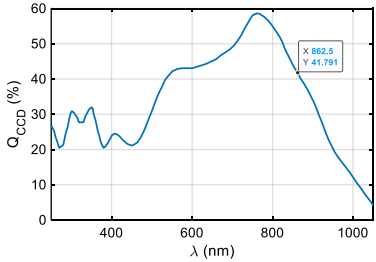

Figure A.4. The wavelength-dependent efficiency curve of Princements CCD camera connected to the grating spectrometer.

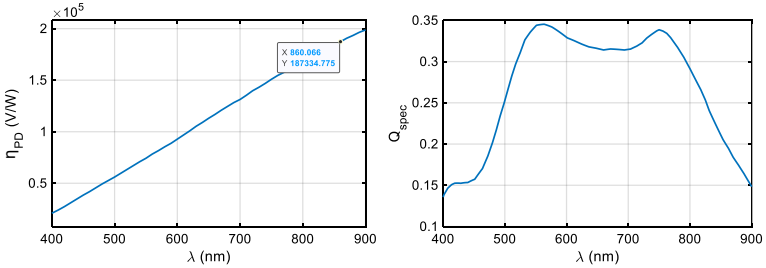

Figure A.5. Resulting efficiency factors for photodiode (left) and spectrometer (right).

Where F is the conversion factor that we are looking for. Here we assume it is a constant. $P(\lambda)$ represent the wavelength dependent power detected by the photodiode in Figure A.1.

The total voltage detected by the photodiode can be expressed as:

$$U_{\text{total}} = \int_{\lambda} P(\lambda) \cdot \eta_{\text{PD}}(\lambda) d\lambda, \tag{A.4}$$

The voltage contribution corresponding to the counts in each wavelength channel can be written as:

$$U(\lambda) = P(\lambda) \cdot \eta_{\text{PD}}(\lambda), \tag{A.5}$$

But we only know U_{total}, not U_λ. However, we can rewrite Equation A.3 as follows:

$$P(\lambda) = \frac{I_{\text{spec}}(\lambda)}{Q_{\text{spec}}(\lambda)} \cdot \frac{1}{F}, \tag{A.6}$$

And insert it in Equation A.4:

$$U_{\text{total}} = \int_\lambda I_{\text{spec}}(\lambda) \cdot \frac{\eta_{\text{PD}}(\lambda)}{Q_{\text{spec}}(\lambda)} \frac{1}{F} d\lambda, \tag{A.7}$$

So that the conversion factor F can be expressed as:

$$F = \frac{\int_\lambda I_{\text{spec}}(\lambda) \cdot \frac{\eta_{\text{PD}}(\lambda)}{Q_{\text{spec}}(\lambda)} d\lambda}{U_{\text{total}}} \tag{A.8}$$

Or, since we are dealing with discrete wavelength channels, we can also rewrite it as following:

$$F = \frac{\sum I_{\text{spec}}(\lambda) \cdot \frac{\eta}{Q_{\text{spec}}(\lambda)}}{U_{\text{total}}}, \tag{A.9}$$

This can be done using any spectral measurement for which a power measurement has been done as well. Here, we use the fundamental mode scattering signal. Note that the signal must be obtained by integrating over the CCD camera strips, not by averaging.

If the conversion factor F is known, any other measured spectrum $I(\lambda)$ can be converted to a power value via the known shape of $Q_{\text{spec}}(\lambda)$:

$$P_{\text{total}} = \sum \frac{I_{\text{spec}}(\lambda)}{Q_{\text{spec}}(\lambda)} \cdot F, \tag{A.10}$$

Calculation of F from real measurement data:

- Measured spectrum of the fundamental mode (scattered from the excitation laser) subtracting background is displayed in Figure A.6 according to

$$I_{\text{spec}}(\lambda) = \frac{I_{\text{measured}}(\lambda)}{t_{\text{int}} \cdot T_{\text{BS}} \cdot T_{\text{filter}}} \tag{A.11}$$

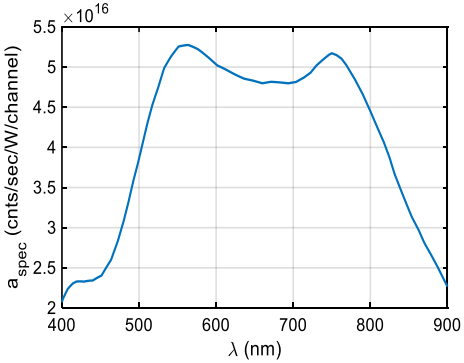

FIGURE A.6. Measured spectrum of the fundamental mode with the background subtraction

where t_{int} is the integration time, T_{BS} is the beam splitter transmittance of 55% and T_{filter} is filter transmittance of 10^{-3}.

- PD voltage: 275 mV = 0.275 V

- Gain setting 60dB

- Laser wavelength 860 nm (SHG wavelength: 430 nm)

Total power incident on PD (estimated using a_{PD} at 860 nm) is obtained:

$$P_{\text{PD}} = \frac{0.275}{1.87 \times 10^5} = 1.47 \times 10^{-6} W,$$

The conversion factor F is obtained using constant a_{PD} and Q_{spec} values:

$$\begin{aligned} F &= \frac{I_{\text{total}}/Q_{\text{spec}}}{U_{\text{PD}}/\eta_{\text{PD}}} = \frac{I_{\text{total}} \cdot \eta_{\text{PD}}}{U_{\text{PD}} \cdot Q_{\text{spec}}} \\ &= \frac{4.5 \times 10^{10} \times 1.87 \times 10^5}{0.275 \times 0.198} \\ &= 1.55 \times 10^{17} cts \cdot s^{-1} \cdot W^{-1}, \end{aligned} \tag{A.12}$$

Instead of the constand a_{PD} and Q_{spec} values, the conversion factor F also can be calculated using wavelength-dependent values according to Equation A.9:

$$\begin{aligned} F &= \frac{\sum I_{\mathrm{spec}}(\lambda) \cdot \frac{\eta_{\mathrm{PD}}(\lambda)}{Q_{\mathrm{spec}}(\lambda)} d\lambda}{U_{\mathrm{total}}} \\ &= 1.53 \times 10^{17} cts \cdot s^{-1} \cdot W^{-1}, \end{aligned} \tag{A.13}$$

Using the last equation for F, we can plot $a_{\mathrm{spec}}(\lambda) = Q_{\mathrm{spec}}(\lambda) \cdot F$ as displayed in Figure A.7.

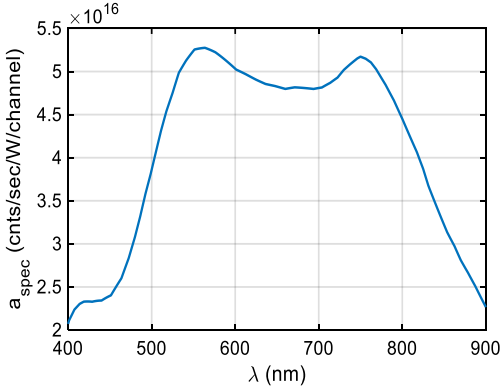

Figure A.7. Wavelength dependent efficiency factor of the spectrometer

Now, for any given spectrum $I(\lambda)$, the corresponding power can be calculated as $P = \sum \frac{I(\lambda)}{a_{\mathrm{spec}}(\lambda)}$.

LIST OF FIGURES

LIST OF TABLES

LIST OF ACRONYMS

$\triangle\lambda$	linewidth
2PPL	two photon (induced) photoluminescence
4PPL	four photon (induced) photoluminescence
AA	L-ascorbic acid
Ag	silver
AgNO	silver nitrate
Au	gold
AuNP	gold nanoparticle
CCD	charge-coupled device
CTAB	cetyltrimethylammonium bromide
CTAC	cetyltrimethylammonium chloride
DFG	difference frequency generation
DI	deionized
EDX	Energy-dispersive X-ray
EELS	electron energy-loss spectroscopy
EIA	electromagnetically-induced-absorption
EIT	electromagnetically-induced-transparency
EM	electron-magnetic
FDTD	finite-difference time-domain
FEM	finite element method
FSR	free spectral range
FWHM	full width at half maximum
H_2O_2	hydrogen peroxide solution
$HAuCl_4{\cdot}3H_2O$	chloroauric acid trihydrate
HQ	hydroquinone
H_2PdCl_4	tetrachloropalladic acid

LSPR	localized surface plasmon resonance
MPPL	multiphoton photoluminescence
NA	numerical aperture
NBP	nanobipyramid
$NH{\cdot}H_2O$	ammonia solution
$NaBH_4$	sodium borohydride
OR	optical rectification
PD	photodiode
Pd	palladium
$PdCl_2$	palladium dichloride
Q	quality
SEM	scanning electron microscope
SFG	sum frequency generation
SH	second harmonic
SHG	second harmonic generation
SMF	single mode fibers
SNOM	scanning near-field optical microscopy
TE	transverse electric
TEM	transmission electron microscope
THG	third harmonic generation
TM	transverse magnetic
TSC	trisodium citrate
TSP	transverse surface plasmon
WGMs	whispering gallery modes

BIBLIOGRAPHY

[1] T. H. Maiman: *Stimulated optical radiation in Ruby.* Nature **187**, 493–494 (1960).
DOI 10.1038/187493a0, cit. on p. 1.

[2] W. Kaiser and C. G. Garrett: *Two-photon excitation in CaF2: Eu2+.* Physical Review Letters **7**, 229–231 (1961).
DOI 10.1103/PhysRevLett.7.229, cit. on pp. 1, 2.

[3] S. Y. Chen, A. Maksimchuk, and D. Umstadter: *Experimental observation of relativistic nonlinear Thomson scattering.* Nature **396**, 653–655 (1998).
DOI 10.1038/25303, cit. on p. 1.

[4] M. Soljacic, M. Segev, T. Coskun, D. N. Christodoulides, and A. Vishwanath: *Modulation instability of incoherent beams in noninstantaneous nonlinear media.* Physical Review Letters **84**, 467–470 (2000).
DOI 10.1103/PhysRevLett.84.467, cit. on p. 1.

[5] C. Thaury, F. Quéré, J. P. Geindre, A. Levy, T. Ceccotti, P. Monot, M. Bougeard, F. Réau, P. D'Oliveira, P. Audebert, R. Marjoribanks, and P. Martin: *Plasma mirrors for ultrahigh-intensity optics.* Nature Physics **3**, 424–429 (2007).
DOI 10.1038/nphys595, cit. on p. 1.

[6] R. W. Boyd and B. R. Masters: *Nonlinear Optics, Third Edition.* Journal of Biomedical Optics **14**, 029902 (2009).
DOI 10.1117/1.3115345, cit. on pp. 1, 25, 26.

[7] H. J. Simon, D. E. Mitchell, and J. G. Watson: *Optical second-harmonic generation with surface plasmons in silver films.* Physical Review Letters **33**, 1531–1534 (1974).
DOI 10.1103/PhysRevLett.33.1531, cit. on p. 2.

[8] S. Linden, J. Kuhl, and H. Giessen: *Controlling the Interaction between Light and Gold Nanoparticles: Selective Suppression of Extinction*. Physical Review Letters **86**, 4688–4691 (2001). DOI 10.1103/PhysRevLett.86.4688, cit. on p. 2.

[9] W. L. Barnes, A. Dereux, and T. W. Ebbesen: *Surface plasmon subwavelength optics*. Nature **424**, 824–830 (2003). DOI 10.1038/nature01937, cit. on p. 2.

[10] S. A. Maier: *Plasmonics: Fundamentlas and Applications*, Springer, 2007. ISBN 9780387378251, cit. on pp. 2, 8, 70.

[11] L. Martín-Moreno, F. J. García-Vidal, H. J. Lezec, K. M. Pellerin, T. Thio, J. B. Pendry, and T. W. Ebbesen: *Theory of extraordinary optical transmission through subwavelength hole arrays*. Physical Review Letters **86**, 1114–1117 (2001). DOI 10.1103/PhysRevLett.86.1114, cit. on p. 2.

[12] K. J. Koerkamp, S. Enoch, F. B. Segerink, N. F. Van Hulst, and L. Kuipers: *Strong influence of hole shape on extraordinary transmission through periodic arrays of subwavelength holes*. Physical Review Letters **92**, 18–21 (2004). DOI 10.1103/PhysRevLett.92.183901, cit. on p. 2.

[13] K. L. Van Der Molen, K. J. Klein Koerkamp, S. Enoch, F. B. Segerink, N. F. Van Hulst, and L. Kuipers: *Role of shape and localized resonances in extraordinary transmission through periodic arrays of subwavelength holes: Experiment and theory*. Physical Review B - Condensed Matter and Materials Physics **72**, 1–9 (2005). DOI 10.1103/PhysRevB.72.045421, cit. on p. 2.

[14] C. Genet and T. W. Ebbesen: *Light in tiny holes*. Nanoscience and Technology: A Collection of Reviews from Nature Journals **445**, 205–212 (2009). DOI 10.1142/9789814287005_0021, cit. on p. 2.

[15] J. Nappa, I. Russier-Antoine, E. Benichou, C. Jonin, and P. F. Brevet: *Second harmonic generation from small gold metallic particles: From the dipolar to the quadrupolar response*. Journal of Chemical Physics **125** (2006). DOI 10.1063/1.2375095, cit. on p. 2.

[16] J. Butet, G. Bachelier, I. Russier-Antoine, C. Jonin, E. Benichou, and P. F. Brevet: *Interference between selected dipoles and octupoles in the optical second-harmonic generation from spherical gold nanoparticles*. Physical Review Letters **105**, 1–4 (2010). DOI 10.1103/PhysRevLett.105.077401, cit. on p. 2.

[17] A. Nahata, R. A. Linke, T. Ishi, and K. Ohashi: *Enhanced nonlinear optical conversion from a periodically nanostructured metal film*. Optics Letters **28**, 423 (2003). DOI 10.1364/ol.28.000423, cit. on p. 2.

[18] M. W. Klein, C. Enkrich, M. Wegener, and S. Linden: *Second-harmonic generation from magnetic metamaterials*. Science **313**, 502–504 (2006). DOI 10.1126/science.1129198, cit. on p. 2.

[19] S. Linden, F. B. Niesler, J. Förstner, Y. Grynko, T. Meier, and M. Wegener: *Collective effects in second-harmonic generation from split-ring-resonator arrays*. Physical Review Letters **109**, 1–5 (2012). DOI 10.1103/PhysRevLett.109.015502, cit. on pp. 2, 115.

[20] S. Lamprecht, A. Leitner, and F. R. Aussenegg: *Femtosecond decay-time measurement of electron-plasma oscillation in nanolithographically designed silver particles*. Applied Physics B: Lasers and Optics **64**, 269–272 (1997). DOI 10.1007/s003400050174, cit. on p. 2.

[21] H. Husu, R. Siikanen, J. Mäkitalo, J. Lehtolahti, J. Laukkanen, M. Kuittinen, and M. Kauranen: *Metamaterials with tailored nonlinear optical response*. Nano Letters **12**, 673–677 (2012). DOI 10.1021/nl203524k, cit. on p. 2.

[22] B. K. Canfield, H. Husu, J. Laukkanen, B. Bai, M. Kuittinen, J. Turunen, and M. Kauranen: *Local Field Asymmetry Drives Second-Harmonic Generation in Noncentrosymmetric Nanodimers.* Nano Letters **7**, 1251–1255 (2007). DOI 10.1021/nl0701253, cit. on p. 2.

[23] K. Thyagarajan, S. Rivier, A. Lovera, and O. J. Martin: *Enhanced second-harmonic generation from double resonant plasmonic antennae.* Optics Express **20**, 12860 (2012). DOI 10.1364/oe.20.012860, cit. on pp. 2, 110.

[24] J. Butet, S. Dutta-Gupta, and O. J. Martin: *Surface second-harmonic generation from coupled spherical plasmonic nanoparticles: Eigenmode analysis and symmetry properties.* Physical Review B - Condensed Matter and Materials Physics **89**, 1–10 (2014). DOI 10.1103/PhysRevB.89.245449, cit. on pp. 2, 3, 115, 133.

[25] B. Metzger, L. Gui, J. Fuchs, D. Floess, M. Hentschel, and H. Giessen: *Strong Enhancement of Second Harmonic Emission by Plasmonic Resonances at the Second Harmonic Wavelength.* Nano Letters **15**, 3917–3922 (2015). DOI 10.1021/acs.nanolett.5b00747, cit. on p. 2.

[26] M. Celebrano, X. Wu, M. Baselli, S. Großmann, P. Biagioni, A. Locatelli, C. De Angelis, G. Cerullo, R. Osellame, B. Hecht, L. Duò, F. Ciccacci, and M. Finazzi: *Mode matching in multiresonant plasmonic nanoantennas for enhanced second harmonic generation.* Nature Nanotechnology **10**, 412–417 (2015). DOI 10.1038/nnano.2015.69, cit. on pp. 2, 110, 127.

[27] H. Linnenbank, Y. Grynko, J. Förstner, and S. Linden: *Second harmonic generation spectroscopy on hybrid plasmonic/dielectric nanoantennas.* Light: Science & Applications **5**, e16013–e16013 (2016). DOI 10.1038/lsa.2016.13, cit. on p. 2.

[28] S. Liu, M. B. Sinclair, S. Saravi, G. A. Keeler, Y. Yang, J. Reno, G. M. Peake, F. Setzpfandt, I. Staude, T. Pertsch, and I. Brener: *Resonantly Enhanced Second-Harmonic Generation Using III-V Semiconductor All-Dielectric Metasurfaces.* Nano Letters **16**, 5426–5432 (2016).
DOI 10.1021/acs.nanolett.6b01816, cit. on pp. 2, 127.

[29] L. Ghirardini, L. Carletti, V. Gili, G. Pellegrini, L. Duò, M. Finazzi, D. Rocco, A. Locatelli, C. De Angelis, I. Favero, M. Ravaro, G. Leo, A. Lemaître, and M. Celebrano: *Polarization properties of second-harmonic generation in AlGaAs optical nanoantennas.* Optics Letters **42**, 559 (2017).
DOI 10.1364/ol.42.000559, cit. on pp. 2, 110.

[30] P. P. Vabishchevich, S. Liu, M. B. Sinclair, G. A. Keeler, G. M. Peake, and I. Brener: *Enhanced Second-Harmonic Generation Using Broken Symmetry III-V Semiconductor Fano Metasurfaces.* ACS Photonics **5**, 1685–1690 (2018).
DOI 10.1021/acsphotonics.7b01478, cit. on p. 2.

[31] V. K. Valev, A. V. Silhanek, N. Verellen, W. Gillijns, P. Van Dorpe, O. A. Aktsipetrov, G. A. Vandenbosch, V. V. Moshchalkov, and T. Verbiest: *Asymmetric optical second-harmonic generation from chiral G-shaped gold nanostructures.* Physical Review Letters **104**, 2–5 (2010).
DOI 10.1103/PhysRevLett.104.127401, cit. on pp. 2, 110.

[32] A. Belardini, M. C. Larciprete, M. Centini, E. Fazio, C. Sibilia, D. Chiappe, C. Martella, A. Toma, M. Giordano, and F. Buatier De Mongeot: *Circular dichroism in the optical second-harmonic emission of curved gold metal nanowires.* Physical Review Letters **107**, 1–5 (2011).
DOI 10.1103/PhysRevLett.107.257401, cit. on pp. 2, 110.

[33] P. Genevet, J. P. Tetienne, E. Gatzogiannis, R. Blanchard, M. A. Kats, M. O. Scully, and F. Capasso: *Large enhancement of nonlinear optical phenomena by plasmonic nanocavity gratings*. Nano Letters **10**, 4880–4883 (2010).
DOI 10.1021/nl102747v, cit. on pp. 2, 110, 127.

[34] K. Thyagarajan, J. Butet, and O. J. Martin: *Augmenting second harmonic generation using fano resonances in plasmonic systems*. Nano Letters **13**, 1847–1851 (2013).
DOI 10.1021/nl400636z, cit. on p. 2.

[35] H. Tuovinen, M. Kauranen, K. Jefimovs, P. Vahimaa, T. Vallius, J. Turunen, N. V. Tkachenko, and H. Lemmetyinen: *Linear and second-order nonlinear optical properties of arrays of noncentrosymmetric gold nanoparticles*. Journal of Nonlinear Optical Physics and Materials **11**, 421–432 (2002).
DOI 10.1142/S0218863502001103, cit. on pp. 3, 115.

[36] A. Lesuffleur, L. K. Kumar, and R. Gordon: *Apex-enhanced second-harmonic generation by using double-hole arrays in a gold film*. Physical Review B - Condensed Matter and Materials Physics **75**, 1–6 (2007).
DOI 10.1103/PhysRevB.75.045423, cit. on pp. 3, 115.

[37] B. L. Wang, R. Wang, R. J. Liu, X. H. Lu, J. Zhao, and Z. Y. Li: *Origin of shape resonance in second-harmonic generation from metallic nanohole arrays*. Scientific Reports **3**, 1–8 (2013).
DOI 10.1038/srep02358, cit. on pp. 3, 115.

[38] J. Berthelot, G. Bachelier, M. Song, P. Rai, G. Colas des Francs, A. Dereux, and A. Bouhelier: *Silencing and enhancement of second-harmonic generation in optical gap antennas*. Optics Express **20**, 10498 (2012).
DOI 10.1364/oe.20.010498, cit. on pp. 3, 115, 133.

[39] F. X. Wang, F. J. Rodríguez, W. M. Albers, R. Ahorinta, J. E. Sipe, and M. Kauranen: *Surface and bulk contributions to the second-order nonlinear optical response of a gold film.* Physical Review B - Condensed Matter and Materials Physics **80**, 4–7 (2009).
DOI 10.1103/PhysRevB.80.233402, cit. on pp. 3, 115.

[40] Y. Zeng, W. Hoyer, J. Liu, S. W. Koch, and J. V. Moloney: *Classical theory for second-harmonic generation from metallic nanoparticles.* Physical Review B - Condensed Matter and Materials Physics **79** (2009).
DOI 10.1103/PhysRevB.79.235109, cit. on pp. 3, 29, 115.

[41] A. Benedetti, M. Centini, M. Bertolotti, and C. Sibilia: *Second harmonic generation from 3D nanoantennas: on the surface and bulk contributions by far-field pattern analysis.* Optics Express **19**, 26752 (2011).
DOI 10.1364/oe.19.026752, cit. on p. 3.

[42] K. O'Brien, H. Suchowski, J. Rho, A. Salandrino, B. Kante, X. Yin, and X. Zhang: *Predicting nonlinear properties of metamaterials from the linear response.* Nature Materials **14**, 379–383 (2015).
DOI 10.1038/nmat4214, cit. on pp. 3, 115.

[43] E. Kim, F. Wang, W. Wu, Z. Yu, and Y. R. Shen: *Nonlinear optical spectroscopy of photonic metamaterials.* Physical Review B - Condensed Matter and Materials Physics **78**, 3–4 (2008).
DOI 10.1103/PhysRevB.78.113102, cit. on pp. 3, 115.

[44] M. Hentschel, T. Utikal, H. Giessen, and M. Lippitz: *Quantitative modeling of the third harmonic emission spectrum of plasmonic nanoantennas.* Nano Letters **12**, 3778–3782 (2012).
DOI 10.1021/nl301686x, cit. on pp. 3, 68, 115.

[45] T. Hanke, J. Cesar, V. Knittel, A. Trügler, U. Hohenester, A. Leitenstorfer, and R. Bratschitsch: *Tailoring spatiotemporal light confinement in single plasmonic nanoantennas.* Nano Letters **12**, 992–996 (2012).
DOI 10.1021/nl2041047, cit. on p. 3.

[46] B. Metzger, M. Hentschel, M. Lippitz, and H. Giessen: *Third-harmonic spectroscopy and modeling of the nonlinear response of plasmonic nanoantennas.* Optics Letters **37**, 4741 (2012).
DOI 10.1364/ol.37.004741, cit. on pp. 3, 68.

[47] Q. Ai, L. Gui, D. Paone, B. Metzger, M. Mayer, K. Weber, A. Fery, and H. Giessen: *Ultranarrow Second-Harmonic Resonances in Hybrid Plasmon-Fiber Cavities.* Nano Letters **18**, 5576–5582 (2018).
DOI 10.1021/acs.nanolett.8b02005, cit. on pp. 3, 115.

[48] L. Novotny and B. Hecht: *Principles of Nano-Optics*, Cambridge University Press, 2012.
ISBN 9780511794193, cit. on p. 8.

[49] C.F. Bohren and D.R. Huffman: *Absorption and scattering of light by small particles*, 1998.
ISBN 978-0-471-29340-8, cit. on pp. 8, 22.

[50] A. Vial, A.-S. Grimault, D. Macías, D. Barchiesi, and M. L. de la Chapelle: *Improved analytical fit of gold dispersion: Application to the modeling of extinction spectra with a finite-difference time-domain method.* Physical Review B **71**, 085416 (2005).
DOI 10.1103/PhysRevB.71.085416, cit. on p. 16.

[51] G. Mie: *Beiträge zur Optik trüber Medien, speziell kolloidaler Metallösungen.* Annalen der Physik **330**, 377–445 (1908).
DOI 10.1002/andp.19083300302, cit. on p. 22.

[52] R. Gans: *Über die Form ultramikroskopischer Goldteilchen.* Annalen der Physik **342**, 881–900 (1912).
DOI 10.1002/andp.19123420503, cit. on p. 22.

[53] C. Noguez: *Surface plasmons on metal nanoparticles: The influence of shape and physical environment*. Journal of Physical Chemistry C **111**, 3606–3619 (2007).
DOI 10.1021/jp066539m, cit. on p. 22.

[54] P. A. Franken, A. E. Hill, C. W. Peters, and G. Weinreich: *Generation of optical harmonics*. Physical Review Letters **7**, 118–119 (1961).
DOI 10.1103/PhysRevLett.7.118, cit. on p. 27.

[55] V. Petrov: *Frequency down-conversion of solid-state laser sources to the mid-infrared spectral range using non-oxide nonlinear crystals*. Progress in Quantum Electronics **42**, 1–106 (2015).
DOI 10.1016/j.pquantelec.2015.04.001, cit. on p. 29.

[56] R. L. Sutherland: *Handbook of Nonlinear Optics*, vol. 3, Marcel Dekker, Inc., 1997.
ISBN 0824742435, cit. on p. 29.

[57] T. Heinz: *Second-Order Nonlinear Optical Effects at Surfaces and Interfaces*, vol. 7, Elsevier Science Publishers B.V., 1991.
ISBN 978-0-444-88359-9, cit. on p. 30.

[58] P. Guyot-Sionnest and Y. R. Shen: *Bulk contribution in surface second-harmonic generation*. Physical Review B **38**, 7985–7989 (1988).
DOI 10.1103/PhysRevB.38.7985, cit. on p. 31.

[59] J. Zuloaga and P. Nordlander: *On the energy shift between near-field and far-field peak intensities in localized plasmon systems*. Nano Letters **11**, 1280–1283 (2011).
DOI 10.1021/nl1043242, cit. on p. 35.

[60] D. Hall and P. Jackson: *The Physics and Technology of Laser Resonators*. The Physics and Technology of Laser Resonators (2020).
DOI 10.1201/9781003069508, cit. on p. 37.

[61] N Hodgson and H Weber: *Optical resonators-Fundamentals, advanced concepts and applications*, London: Springer-Verlag, 1997.
ISBN 978-1-4471-3595-1, cit. on p. 37.

[62] B. Little, S. Chu, H. Haus, J. Foresi, and J.-P. Laine: *Microring resonator channel dropping filters*. Journal of Lightwave Technology **15**, 998–1005 (1997).
DOI 10.1109/50.588673, cit. on p. 37.

[63] N. Hodgson, H. Weber, F. H. K. V. Lotsch, E. B. T. Asakura, T Kamiya, B Monemar, H Venghaus, H Weinfurter, and W. T. Rhodes: *Laser Resonators and Beam Propagation. Fundamentals, Advanced Concepts, Applications*, Springer, 2005.
ISBN 0-387-40078-8, cit. on p. 37.

[64] X. Zhang, Q. T. Cao, Z. Wang, Y. xi Liu, C. W. Qiu, L. Yang, Q. Gong, and Y. F. Xiao: *Symmetry-breaking-induced nonlinear optics at a microcavity surface*. Nature Photonics **13**, 21–24 (2019).
DOI 10.1038/s41566-018-0297-y, cit. on p. 37.

[65] T. Compendium: *Integrated Ring Resonators*, Springer, 2007.
ISBN 9783540687863, cit. on p. 37.

[66] L. Rayleigh: *CXII. The problem of the whispering gallery*. The London, Edinburgh, and Dublin Philosophical Magazine and Journal of Science **20**, 1001–1004 (1910).
DOI 10.1080/14786441008636993, cit. on p. 38.

[67] M. J. Deen and P. K. Basu: *Optical Processes*. Silicon Photonics, 69–108 (2012).
DOI 10.1002/9781119945161.ch4, cit. on p. 38.

[68] Q. J. Wang, C. Yan, N. Yu, J. Unterhinninghofen, J. Wiersig, C. Pflügl, L. Diehl, T. Edamura, M. Yamanishi, H. Kan, and F. Capasso: *Whispering-gallery mode resonators for highly unidirectional laser action*. Proceedings of the National Academy of Sciences of the United States of America **107**, 22407–22412 (2010).
DOI 10.1073/pnas.1015386107, cit. on p. 38.

[69] M. Sumetsky: *Lasing microbottles*. Light: Science and Applications **6**, 4–6 (2017).
DOI 10.1038/lsa.2017.102, cit. on p. 38.

[70] S. M. Spillane: *Fiber-coupled Ultra-high-Q Microresonators for Nonlinear and Quantum Optics Thesis by*. PhD Thesis **2004**, 143 (2004).
DOI 10.7907/MKYH-WV47, cit. on p. 38.

[71] M. A. Schmidt, D. Y. Lei, L. Wondraczek, V. Nazabal, and S. A. Maier: *Hybrid nanoparticle–microcavity-based plasmonic nanosensors with improved detection resolution and extended remote-sensing ability*. Nature Communications **3**, 1108 (2012).
DOI 10.1038/ncomms2109, cit. on p. 38.

[72] J. Wang, T. Zhan, G. Huang, P. K. Chu, and Y. Mei: *Optical microcavities with tubular geometry: Properties and applications*. Laser and Photonics Reviews **8**, 521–547 (2014).
DOI 10.1002/lpor.201300040, cit. on p. 38.

[73] W. Pongruengkiat and S. Pechprasarn: *Whispering-gallery mode resonators for detecting cancer*. Sensors (Switzerland) **17** (2017).
DOI 10.3390/s17092095, cit. on p. 38.

[74] Y. nan Zhang, T. Zhou, B. Han, A. Zhang, and Y. Zhao: *Optical bio-chemical sensors based on whispering gallery mode resonators*. Nanoscale **10**, 13832–13856 (2018).
DOI 10.1039/c8nr03709d, cit. on p. 38.

[75] X. Jiang, A. J. Qavi, S. H. Huang, and L. Yang: *Whispering-Gallery Sensors*. Matter **3**, 371–392 (2020).
DOI 10.1016/j.matt.2020.07.008, cit. on p. 38.

[76] J. Ward and O. Benson: *WGM microresonators: Sensing, lasing and fundamental optics with microspheres*. Laser and Photonics Reviews **5**, 553–570 (2011).
DOI 10.1002/lpor.201000025, cit. on p. 39.

[77] M. D. Baaske and F. Vollmer: *Optical observation of single atomic ions interacting with plasmonic nanorods in aqueous solution*. Nature Photonics **10**, 733–739 (2016).
DOI 10.1038/nphoton.2016.177, cit. on p. 39.

[78] A. Chiasera, Y. Dumeige, P. Féron, M. Ferrari, Y. Jestin, G. N. Conti, S. Pelli, S. Soria, and G. C. Righini: *Spherical whispering-gallery-mode microresonators*. Laser and Photonics Reviews **4**, 457–482 (2010).
DOI 10.1002/lpor.200910016, cit. on p. 39.

[79] G. Kakarantzas, T. E. Dimmick, T. A. Birks, R. Le Roux, and P. S. J. Russell: *Miniature all-fiber devices based on CO2 laser microstructuring of tapered fibers*. Optics Letters **26**, 1137 (2001).
DOI 10.1364/OL.26.001137, cit. on p. 39.

[80] D. K. Armani, T. J. Kippenberg, S. M. Spillane, and K. J. Vahala: *Ultra-high-Q toroid microcavity on a chip*. Nature **421**, 925–928 (2003).
DOI 10.1038/nature01371, cit. on pp. 39, 45.

[81] G. Senthil Murugan, J. S. Wilkinson, and M. N. Zervas: *Optical excitation and probing of bottle microresonators*. AIP Conference Proceedings **1288**, 22–25 (2010).
DOI 10.1063/1.3521362, cit. on p. 39.

[82] M. Sumetsky, Y. Dulashko, and R. S. Windeler: *Optical microbubble resonator*. Optics Letters **35**, 898 (2010).
DOI 10.1364/ol.35.000898, cit. on pp. 39, 45.

[83] M. MICHIHATA, B. CHU, Z. ZHAO, K. HAYASHI, K. TAKAMASU, and S. TAKAHASHI: *Diameter Measurement of a Microsphere Based on Whispering Gallery Mode Resonance*. Journal of the Japan Society for Precision Engineering **84**, 77–84 (2018).
DOI 10.2493/jjspe.84.77, cit. on p. 40.

[84] C. C. Lam, P. T. Leung, and K. Young: *Explicit asymptotic formulas for the positions, widths, and strengths of resonances in Mie scattering*. Journal of the Optical Society of America B **9**, 1585 (1992).
DOI 10.1364/josab.9.001585, cit. on pp. 40, 41.

[85] V. B. Braginsky, M. L. Gorodetsky, and V. S. Ilchenko: *Quality-factor and nonlinear properties of optical whispering-gallery modes*. Physics Letters A **137**, 393–397 (1989).
DOI 10.1016/0375-9601(89)90912-2, cit. on pp. 40, 43, 48.

[86] M. L. Gorodetsky, A. A. Savchenkov, and V. S. Ilchenko: *Ultimate Q of optical microsphere resonators*. Proceedings of SPIE - The International Society for Optical Engineering **2799**, 389–391 (1996).
DOI 10.1364/ol.21.000453, cit. on p. 45.

[87] S. Soria, S. Berneschi, M. Brenci, F. Cosi, G. N. Conti, S. Pelli, and G. C. Righini: *Optical microspherical resonators for biomedical sensing*. Sensors **11**, 785–805 (2011).
DOI 10.3390/s110100785, cit. on pp. 45, 47.

[88] P. Wang, Y. Wang, Z. Yang, X. Guo, X. Lin, X. C. Yu, Y. F. Xiao, W. Fang, L. Zhang, G. Lu, Q. Gong, and L. Tong: *Single-Band 2-nm-Line-Width Plasmon Resonance in a Strongly Coupled Au Nanorod*. Nano Letters **15**, 7581–7586 (2015).
DOI 10.1021/acs.nanolett.5b03330, cit. on pp. 45, 86, 114, 116.

[89] M. Kuwata-Gonokami and K. Takeda: *Polymer whispering gallery mode lasers*. Optical Materials **9**, 12–17 (1998).
DOI 10.1016/S0925-3467(97)00160-2, cit. on p. 46.

[90] V. S. Ilchenko, A. M. Bennett, P. Santini, A. A. Savchenkov, A. B. Matsko, and L. Maleki: *Whispering gallery mode diamond resonator*. Optics Letters **38**, 4320 (2013).
DOI 10.1364/ol.38.004320, cit. on p. 46.

[91] X. Peng, F. Song, S. Jiang, N. Peyghambarian, M. Kuwata-Gonokami, and L. Xu: *Fiber-taper-coupled L-band Er 3+-doped tellurite glass microsphere laser*. Applied Physics Letters **82**, 1497–1499 (2003).
DOI 10.1063/1.1559653, cit. on p. 47.

[92] G. C. Righini, Y. Dumeige, P. Féron, M. Ferrari, G. N. Conti, D. Ristic, and S. Soria: *Whispering Gallery Mode microresonators: Fundamentals and applications*. Rivista del Nuovo Cimento **34**, 435–488 (2011).
DOI 10.1393/ncr/i2011-10067-2, cit. on p. 47.

[93] S. Yang, Y. Wang, and H. D. Sun: *Advances and Prospects for Whispering Gallery Mode Microcavities*. Advanced Optical Materials **3**, 1136–1162 (2015).
DOI 10.1002/adom.201500232, cit. on p. 47.

[94] L. Bica: *Formation of glass microspheres with rotating electrical arc*. Materials Science and Engineering B: Solid-State Materials for Advanced Technology **77**, 210–212 (2000).
DOI 10.1016/S0921-5107(00)00483-9, cit. on p. 47.

[95] G. Nunzi Conti, A. Chiasera, L. Ghisa, S. Berneschi, M. Brenci, Y. Dumeige, S. Pelli, S. Sebastiani, P. Feron, M. Ferrari, and G. Righini: *Spectroscopic and lasing properties of Er3+-doped glass microspheres*. Journal of Non-Crystalline Solids **352**, 2360–2363 (2006).
DOI 10.1016/j.jnoncrysol.2006.01.089, cit. on p. 47.

[96] M. L. Gorodetsky and V. S. Ilchenko: *Optical microsphere resonators: optimal coupling to high-Q whispering-gallery modes*. Journal of the Optical Society of America B **16**, 147 (1999).
DOI 10.1364/josab.16.000147, cit. on p. 48.

[97] V. S. Ilchenko, X. S. Yao, and L. Maleki: *Pigtailing the high-Q microsphere cavity: a simple fiber coupler for optical whispering-gallery modes*. Optics Letters **24**, 723 (1999).
DOI 10.1364/ol.24.000723, cit. on p. 48.

[98] J. C. Knight, G. Cheung, F. Jacques, and T. A. Birks: *Phase-matched excitation of whispering-gallery-mode resonances by a fiber taper*. Optics Letters **22**, 1129 (1997).
DOI 10.1364/ol.22.001129, cit. on p. 48.

[99] M. Cai, O. Painter, and K. J. Vahala: *Observation of Critical Coupling in a Fiber Taper to a Silica-Microsphere Whispering-Gallery Mode System*. Physical Review Letters **85**, 74–77 (2000).
DOI 10.1103/PhysRevLett.85.74, cit. on p. 48.

[100] C. V. Boys: *On the production, properties, and some suggested uses of the finest threads*. Proceedings of the Physical Society of London **9**, 8–19 (1887).
DOI 10.1088/1478-7814/9/1/303, cit. on p. 51.

[101] T. Birks and Y. Li: *The shape of fiber tapers*. Journal of Lightwave Technology **10**, 432–438 (1992).
DOI 10.1109/50.134196, cit. on p. 51.

[102] L. Tong, R. R. Gattass, J. B. Ashcom, S. He, J. Lou, M. Shen, I. Maxwell, and E. Mazur: *Subwavelength-diameter silica wires for low-loss optical wave guiding*. Nature **426**, 816–819 (2003).
DOI 10.1038/nature02193, cit. on p. 51.

[103] G. Brambilla, V. Finazzi, and D. J. Richardson: *Ultra-low-loss optical fiber nanotapers*. Optics Express **12**, 2258 (2004).
DOI 10.1364/OPEX.12.002258, cit. on p. 51.

[104] L. Tong, J. Lou, Z. Ye, G. T. Svacha, and E. Mazur: *Self-modulated taper drawing of silica nanowires*. Nanotechnology **16**, 1445–1448 (2005).
DOI 10.1088/0957-4484/16/9/004, cit. on p. 51.

[105] L. Tong, L. Hu, J. Zhang, J. Qiu, Q. Yang, J. Lou, Y. Shen, J. He, and Z. Ye: *Photonic nanowires directly drawn from bulk glasses*. Optics Express **14**, 82 (2006).
DOI 10.1364/OPEX.14.000082, cit. on p. 51.

[106] R. Ismaeel, T. Lee, M. Ding, M. Belal, and G. Brambilla: *Optical microfiber passive components*. Laser and Photonics Reviews **7**, 350–384 (2013).
DOI 10.1002/lpor.201200024, cit. on p. 52.

[107] P. Wang, T. Lee, M. Ding, Z. Lian, X. Feng, Y. Ma, L. Bo, Q. Wu, Y. Semenova, W. Loh, G. Farrell, and G. Brambilla: *White Light trapping using Supercontinuum generation spectra in a lead-silicate Fibre taper*. Journal of Lightwave Technology **32**, 40–45 (2014).
DOI 10.1109/JLT.2013.2289305, cit. on p. 52.

[108] L. Wang, P. Xu, Y. Li, J. Han, X. Guo, Y. Cui, X. Liu, and L. Tong: *Femtosecond Mode-locked Fiber Laser at 1 μm Via Optical Microfiber Dispersion Management*. Scientific Reports **8**, 1–7 (2018).
DOI 10.1038/s41598-018-23027-9, cit. on p. 52.

[109] N. R. Jana, L. Gearheart, and C. J. Murphy: *Seeding growth for size control of 5-40 nm diameter gold nanoparticles*. Langmuir **17**, 6782–6786 (2001).
DOI 10.1021/la0104323, cit. on p. 53.

[110] M. C. Daniel and D. Astruc: *Gold Nanoparticles: Assembly, Supramolecular Chemistry, Quantum-Size-Related Properties, and Applications Toward Biology, Catalysis, and Nanotechnology*. Chemical Reviews **104**, 293–346 (2004).
DOI 10.1021/cr030698+, cit. on pp. 53, 70.

[111] C. J. Ackerson, P. D. Jadzinsky, and R. D. Kornberg: *Thiolate ligands for synthesis of water-soluble gold clusters*. Journal of the American Chemical Society **127**, 6550–6551 (2005).
DOI 10.1021/ja046114i, cit. on p. 53.

[112] S. Roux, B. Garcia, J. L. Bridot, M. Salomé, C. Marquette, L. Lemelle, P. Gillet, L. Blum, P. Perriat, and O. Tillement: *Synthesis, characterization of dihydrolipoic acid capped gold nanoparticles, and functionalization by the electroluminescent luminol*. Langmuir **21**, 2526–2536 (2005).
DOI 10.1021/la048082i, cit. on p. 53.

[113] J. D. Wilton-Ely: *The surface functionalisation of gold nanoparticles with metal complexes*. Journal of the Chemical Society. Dalton Transactions, 25–29 (2007).
DOI 10.1039/b714144k, cit. on p. 53.

[114] M. Grzelczak, J. Pérez-Juste, P. Mulvaney, and L. M. Liz-Marzán: *Shape control in gold nanoparticle synthesis.* Chemical Society Reviews **37**, 1783–1791 (2008). DOI 10.1039/b711490g, cit. on p. 53.

[115] R. Sardar and J. S. Shumaker-Parry: *Spectroscopic and microscopic investigation of gold nanoparticle formation: Ligand and temperature effects on rate and particle size.* Journal of the American Chemical Society **133**, 8179–8190 (2011). DOI 10.1021/ja107934h, cit. on p. 53.

[116] J. Turkevich, P. C. Stevenson, and J. Hillier: *A study of the nucleation and growth processes in the synthesis of colloidal gold.* Discussions of the Faraday Society **11**, 55 (1951). DOI 10.1039/df9511100055, cit. on p. 54.

[117] L. Vigderman and E. R. Zubarev: *High-yield synthesis of gold nanorods with longitudinal SPR peak greater than 1200 nm using hydroquinone as a reducing agent.* Chemistry of Materials **25**, 1450–1457 (2013). DOI 10.1021/cm303661d, cit. on p. 54.

[118] M. J. Schnepf, M. Mayer, C. Kuttner, M. Tebbe, D. Wolf, M. Dulle, T. Altantzis, P. Formanek, S. Förster, S. Bals, T. A. König, and A. Fery: *Nanorattles with tailored electric field enhancement.* Nanoscale **9**, 9376–9385 (2017). DOI 10.1039/c7nr02952g, cit. on p. 54.

[119] M. Liu and P. Guyot-Sionnest: *Mechanism of silver(I)-assisted growth of gold nanorods and bipyramids.* Journal of Physical Chemistry B **109**, 22192–22200 (2005). DOI 10.1021/jp054808n, cit. on p. 55.

[120] L. Liu, T. feng Xu, Z. xiang Dai, S. xun Dai, and T. jun Liu: *A simplified tunable frequency interval optical frequency comb generator using a single continuous-wave laser.* Optoelectronics Letters **13**, 104–107 (2017). DOI 10.1007/s11801-017-6159-x, cit. on p. 55.

[121] H. K. Yip, X. Zhu, X. Zhuo, R. Jiang, Z. Yang, and J. Wang: *Gold Nanobipyramid-Enhanced Hydrogen Sensing with Plasmon Red Shifts Reaching 140 nm at 2 vol% Hydrogen Concentration.* Advanced Optical Materials **5**, 1700740 (2017). DOI 10.1002/adom.201700740, cit. on p. 57.

[122] R. Zsigmondy: *Properties of colloids.* In: Nobel Lecture, Chemistry 1992-1941, Elsevier Publishing Company: Amsterdam (), 1965. ISBN 9781483222486, cit. on p. 62.

[123] C. Sönnichsen, S. Geier, N. E. Hecker, G. Von Plessen, J. Feldmann, H. Ditlbacher, B. Lamprecht, J. R. Krenn, F. R. Aussenegg, V. Z. Chan, J. P. Spatz, and M. Möller: *Spectroscopy of single metallic nanoparticles using total internal reflection microscopy.* Applied Physics Letters **77**, 2949–2951 (2000). DOI 10.1063/1.1323553, cit. on p. 62.

[124] J. J. Mock, M. Barbic, D. R. Smith, D. A. Schultz, and S. Schultz: *Shape effects in plasmon resonance of individual colloidal silver nanoparticles.* Journal of Chemical Physics **116**, 6755–6759 (2002). DOI 10.1063/1.1462610, cit. on p. 62.

[125] C. Sönnichsen, T. Franzl, T. Wilk, G. von Plessen, J. Feldmann, O. Wilson, and P. Mulvaney: *Drastic reduction of plasmon damping in gold nanorods.* Physical Review Letters **88**, 774021–774024 (2002). DOI 10.1103/PhysRevLett.88.077402, cit. on pp. 62, 69.

[126] J. A. Fan, K. Bao, J. B. Lassiter, J. Bao, N. J. Halas, P. Nordlander, and F. Capasso: *Near-Normal Incidence Dark-Field Microscopy: Applications to Nanoplasmonic Spectroscopy.* Nano Letters **12**, 2817–2821 (2012). DOI 10.1021/nl300160y, cit. on p. 63.

[127] K. D. Ko, A. Kumar, K. H. Fung, R. Ambekar, G. L. Liu, N. X. Fang, and K. C. Toussaint: *Nonlinear optical response from arrays of Au bowtie nanoantennas*. Nano Letters **11**, 61–65 (2011).
DOI 10.1021/nl102751m, cit. on p. 68.

[128] B. Metzger, T. Schumacher, M. Hentschel, M. Lippitz, and H. Giessen: *Third Harmonic Mechanism in Complex Plasmonic Fano Structures*. ACS Photonics **1**, 471–476 (2014).
DOI 10.1021/ph5000677, cit. on p. 68.

[129] H. Linnenbank and S. Linden: *Second harmonic generation spectroscopy on second harmonic resonant plasmonic metamaterials*. Optica **2**, 698 (2015).
DOI 10.1364/optica.2.000698, cit. on p. 68.

[130] L. Gui, S. Bagheri, N. Strohfeldt, M. Hentschel, C. M. Zgrabik, B. Metzger, H. Linnenbank, E. L. Hu, and H. Giessen: *Nonlinear Refractory Plasmonics with Titanium Nitride Nanoantennas*. Nano Letters **16**, 5708–5713 (2016).
DOI 10.1021/acs.nanolett.6b02376, cit. on p. 68.

[131] N. Accanto, L. Piatkowski, I. M. Hancu, J. Renger, and N. F. Van Hulst: *Resonant plasmonic nanoparticles for multicolor second harmonic imaging*. Applied Physics Letters **108**, 083115 (2016).
DOI 10.1063/1.4942902, cit. on p. 68.

[132] J. Renger, R. Quidant, N. Van Hulst, S. Palomba, and L. Novotny: *Free-Space excitation of propagating surface plasmon polaritons by nonlinear four-Wave mixing*. Physical Review Letters **103**, 1–4 (2009).
DOI 10.1103/PhysRevLett.103.266802, cit. on p. 68.

[133] V. Kravtsov, R. Ulbricht, J. M. Atkin, and M. B. Raschke: *Plasmonic nanofocused four-wave mixing for femtosecond near-field imaging*. Nature Nanotechnology **11**, 459–464 (2016).
DOI 10.1038/nnano.2015.336, cit. on p. 68.

[134] P. Vasa, W. Wang, R. Pomraenke, M. Lammers, M. Maiuri, C. Manzoni, G. Cerullo, and C. Lienau: *Real-time observation of ultrafast Rabi oscillations between excitons and plasmons in metal nanostructures with J-aggregates.* Nature Photonics **7**, 128–132 (2013).
DOI 10.1038/nphoton.2012.340, cit. on p. 68.

[135] M. Castro-Lopez, D. Brinks, R. Sapienza, and N. F. Van Hulst: *Aluminum for nonlinear plasmonics: Resonance-driven polarized luminescence of Al, Ag, and Au nanoantennas.* Nano Letters **11**, 4674–4678 (2011).
DOI 10.1021/nl202255g, cit. on p. 68.

[136] P. Biagioni, D. Brida, J. S. Huang, J. Kern, L. Duò, B. Hecht, M. Finazzi, and G. Cerullo: *Dynamics of four-photon photoluminescence in gold nanoantennas.* Nano Letters **12**, 2941–2947 (2012).
DOI 10.1021/nl300616s, cit. on pp. 68, 70, 93.

[137] S. Wang, W. Xi, F. Cai, X. Zhao, Z. Xu, J. Qian, and S. He: *Three-photon luminescence of gold nanorods and its applications for high contrast tissue and deep in vivo brain imaging.* Theranostics **5**, 251–266 (2015).
DOI 10.7150/thno.10396, cit. on pp. 68, 69, 91, 93.

[138] V. Knittel, M. P. Fischer, T. De Roo, S. Mecking, A. Leitenstorfer, and D. Brida: *Nonlinear photoluminescence spectrum of single gold nanostructures.* ACS Nano **9**, 894–900 (2015).
DOI 10.1021/nn5066233, cit. on pp. 68, 81, 95, 101.

[139] V. Knittel, M. P. Fischer, M. Vennekel, T. Rybka, A. Leitenstorfer, and D. Brida: *Dispersion of the nonlinear susceptibility in gold nanoantennas.* Physical Review B **96**, 1–6 (2017).
DOI 10.1103/PhysRevB.96.125428, cit. on pp. 68, 91.

[140] J. Lee, M. Tymchenko, C. Argyropoulos, P.-Y. Chen, F. Lu, F. Demmerle, G. Boehm, M.-C. Amann, A. Alù, and M. A. Belkin: *Giant nonlinear response from plasmonic metasurfaces coupled to intersubband transitions.* Nature **511**, 65–69 (2014).
DOI 10.1038/nature13455, cit. on p. 68.

[141] G. Grinblat, M. Rahmani, E. Cortés, M. Caldarola, D. Comedi, S. A. Maier, and A. V. Bragas: *High-efficiency second harmonic generation from a single hybrid ZnO nanowire/Au plasmonic nano-oligomer.* Nano Letters **14**, 6660–6665 (2014).
DOI 10.1021/nl503332f, cit. on pp. 68, 69, 110.

[142] C. Kai, C. Durak, J. R. Heflin, and H. D. Robinson: *Plasmon-enhanced second-harmonic generation from ionic self-assembled multilayer films.* Nano Letters **7**, 254–258 (2007).
DOI 10.1021/nl062090x, cit. on p. 68.

[143] G. Albrecht, M. Hentschel, S. Kaiser, and H. Giessen: *Hybrid Organic-Plasmonic Nanoantennas with Enhanced Third-Harmonic Generation.* ACS Omega **2**, 2577–2582 (2017).
DOI 10.1021/acsomega.7b00481, cit. on p. 68.

[144] Y. Pu, R. Grange, C. L. Hsieh, and D. Psaltis: *Nonlinear optical properties of core-shell nanocavities for enhanced second-harmonic generation.* Physical Review Letters **104**, 1–4 (2010).
DOI 10.1103/PhysRevLett.104.207402, cit. on pp. 68, 110.

[145] X. Ye, Y. Gao, J. Chen, D. C. Reifsnyder, C. Zheng, and C. B. Murray: *Seeded growth of monodisperse gold nanorods using bromide-free surfactant mixtures.* Nano Letters **13**, 2163–2171 (2013).
DOI 10.1021/nl400653s, cit. on p. 69.

[146] M. Mayer, L. Scarabelli, K. March, T. Altantzis, M. Tebbe, M. Kociak, S. Bals, F. J. Garciá De Abajo, A. Fery, and L. M. Liz-Marzán: *Controlled Living Nanowire Growth: Precise Control over the Morphology and Optical Properties of AgAuAg Bimetallic Nanowires.* Nano Letters **15**, 5427–5437 (2015).
DOI 10.1021/acs.nanolett.5b01833, cit. on p. 69.

[147] J. S. Huang, V. Callegari, P. Geisler, C. Brüning, J. Kern, J. C. Prangsma, X. Wu, T. Feichtner, J. Ziegler, P. Weinmann, M. Kamp, A. Forchel, P. Biagioni, U. Sennhauser, and B. Hecht: *Atomically flat single-crystalline gold nanostructures for plasmonic nanocircuitry.* Nature Communications **1**, 150–158 (2010).
DOI 10.1038/ncomms1143, cit. on p. 69.

[148] G. Bachelier, I. Russier-Antoine, E. Benichou, C. Jonin, N. Del Fatti, F. Vallée, and P. F. Brevet: *Fano profiles induced by near-field coupling in heterogeneous dimers of gold and silver nanoparticles.* Physical Review Letters **101**, 5–8 (2008).
DOI 10.1103/PhysRevLett.101.197401, cit. on p. 69.

[149] H. Aouani, M. Rahmani, M. Navarro-Cía, and S. A. Maier: *Third-harmonic-upconversion enhancement from a single semiconductor nanoparticle coupled to a plasmonic antenna.* Nature Nanotechnology **9**, 290–294 (2014).
DOI 10.1038/nnano.2014.27, cit. on p. 69.

[150] J. Alegret, T. Rindzevicius, T. Pakizeh, Y. Alaverdyan, L. Gunnarsson, and M. Käll: *Plasmonic properties of silver trimers with trigonal symmetry fabricated by electron-beam lithography.* Journal of Physical Chemistry C **112**, 14313–14317 (2008).
DOI 10.1021/jp804505k, cit. on p. 69.

[151] M. Rahmani, D. Y. Lei, V. Giannini, B. Lukiyanchuk, M. Ranjbar, T. Y. F. Liew, M. Hong, and S. A. Maier: *Subgroup decomposition of plasmonic resonances in hybrid oligomers: Modeling the resonance lineshape.* Nano Letters **12**, 2101–2106 (2012).
DOI 10.1021/nl3003683, cit. on p. 69.

[152] N. Liu, L. Langguth, T. Weiss, J. Kästel, M. Fleischhauer, T. Pfau, and H. Giessen: *Plasmonic analogue of electromagnetically induced transparency at the Drude damping limit.* Nature Materials **8**, 758–762 (2009).
DOI 10.1038/nmat2495, cit. on p. 69.

[153] R. Taubert, M. Hentschel, J. Kästel, and H. Giessen: *Classical Analog of Electromagnetically Induced Absorption in Plasmonics.* Nano Letters **12**, 1367–1371 (2012).
DOI 10.1021/nl2039748, cit. on pp. 69, 110.

[154] R. Taubert, M. Hentschel, and H. Giessen: *Plasmonic analog of electromagnetically induced absorption: simulations, experiments, and coupled oscillator analysis.* Journal of the Optical Society of America B **30**, 3123 (2013).
DOI 10.1364/josab.30.003123, cit. on p. 69.

[155] D. Floess, M. Hentschel, T. Weiss, H. U. Habermeier, J. Jiao, S. G. Tikhodeev, and H. Giessen: *Plasmonic analog of electromagnetically induced absorption leads to giant thin film Faraday rotation of 14°.* Physical Review X **7**, 1–10 (2017).
DOI 10.1103/PhysRevX.7.021048, cit. on pp. 69, 110.

[156] K. Imura and H. Okamoto: *Properties of photoluminescence from single gold nanorods induced by near-field two-photon excitation.* Journal of Physical Chemistry C **113**, 11756–11759 (2009).
DOI 10.1021/jp9018074, cit. on p. 69.

[157] P. Biagioni, M. Celebrano, M. Savoini, G. Grancini, D. Brida, S. Mátéfi-Tempfli, M. Mátéfi-Tempfli, L. Duò, B. Hecht, G. Cerullo, and M. Finazzi: *Dependence of the two-photon photoluminescence yield of gold nanostructures on the laser pulse duration.* Physical Review B - Condensed Matter and Materials Physics **80**, 1–5 (2009).
DOI 10.1103/PhysRevB.80.045411, cit. on pp. 69, 100.

[158] M. B. Lien, J. Y. Kim, M. G. Han, Y. C. Chang, Y. C. Chang, H. J. Ferguson, Y. Zhu, A. A. Herzing, J. C. Schotland, N. A. Kotov, and T. B. Norris: *Optical Asymmetry and Nonlinear Light Scattering from Colloidal Gold Nanorods.* ACS Nano **11**, 5925–5932 (2017).
DOI 10.1021/acsnano.7b01665, cit. on p. 69.

[159] A. M. Gobin, M. H. Lee, N. J. Halas, W. D. James, R. A. Drezek, and J. L. West: *Near-infrared resonant nanoshells for combined optical imaging and photothermal cancer therapy.* Nano Letters **7**, 1929–1934 (2007).
DOI 10.1021/nl070610y, cit. on p. 69.

[160] G. T. Boyd, Z. H. Yu, and Y. R. Shen: *Photoinduced luminescence from the noble metals and its enhancement on roughened surfaces.* Physical Review B **33**, 7923–7936 (1986).
DOI 10.1103/PhysRevB.33.7923, cit. on p. 69.

[161] N. J. Durr, T. Larson, D. K. Smith, B. A. Korgel, K. Sokolov, and A. Ben-Yakar: *Two-Photon Luminescence Imaging of Cancer Cells Using Molecularly Targeted Gold Nanorods.* Nano Letters **7**, 941–945 (2007).
DOI 10.1021/nl062962v, cit. on pp. 69, 70.

[162] J. Olesiak-Banska, M. Waszkielewicz, P. Obstarczyk, and M. Samoc: *Two-photon absorption and photoluminescence of colloidal gold nanoparticles and nanoclusters.* Chemical Society Reviews **48**, 4087–4117 (2019).
DOI 10.1039/c8cs00849c, cit. on p. 69.

[163] P. Ghenuche, S. Cherukulappurath, T. H. Taminiau, N. F. Van Hulst, and R. Quidant: *Spectroscopic mode mapping of resonant plasmon nanoantennas.* Physical Review Letters **101**, 1–4 (2008).
DOI 10.1103/PhysRevLett.101.116805, cit. on p. 70.

[164] J. S. Huang, J. Kern, P. Geisler, P. Weinmann, M. Kamp, A. Forchel, P. Biagioni, and B. Hecht: *Mode imaging and selection in strongly coupled nanoantennas.* Nano Letters **10**, 2105–2110 (2010).
DOI 10.1021/nl100614p, cit. on p. 70.

[165] M. Beversluis, A. Bouhelier, and L. Novotny: *Continuum generation from single gold nanostructures through near-field mediated intraband transitions.* Physical Review B - Condensed Matter and Materials Physics **68**, 1–10 (2003).
DOI 10.1103/PhysRevB.68.115433, cit. on p. 70.

[166] P. N. Melentiev, A. E. Afanasiev, A. A. Kuzin, A. V. Zablotskiy, and V. I. Balykin: *Giant enhancement of two photon induced luminescence in metal nanostructure.* Optics Express **23**, 11444 (2015).
DOI 10.1364/oe.23.011444, cit. on p. 70.

[167] F. Wackenhut, X. Wang, A. V. Failla, and A. J. Meixner: *Two and three photon excited luminescence of single gold nanoparticles: Switching between plasmon- and electron-hole-pair emission by ultrashort laser pulses.* arXiv (2018).
PMID 1812.01409, cit. on pp. 70, 101.

[168] R. A. Farrer, F. L. Butterfiefd, V. W. Chen, and J. T. Fourkas: *Highly efficient multiphoton-absorption-lnduced luminescence from gold nanoparticles.* Nano Letters **5**, 1139–1142 (2005).
DOI 10.1021/nl050687r, cit. on p. 70.

[169] P. Muhlschlegel: *Resonant Optical Antennas.* Science **308**, 1607–1609 (2005).
DOI 10.1126/science.1111886, cit. on pp. 70, 93.

[170] E. Sakat, I. Bargigia, M. Celebrano, A. Cattoni, S. Collin, D. Brida, M. Finazzi, C. D'Andrea, and P. Biagioni: *Time-Resolved Photoluminescence in Gold Nanoantennas.* ACS Photonics **3**, 1489–1493 (2016).
DOI 10.1021/acsphotonics.6b00039, cit. on p. 70.

[171] H. D. Deng, G. C. Li, Q. F. Dai, M. Ouyang, S. Lan, V. A. Trofimov, and T. M. Lysak: *Size dependent competition between second harmonic generation and two-photon luminescence observed in gold nanoparticles.* Nanotechnology **24**, 075201 (2013).
DOI 10.1088/0957-4484/24/7/075201, cit. on p. 70.

[172] N. Gao, Y. Chen, L. Li, Z. Guan, T. Zhao, N. Zhou, P. Yuan, S. Q. Yao, and Q. H. Xu: *Shape-dependent two-photon photoluminescence of single gold nanoparticles.* Journal of Physical Chemistry C **118**, 13904–13911 (2014).
DOI 10.1021/jp502038v, cit. on p. 70.

[173] A. M. Siddiquee, A. B. Taylor, S. Syed, G. H. Lim, B. Lim, and J. W. Chon: *Measurement of Plasmon-Mediated Two-Photon Luminescence Action Cross Sections of Single Gold Bipyramids, Dumbbells, and Hemispherically Capped Cylindrical Nanorods.* Journal of Physical Chemistry C **119**, 28536–28543 (2015).
DOI 10.1021/acs.jpcc.5b08214, cit. on p. 70.

[174] M. Sivis, N. Pazos-Perez, R. Yu, R. Alvarez-Puebla, F. J. García de Abajo, and C. Ropers: *Continuous-wave multiphoton photoemission from plasmonic nanostars.* Communications Physics **1**, 13 (2018).
DOI 10.1038/s42005-018-0014-7, cit. on p. 70.

[175] E. Hutter and J. H. Fendler: *Exploitation of localized surface plasmon resonance.* Advanced Materials **16**, 1685–1706 (2004).
DOI 10.1002/adma.200400271, cit. on p. 70.

[176] A. L. González, J. A. Reyes-Esqueda, and C. Noguez: *Optical properties of elongated noble metal nanoparticles*. Journal of Physical Chemistry C **112**, 7356–7362 (2008).
DOI 10.1021/jp800432q, cit. on p. 70.

[177] J. Z. Zhang and C. Noguez: *Plasmonic optical properties and applications of metal nanostructures*. Plasmonics **3**, 127–150 (2008).
DOI 10.1007/s11468-008-9066-y, cit. on p. 70.

[178] M. Hu, C. Novo, A. Funston, H. Wang, H. Staleva, S. Zou, P. Mulvaney, Y. Xia, and G. V. Hartland: *Dark-field microscopy studies of single metal nanoparticles: Understanding the factors that influence the linewidth of the localized surface plasmon resonance*. Journal of Materials Chemistry **18**, 1949–1960 (2008).
DOI 10.1039/b714759g, cit. on p. 70.

[179] V. Amendola, R. Pilot, M. Frasconi, O. M. Maragò, and M. A. Iatì: *Surface plasmon resonance in gold nanoparticles: A review*. Journal of Physics Condensed Matter **29** (2017).
DOI 10.1088/1361-648X/aa60f3, cit. on p. 70.

[180] M. Lippitz, M. A. Van Dijk, and M. Orrit: *Third-harmonic generation from single gold nanoparticles*. Nano Letters **5**, 799–802 (2005).
DOI 10.1021/nl0502571, cit. on p. 93.

[181] D.-S. Wang, F.-Y. Hsu, and C.-W. Lin: *Surface plasmon effects on two photon luminescence of gold nanorods*. Optics Express **17**, 11350 (2009).
DOI 10.1364/oe.17.011350, cit. on p. 93.

[182] T. Haug, P. Klemm, S. Bange, and J. M. Lupton: *Hot-Electron Intraband Luminescence from Single Hot Spots in Noble-Metal Nanoparticle Films*. Physical Review Letters **115**, 1–5 (2015).
DOI 10.1103/PhysRevLett.115.067403, cit. on p. 100.

[183] Y. He, K. Xia, G. Lu, H. Shen, Y. Cheng, Y. C. Liu, K. Shi, Y. F. Xiao, and Q. Gong: *Surface enhanced anti-Stokes one-photon luminescence from single gold nanorods.* Nanoscale **7**, 577–582 (2015).
DOI 10.1039/c4nr04879b, cit. on p. 100.

[184] J. T. Hugall and J. J. Baumberg: *Demonstrating Photoluminescence from Au is Electronic Inelastic Light Scattering of a Plasmonic Metal: The Origin of SERS Backgrounds.* Nano Letters **15**, 2600–2604 (2015).
DOI 10.1021/acs.nanolett.5b00146, cit. on p. 100.

[185] K. Imura, T. Nagahara, and H. Okamoto: *Near-field two-photon-induced photoluminescence from single gold nanorods and imaging of plasmon modes.* Journal of Physical Chemistry B **109**, 13214–13220 (2005).
DOI 10.1021/jp051631o, cit. on pp. 100, 102.

[186] R. Rosei: *Temperature modulation of the optical transitions involving the fermi surface in Ag: Theory.* Physical Review B **10**, 474–483 (1974).
DOI 10.1103/PhysRevB.10.474, cit. on p. 100.

[187] M. Guerrisi, R. Rosei, and P. Winsemius: *Splitting of the interband absorption edge in Au.* Physical Review B **12**, 557–563 (1975).
DOI 10.1103/PhysRevB.12.557, cit. on p. 100.

[188] Z. Guan, N. Gao, X. F. Jiang, P. Yuan, F. Han, and Q. H. Xu: *Huge enhancement in two-photon photoluminescence of au nanoparticle clusters revealed by single-particle spectroscopy.* Journal of the American Chemical Society **135**, 7272–7277 (2013).
DOI 10.1021/ja400364f, cit. on p. 101.

[189] V. Remesh, M. Stührenberg, L. Saemisch, N. Accanto, and N. F. Van Hulst: *Phase control of plasmon enhanced two-photon photoluminescence in resonant gold nanoantennas.* Applied Physics Letters **113**, 211101 (2018).
DOI 10.1063/1.5051381, cit. on p. 101.

[190] L. P. Bouckaert, R. Smoluchowski, and E. Wigner: *Theory of Brillouin Zones and Symmetry Properties of Wave Functions in Crystals*. Physical Review **50**, 58–67 (1936).
DOI 10.1103/PhysRev.50.58, cit. on p. 102.

[191] D. Lehr, J. Reinhold, I. Thiele, H. Hartung, K. Dietrich, C. Menzel, T. Pertsch, E. B. Kley, and A. Tünnermann: *Enhancing second harmonic generation in gold nanoring resonators filled with lithium niobate*. Nano Letters **15**, 1025–1030 (2015).
DOI 10.1021/nl5038819, cit. on p. 110.

[192] S. Liu, M. B. Sinclair, S. Saravi, G. A. Keeler, Y. Yang, J. Reno, G. M. Peake, F. Setzpfandt, I. Staude, T. Pertsch, and I. Brener: *Resonantly Enhanced Second-Harmonic Generation Using III-V Semiconductor All-Dielectric Metasurfaces*. Nano Letters **16**, 5426–5432 (2016).
DOI 10.1021/acs.nanolett.6b01816, cit. on p. 110.

[193] P. P. Vabishchevich, S. Liu, M. B. Sinclair, G. A. Keeler, G. M. Peake, and I. Brener: *Enhanced Second-Harmonic Generation Using Broken Symmetry III-V Semiconductor Fano Metasurfaces*. ACS Photonics **5**, 1685–1690 (2018).
DOI 10.1021/acsphotonics.7b01478, cit. on p. 110.

[194] K. Thyagarajan, J. Butet, and O. J. Martin: *Augmenting second harmonic generation using fano resonances in plasmonic systems*. Nano Letters **13**, 1847–1851 (2013).
DOI 10.1021/nl400636z, cit. on p. 110.

[195] H. Aouani, M. Navarro-Cia, M. Rahmani, T. P. Sidiropoulos, M. Hong, R. F. Oulton, and S. A. Maier: *Multiresonant broadband optical antennas as efficient tunable nanosources of second harmonic light*. Nano Letters **12**, 4997–5002 (2012).
DOI 10.1021/nl302665m, cit. on p. 110.

[196] S. D. Liu, E. S. P. Leong, G. C. Li, Y. Hou, J. Deng, J. H. Teng, H. C. Ong, and D. Y. Lei: *Polarization-independent multiple fano resonances in plasmonic nonamers for multimode-matching enhanced multiband second-harmonic generation.* ACS Nano **10**, 1442–1453 (2016). DOI 10.1021/acsnano.5b06956, cit. on p. 110.

[197] K. Y. Yang, J. Butet, C. Yan, G. D. Bernasconi, and O. J. Martin: *Enhancement Mechanisms of the Second Harmonic Generation from Double Resonant Aluminum Nanostructures.* ACS Photonics **4**, 1522–1530 (2017). DOI 10.1021/acsphotonics.7b00288, cit. on p. 110.

[198] S. Zou, N. Janel, and G. C. Schatz: *Silver nanoparticle array structures that produce remarkably narrow plasmon lineshapes.* Journal of Chemical Physics **120**, 10871–10875 (2004). DOI 10.1063/1.1760740, cit. on p. 110.

[199] B. Auguié and W. L. Barnes: *Collective resonances in gold nanoparticle arrays.* Physical Review Letters **101**, 1–4 (2008). DOI 10.1103/PhysRevLett.101.143902, cit. on p. 110.

[200] M. Hentschel, T. Utikal, H. Giessen, and M. Lippitz: *Quantitative modeling of the third harmonic emission spectrum of plasmonic nanoantennas.* Nano Letters **12**, 3778–3782 (2012). DOI 10.1021/nl301686x, cit. on pp. 110, 115.

[201] M. J. Huttunen, O. Reshef, T. Stolt, K. Dolgaleva, R. W. Boyd, and M. Kauranen: *Efficient nonlinear metasurfaces by using multiresonant high-Q plasmonic arrays.* Journal of the Optical Society of America B **36**, E30 (2019). DOI 10.1364/JOSAB.36.000E30, cit. on pp. 110, 129.

[202] J. A. Van Nieuwstadt, M. Sandtke, R. H. Harmsen, F. B. Segerink, J. C. Prangsma, S. Enoch, and L. Kuipers: *Strong modification of the nonlinear optical response of metallic subwavelength hole arrays.* Physical Review Letters **97**, 1–4 (2006). DOI 10.1103/PhysRevLett.97.146102, cit. on p. 115.

[203] A. Benedetti, M. Centini, M. Bertolotti, and C. Sibilia: *Second harmonic generation from 3D nanoantennas: on the surface and bulk contributions by far-field pattern analysis.* Optics Express **19**, 26752 (2011).
DOI 10.1364/oe.19.026752, cit. on p. 115.

[204] T. Hanke, J. Cesar, V. Knittel, A. Trügler, U. Hohenester, A. Leitenstorfer, and R. Bratschitsch: *Tailoring spatiotemporal light confinement in single plasmonic nanoantennas.* Nano Letters **12**, 992–996 (2012).
DOI 10.1021/nl2041047, cit. on p. 115.

[205] F. Wang and H. Harutyunyan: *Tailoring the quality factors and nonlinear response in hybrid plasmonic-dielectric metasurfaces.* Optics Express **26**, 120 (2018).
DOI 10.1364/oe.26.000120, cit. on p. 115.

[206] B. Metzger, M. Hentschel, M. Lippitz, and H. Giessen: *Third-harmonic spectroscopy and modeling of the nonlinear response of plasmonic nanoantennas.* Optics Letters **37**, 4741 (2012).
DOI 10.1364/ol.37.004741, cit. on p. 115.

[207] R. Czaplicki, A. Kiviniemi, M. J. Huttunen, X. Zang, T. Stolt, I. Vartiainen, J. Butet, M. Kuittinen, O. J. F. Martin, and M. Kauranen: *Less Is More: Enhancement of Second-Harmonic Generation from Metasurfaces by Reduced Nanoparticle Density.* Nano Letters **18**, 7709–7714 (2018).
DOI 10.1021/acs.nanolett.8b03378, cit. on p. 126.

[208] M.-L. Ren, W. Liu, C. O. Aspetti, L. Sun, and R. Agarwal: *Enhanced second-harmonic generation from metal-integrated semiconductor nanowires via highly confined whispering gallery modes.* Nature Communications **5**, 5432 (2014).
DOI 10.1038/ncomms6432, cit. on p. 127.

[209] L. Gui, S. Bagheri, N. Strohfeldt, M. Hentschel, C. M. Zgrabik, B. Metzger, H. Linnenbank, E. L. Hu, and H. Giessen: *Nonlinear Refractory Plasmonics with Titanium Nitride Nanoantennas.* Nano Letters **16**, 5708–5713 (2016).
DOI 10.1021/acs.nanolett.6b02376, cit. on p. 129.

[210] C. G. Biris and N. C. Panoiu: *Nonlinear pulsed excitation of high-Q optical modes of plasmonic nanocavities.* Optics Express **18**, 17165 (2010).
DOI 10.1364/oe.18.017165, cit. on p. 135.

[211] T. Harayama, P. Davis, and K. S. Ikeda: *Nonlinear whispering gallery modes.* Physical Review Letters **82**, 3803–3806 (1999).
DOI 10.1103/PhysRevLett.82.3803, cit. on p. 135.

PUBLICATIONS

Parts of this thesis and associated work have been published in scientific journals, have been submitted to a journal, are being prepared for publication, have been presented and/or to be presented at national and international conferences.

JOURNAL PUBLICATIONS

P1 Q. Ai, L. Gui, D. Paone, B. Metzger, M. Mayer, K. Weber, A.Fery, H. Giessen,
"**Ultranarrow Second-Harmonic Resonances in Hybrid Plasmon-Fiber Cavities**",
Nano Letters **18**(9), 5576-5582 (2018),
DOI 10.1021/acs.nanolett.8b02005.

P2 Q. Ai, H. Zhang, J. Wang, and H. Giessen,
"**Multiphoton Photoluminescence in Hybrid Plasmon-Fiber Cavities with Au and Au@Pd Nanobipyramids: Two-Photon versus Four-Photon processes and rapid quenching**",
ACS Photonics **8**(7), 2088–2094 (2021),
DOI 10.1021/acsphotonics.1c00470.

P3 Q. Ai, F. Sterl, H. Zhang, J. Wang, and H. Giessen,
"**Giant Second Harmonic Generation Enhancement in a High-Q Doubly Resonant Hybrid Plasmon-Fiber Cavity System**",
ACS Nano (2021),
DOI 10.1021/acsnano.1c05970.

JOURNAL PUBLICATIONS BEYOND THE SCOPE OF THIS THESIS

O1 Q. Ai, X. Chen, M. Tian, B. Yan, Y. Zhang, F. Song, G. Chen, X, Sang, Y, Wang, F, Xiao, and K. Alameh,

"**Demonstration of Multi-Wavelength Tunable Fiber Lasers Based on a Digital Micormirror Device Processor**",
Applied Optics **54**(4), 603-607 (2015),
DOI 10.1364/AO.54.000603.

O2 Q. Ai, X. Chen, M. Tian, B. Yan, F. Song, G. Chen, X, Sang, and Y, Wang,
"**Multi-Channel C-Band-Tunable Fiber Lasers Based on DMD Processor**",
Acta Optica Sinica **34**(4), 0414001 (2014),
DOI 10.3788/AOS201434.0414001

O3 T, Wang, X, Sang, B. Yan, Q. Ai, Y, Li, X. Chen, Y. Zhang, G. Chen, F. Song, X, Zhang, K, Wang, J, Yuan, C, Yu, F, Xiao, and K. Alameh,
"**Tunable Mircowave signal generation based on an Opto-DMD processor and a photonic crystal fiber**",
Chinese Physics B **23**(6), 064217 (2014),
DOI 10.1088/1674-1056/23/6/064217

O4 K, Huang, B. Yan, X. Chen, X, G. Chen, Q. Ai, K, Wang, Y, Wang, Y. Zhang, F. Song, Q, Wu and X. Sang,
"**High Stable Single-Polarization Tunable Fiber Laser Based on Opto-DMD Processor and Polarization-Maintaining Fiber Devices**",
Laser Physics **22**, 1833-1836 (2012),
DOI 10.1134/S1054660X12120146.

CONFERENCE CONTRIBUTIONS AS PRESENTING AUTHOR

C1 Q. Ai, D. Paone, K. Kaefer, S. Celiksoy, C. Soennichsen, and H. Giessen,
"**Strong Coupling of Localized Surface Plamsons and Whispering Gallery Modes**",
Spring Meeting of the German Physical Society (DPG), Regensburg, Germany (2016), poster presentation.

C2 Q. Ai, D. Paone, K. Kaefer, S. Celiksoy, C. Soennichsen, and H. Giessen,
"**Efficient Coupling of Localized Surface Plamsons and Whispering Gallery Modes**",
Optical Nanospectrosocpy III and Topical Meeting on Nonlinear Plasmonics, Rome, Italy (2016), poster presentation.

C3 Q. Ai and H. Giessen,
"**Efficient Coupling of Localized Surface Plamsons and Whispering Gallery Modes**",
Sino-German Symposium, Herrenberg, Germany (2016), poster presentation.

C4 Q. Ai, D. Paone, K. Kaefer, S. Celiksoy, C. Soennichsen, and H. Giessen,
"**Efficient Coupling of Localized Surface Plamsons and Whispering Gallery Modes**",
Gordon Research Seminar and Conference on Plasmonics and Nanophotonics (GRS/GRC), Newry, ME, USA (2016), poster presentation.

C5 Q. Ai, D. Paone, M. Mayer, A. Fery, and H. Giessen,
"**Second-Harmonic Generation from Coupling of Localized Surface Plasmons and Whispering Gallery Cavity**",
Kompetenznetz Funktionelle Nanostrukturen (NanoNetz), Bad Herrenalb, Germany (2016), oral and poster presentation.

C6 Q. Ai, D. Paone, M. Mayer, A. Fery, and H. Giessen,
"**Second-Harmonic Generation from Coupling of Localized Surface Plasmons and Whispering Gallery Cavity**",
Strong Coupling with Organic Molecules (SCOM16), Donostia - San Sebastian, Spain (2016), poster presentation.

C7 Q. Ai, D. Paone, M. Mayer, and H. Giessen,
"**Ultranarrow nonlinear resonances in hybrid fiber-plasmon cavities**",
Spring Meeting of the German Physical Society (DPG), Dresden, Germany (2017), oral presentation.

C8 Q. Ai, L. Gui, D. Paone, B. Metzger, M. Mayer, K. Weber, A.Fery, H. Giessen,
"**Ultranarrow Second-Harmonic Resonances in Hybrid Plasmon-Fiber Cavities**",
Spring Meeting of the German Physical Society (DPG), Erlangen, Germany (2018), oral presentation.

C9 Q. Ai, F. Sterl, H. Zhang, J. Wang, and H. Giessen,
"**Giant Second Harmonic Generation in Hybrid Plasmon-Fiber Cavity Systems**",
Conference on Lasers and Electro-Optics (CLEO), California, USA(2021), oral presentation.

ACKNOWLEDGMENTS

Six years of doing my PhD at the 4^{th} Physics Institute at the University of Stuttgart made a different and better me. Six years ago, I was anxious and worried about the upcoming PhD study abroad. Now as it soon comes to an end, I have to say that I have not only survived but also enjoyed this amazing journey. Obviously, this change and this thesis would not exist without the people who helped and accompanied me throughout the whole journey.

First and foremost, I want to thank Prof. Harald Giessen for giving me such an opportunity to study in his group. That is the beginning of a beautiful and fantastic PhD journey. In the last six years, he was always encouraging me, supporting me with the projects and especially patiently explaining all the shortages in my experiment and analysis. I also learnt a lot from him, including intellectual insights, high efficient working and critical thinking. When I read his notes in 1998 to tune our Ti:sapphire laser, I was entierely shocked by the details and the intact saving. I believe that those stimulations will accompany me in my future research and entire life.

I would like to thank Prof. Dr. Hans Peter Büchler and Prof. Dr. Peter Michler for agreeing to be my examiners, for taking the time and effort to examine my thesis and also for arranging the PhD examination.

I would also like to express my thanks to Dr. Christine von Rekowski. I would have even missed my contract more than once without her. She is such a considerable and productive person and always taking care of all the administrative matters so well. My visa could only be extended smoothly when she helped me with the documents.

Special thanks to Dr. Lili Gui, who help me to transfer the research field from fiber lasers to nonlinear plasmonics successfully. It is my honor to work with her day by day in the first year of my PhD. She is one of the most hard-working researchers I met. Her solid knowledge background gave me a deep impression when she told me I could find the particular theory on the specific page of one book. Thanks for her useful discussions and helpful guidance in the years she was here and also the entire six years.

My heart-felt thanks go to our senior group member, Dr. Nik Strohfeldt and Dr. Florian Sterl, who built the microspectroscopy setup and supplied their valuable technical support for all my projects. Especially, Dr. Florain Sterl helped me to improve my illumination components and doing the power calibration of the spectrometer. He is the best listener and problem solver of all the troubles I met with the experimental setup.

Certainly, my project cannot be running successful without Prof. Jianfang Wang, Dr. Han Zhang, Dr. Martin Mayer, Dr. Sirin Celiksory, Domemnico Paone, who provided me with the awesome chemical nanoparticles used in my hybrid system. Thanks to their effort and time in modifying the parameters of samples to satisfy the demand I supposed. Thanks so much for their patience. The same thanks goes to Dr. Bernd Metzger, who shared the theoretical model of the coupled anharmonic oscillator with me. All those people have contributed directly to the work present in this thesis. Also thanks Dr. Mario Hentschel for sharing deep insights of nonlinear plasmonics with me and doing EDX mapping of the samples.

I also want to give a big special thanks to my colleague, my officemate and also my best friend in Germany, Ksenia Weber. She helped me with the scanning electron microscopy, polishing posters, papers, testing all my presentations, and even adapting to the new circumstance in Germany. She is far more important to me than just the academic workings. I really appreciate that we turn out to be such good friends even though I spoke poor English and even did not introduce myself when we first meet. It sounds like a joke, but, it is such an embarrassing situation that makes us feel how strong and genuine friendship is built in the past. She is another big harvest for me in the last six years except the PhD degree.

Also thanks to our 'lunch group': Dr. Andy Steinman, Dr. Asa Asadollahbaik, Dr. Rostyslav Semenyshyn, Dr. Izzatjon Allayarov, Dr. Josselin Defrance, Dr. Swaathi Upendar, Steffen Both, Sascha Böhrkircher, Zhen Wang and also Dr. Florian Sterl, Ksenia Weber, and all the rest. Thanks for making the time during the lunch and following coffee break more interesting and enjoyable. Especially, I am grateful to Ksenia Weber, Steffan Both, Sascha Böhrkircher, Dr. Florian Sterl for taking care and playing games with Timo, thus I can have more time working on my PhD. My thanks would go to all the members of the PI4 for contributing to such a nice working atmosphere.

Last but definitely not least, I would like to extend my deep gratefulness to my beloved family, who are always supporting me unconditionally,

especially, my mother and mother-in-law took turns every three month traveling to Germany to take care of my son Timo in his first two years. Without them, I cannot imagine how difficult it would be. And of course, to my husband Ning Zhou, for encouraging me to be myself and to come to Germany, for continually supporting me through the tough six years, for sharing all the happiness and misery in the past ten years and coming days, and for everything you have done. To my Son, Timo Zhou, for coming to be an important member of our family, for giving me power to face all the difficulties, and for inspiring me to see the world and life from a new perspective.

DECLARATION

I hereby certify that this dissertation is entirely my own work except where otherwise indicated. Passages and ideas from other sources have been clearly marked as such.

Stuttgart, 2021

Qi Ai

COLOPHON

This thesis was typeset with LaTeX 2_ε using Robert Slimbach's Minion Pro font. The style was inspired by Robert Bringhurst's "*The Elements of Typographic Style*". It is available for LaTeX via CTAN as CLASSICTHESIS.